The Pennsylvania State University

The Graduate School

Materials Science and Engineering

PULSED LASER DEPOSITION OF BISMUTH ZINC NIOBATE THIN FILMS FOR DIELECTRIC APPLICATIONS

A Thesis in

Materials Science and Engineering

by

Lisa Friedman Edge

Submitted in Partial Fulfillment
of the Requirements
for the Degree of

Master of Science

August 2002

Lisa Friedman Edge

We approve the thesis of Lisa Friedman Edge.

Date of Signature

Susan Trolier-McKinstry
Professor of Ceramic Science and Engineering
Thesis Advisor

Michael T. Lanagan
Associate Professor of Materials Science and Engineering

Russell F. Messier
Professor of Engineering Science and Mechanics

James P. Runt
Professor of Polymer Science
Associate Head for Graduate Studies
Department of Materials Science and Engineering

Abstract

There is considerable interest in being able to deposit high permittivity dielectrics on integrated circuits after the metallization steps, as on-chip decoupling capacitors. This requires that the dielectric have a high capacitance density at modest crystallization temperatures. Among the candidates materials are the bismuth-zinc-niobate, BZN, pyrochlores. These materials show permittivities of 80 to 180, with no thickness dependence of the permittivity.

As a test vapor deposition method, $Bi_{1.5}Zn_{1.0}Nb_{1.5}O_7$ and $Bi_{1.5}Zn_{0.5}Nb_{1.5}O_{6.5}$ thin films were grown by pulsed laser deposition, PLD, on Pt/Ti/SiO_2/Si and Pt/ La, Pt alloy (5 vol % La in Pt)/ La_2O_3/SiO_2/Si wafers. The relationships between processing and properties were studied. The film composition was studied by Rutherford backscattering as a function of target composition, target to substrate distance, laser frequency, substrate temperature, target exposure, and chamber pressure. It was found that the compositional control in BZN was extremely complicated in the PLD process, due to the complex interplay between deposition variables and the large apparent solubility limits in the pyrochlore structure. The target to substrate distance and the chamber pressure were the dominant parameters that controlled the stoichiometry of the BZN films. The bismuth content decreased as the target to substrate distance was decreased from 7 cm to 4 cm, while the zinc content remained unchanged. The decrease in bismuth content was probably caused by resputtering of the bismuth from the growing film. Changing the chamber pressure from 100 mTorr to 400 mTorr dramatically changed the film composition and increased both the bismuth and zinc content in the film to a composition

that was close to the stoichiometry of the target. A model is presented to account for these composition changes.

The films crystallized into the cubic pyrochlore structure at 450 °C on the Pt/ La, Pt alloy (5 vol % La in Pt)/ $La_2O_3/SiO_2/Si$ wafers. All of the films grown in this study show smaller lattice parameters than bulk BZN samples.

The crystalline films have dielectric constants between 70 and 138 and a tan $\delta <$ 0.007 over a wide range of compositions. The temperature coefficient of capacitance, TCC, was strongly dependent on the crystallinity of the films and ranged between 200 ppm/°C to –200 ppm/°C for amorphous films and well crystallized films, respectively, when measured between 100 °C to –50 °C. The loss was < 1 % over the temperature range measured for TCC. Some of the compositions of films with permittivities ~100 showed TCC between 12 ppm/°C to –22 ppm/°C, which make them promising for NPO, negative, positive, but almost zero temperature coefficient of capacitance, dielectrics. The PLD films show low leakage currents of 2×10^{-8} A/cm^2 at 200 kV/cm. A preliminary study using highly accelerated lifetime testing, HALT, was completed on amorphous films to determine the dc reliability and degradation. These materials should be useful for high capacitance density, temperature and frequency stable capacitors.

Table of Contents

List of Figures……..…….……vii
List of Tables……...……..xii
Acknowledgements……..……..….xiii
Chapter 1 Introduction and Statement of Goals..... 1
1.1 Introduction..... 1
1.2 Statement of Goals..... 2
Chapter 2 Literature Survey..... 4
2.1 Introduction..... 4
2.2 Pulsed Laser Deposition 4
2.2.1 Background on Pulsed Laser Deposition..... 4
2.2.2 Excimer Lasers..... 5
2.2.3 Laser Target Interactions 6
2.2.4 Characteristics of Plasma Plume..... 7
2.2.5 Control of Stoichiometry 10
2.2.6 Particulate Generation..... 11
2.2.7 Film Nucleation and Microstructure of Vapor Deposited Thin Films..... 12
2.3 Bismuth- Zinc-Niobate 15
2.3.1 Crystallography of Bismuth-Zinc-Niobate 15
2.3.2 Crystal Structure of $Bi_2Zn_{2/3}Nb_{4/3}O_7$ 16
2.3.3 Crystal Structure of $Bi_{1.5}Zn_{1.0}Nb_{1.5}O_7$..... 18
2.4 Bismuth-Zinc-Niobate Thin Films..... 21
Chapter 3 Experimental Procedure 30
3.1 Description of Deposition Equipment 30
3.1.1 Excimer Laser 30
3.1.2 Laser Optics 30
3.1.3 Targets..... 31
3.1.4 Substrate Mounting..... 32
3.1.5 Vacuum System 32
3.2 Substrates 33
3.3 Deposition of BZN..... 37
3.4 Top Electrode Deposition and Fabrication 39
3.5 X-ray Analysis 41
3.6 Electrical Property Analysis 42
3.7 HALT Measurements..... 43
3.8 Composition Characterization 44
3.9 Morphology Characterization 44
4.1 Deposition Study..... 45
4.1.1 Target to Substrate Distance 45
4.1.2 Deposition Pressure 49
4.1.3 Laser Frequency..... 54
4.2 Composition of BZN Thin Films..... 56
4.2.1 Composition of BZN Thin Films as a Function of Target Composition 56

4.2.2 Composition as a Function of Laser Exposure 60
4.2.3 Composition as a Function of Target to Substrate Distance..... 61
4.2.4 Composition as a Function of Deposition Temperature 63
4.2.5 Composition as Function of Laser Frequency 65
4.2.6 Composition Summary 68
4.3 Phase Formation..... 71
4.3.1 Crystallization Temperature as a Function of Chamber Pressure..... 72
4.3.2 Effects of Substrate on the Crystallization Temperature 76
4.4 Dielectric Properties..... 79
4.4.1 Permittivity as a Function of Deposition Temperature..... 79
4.4.2 Dielectric Properties as a Function of Chamber Pressure..... 83
4.4.3 Permittivity as a Function of Target to Substrate Distance 85
4.4.4 Temperature Coefficient of Capacitance 86
4.4.5 Low Temperature Dielectric Behavior for Amorphous Films..... 88
4.4.6 Leakage Behavior for Amorphous Films..... 89
4.4.7 Tunability..... 92
4.4.8 Effects of Forming Gas Annealing on Dielectric Properties 93
4.5 Degradation Behavior of BZN Thin Films 95
Chapter 5 Conclusions and Future Work..... 101
5.1 Conclusions..... 101
5.2 Future Work..... 104
Appendix..... 108
References……..…….111

List of Figures

Figure 2.1 Optical spectra of the laser plume produced from a YBCO target at different oxygen pressures at a laser fluence of 1.5 J/cm^2. 8
Figure 2.2 Velocity distributions of ground state Y, Ba, Cu, and Ba^+ as determined by optical absorption (target to substrate distance-5 cm and laser fluence of 1 J/cm^2). 8
Figure 2.3 Shows the plasma plume deposition geometry, where z is the deposition axis and x is the distance from the deposition axis. 9
Figure 2.4 Three basic modes of thin film growth. 13
Figure 2.5 Schematic showing the superposition of physical processes that establishes the structural zones. 15
Figure 2.6 Crystal structure for BZN-2/3. 17
Figure 2.7 Crystal structure of BZN-2/3 illustrating the two possible positions for the zinc atoms. 18
Figure 2.8 Crystal structure for the $Bi_{1.5}Zn_{0.92}Nb_{1.5}O_{6.92}$ composition. 19
Figure 2.9 Dielectric constant and loss as a function of temperature for 2, 10, 30, and 100 kHz from left to right for BZN-1. 20
Figure 2.10 Dielectric constant and loss as a function of temperature for 2, 10, 30, and 100 kHz from left to right for BZN-2/3. 21
Figure 2.11 Dielectric properties measured from 1 kHz to 1 MHz for BZN-2/3 thin films deposited on MgO substrates at 400-600 °C for 30 minutes. 22
Figure 2.12 Dielectric constant as a function of firing temperature for BZN-1, BZN-0.5, and BZN-2/3 thin films.' 23
Figure 2.13 Capacitance as a function of thickness for BZN-1 films produced by MOD. 24
Figure 2.14 Temperature coefficient of capacitance as a function of firing temperature for MOD films.' 25
Figure 2.15 Temperature dependence of the dielectric constant and loss for BZN-1 and BZN-0.5 films produced by MOD. 25
Figure 2.16 Temperature dependence of the dielectric constant for BZN-2/3 measured at 0.5, 1, 2, 5, 10 kHz. For the dielectric constant curve, the top curve was measured at the lowest frequency and for the loss tangent curve the top curve was measured at the highest frequency. 26
Figure 2.17 Normalized dielectric constant as a function of dc bias field for BZN-1 at different firing temperatures measured at 10 kHz. 26
Figure 2.18 Normalized permittivity as a function of bias field measured at different temperatures for a BZN-1 film produced by MOD and fired at 750 °C. 27
Figure 2.19 Permittivity as a function of bias field at 77 K for BZN-0.5 film produced by MOD at a firing temperature of 650 °C. 27
Figure 3.1 PLD chamber schematic. 31
Figure 3.2 Substrate heater. 32
Figure 3.3 X-ray diffraction pattern for the BZN-0.5 target. Indexed peaks are from the cubic pyrochlore phase. BN stands for $BiNbO_4$ (PDF: 16-0295). 35

Figure 3.4 X-ray diffraction pattern for the BZN-1 target. Indexed peaks are from the cubic pyrochlore phase. 36
Figure 3.5 X-ray diffraction pattern of the BZN-2/3 target. Indexed peaks are from the monoclinic phase. 37
Figure 3.6 Nova substrate heated to 650 °C for 5 minutes in vacuum. 38
Figure 3.7 Nova substrate with BZN film deposited at a substrate temperature of 250 °C, at a target to substrate distance of 7 cm, a laser frequency of 3 Hz, a chamber pressure of 200 mTorr, and a deposition time of 15 seconds. The film was then heated to 650 °C and held at 650 °C for 30 minutes. 39
Figure 3.8 Schematic of the chip package. 42
Figure 4.1 Deposition rate as a function of target to substrate distance for films grown using the $Bi_2Zn_{2/3}Nb_{4/3}O_7$ target, a substrate temperature of 550 °C, a laser frequency of 10 Hz, and a chamber pressure of 200 mTorr. 46
Figure 4.2 Plasma plume as a function of target to substrate distance: a) 4 cm; b) 5 cm; c) 6 cm; d) 7 cm. The images were taken using the BZN-1 target at a chamber pressure of 100 mTorr. 48
Figure 4.3 Deposition rate as a function of chamber pressure (of 10 % O_3 and 90 % O_2) for films deposited at 550 °C, at a target to substrate distance of 7 cm, and at a laser frequency of 3 Hz. 50
Figure 4.4 Plasma plume as a function of chamber pressure: a) 50 mTorr; b) 100 mTorr; c) 200 mTorr; d) 300 mTorr; e) 400 mTorr. 52
Figure 4.5 Surface morphology as a function of chamber pressure: a) 100 mTorr; b) 200 mTorr; c) 300 mTorr; d) 400 mTorr. The films were deposited using the BZN-1 target, on Nova substrates, at a target to substrate distance of 7 cm, a substrate temperature of 550 °C, and a laser frequency of 3 Hz. Films were ~ 300 nm thick. 53
Figure 4.6 TEM cross sectional image of a film deposited using the BZN-1.0 target, at a substrate temperature of 550 °C, a chamber pressure of 100 mTorr, a target to substrate distance of 7 cm, and a laser frequency of 3 Hz. Image courtesy of Dr. Jaenam Kim. 53
Figure 4.7 X-ray diffraction patterns as a function of chamber pressure for films grown from the BZN-1.0 target, at a substrate temperature of 550 °C, a laser frequency of 3 Hz, and a target to substrate distance of 7 cm. * denotes substrate peaks and BN stands for $BiNbO_4$. The amorphous hump around 12° 2θ is from the substrate holder. Indexed peaks are from the cubic pyrochlore phase. a) 50 mTorr, b) 100 mTorr, c) 200 mTorr, d) 300 mTorr, e) 400 mTorr. 54
Figure 4.8 Laser frequency as a function of deposition rate for films grown using the BZN-1 + 0.11 mol Bi_2O_3 target, at a target to substrate distance of 7 cm, a substrate temperature of 550 °C, and a chamber pressure of 100 mTorr. 55
Figure 4.9 X-Ray diffraction patterns as a function of laser frequency for films grown from the BZN-1.0 + 0.11 mol Bi_2O_3 target, on Nova substrates, at a target to substrate distance of 7 cm, a substrate temperature of 550 °C, and a chamber pressure of 100 mTorr. * denotes substrate peaks. The amorphous hump around 12° 2θ is from the substrate holder. Indexed peaks are from the cubic pyrochlore phase. 55

Figure 4.10 X-ray diffraction patterns for films deposited using BZN-0.5 and BZN-1.0 targets, on Nova substrates, at a substrate temperature of 550 °C, a target to substrate distance of 7 cm, a laser frequency of 3 Hz, and a chamber pressure of 100 mTorr. * denotes substrate peaks. The amorphous hump around 12° 2θ is from the substrate holder. Indexed peaks are from the cubic pyrochlore phase. 57
Figure 4.11 X-ray diffraction patterns as a function of target composition for films grown on Nova substrates, at a substrate temperature of 550 °C, a target to substrate distance of 7 cm, a laser frequency of 3 Hz, and a chamber pressure of 100 mTorr. * denotes substrate peaks. The amorphous hump around 12° 2θ is from the substrate holder. Indexed peaks are from the cubic pyrochlore phase. 59
Figure 4.12 X-ray diffraction patterns as function of target composition for films grown on Nova substrates, at a substrate temperature of 500 °C, a target to substrate distance of 7 cm, a laser frequency of 3 Hz, and a chamber pressure of 100 mTorr. * denotes substrate peaks and BN stands for $BiNbO_4$. The amorphous hump around 12° 2θ is from the substrate holder. Indexed peaks are from the cubic pyrochlore phase. 60
Figure 4.13 Lattice parameter as a function of chamber pressure for films grown from the BZN-1.0 target, at a substrate temperature of 550 °C, a laser frequency of 3 Hz, and a target to substrate distance of 7 cm. 68
Figure 4.14 Lattice parameter as a function of zinc content for films grown at different chamber pressures. 69
Figure 4.15 Schematic of the bismuth and zinc distributions as a function of chamber pressure and target to substrate distance. 71
Figure 4.16 X-ray diffraction patterns for films deposited using the BZN-1.0 target, on Nova substrates, at a laser frequency of 10 Hz, a target to substrate distance of 7 cm, and a chamber pressure of 200 mTorr. * denotes substrate peaks. The amorphous hump around 12° 2θ is from the substrate holder. Indexed peaks are from the cubic pyrochlore phase. 72
Figure 4.17 X-ray diffraction pattern for films deposited using the BZN-1.0 target, on Nova substrates, a target to substrate distance of 7 cm, a laser frequency of 3 Hz, and at a chamber pressure of 100 mTorr. * denotes substrate peaks. The amorphous hump around 12 ° 2θ is from the substrate holder. Indexed peaks are from the cubic pyrochlore phase. 73
Figure 4.18 X-ray diffraction patterns as a function of laser frequency for films deposited using the BZN-1.0 target, on Nova substrates, a target to substrate distance of 7 cm, and a chamber pressure of 100 mTorr. * denotes substrate peaks. The amorphous hump around 12° 2θ is from the substrate holder. Indexed peaks are from the cubic pyrochlore phase. 74
Figure 4.19 AFM images as a function of deposition temperature for films grown from the BZN-1.0 target, on Nova substrates, at a chamber pressure of 100 mTorr, a laser frequency of 3 Hz, and a target to substrate distance of 7 cm. 76
Figure 4.20 X-ray diffraction patterns for two of the Pt/ La, Pt alloy (5 vol % La in Pt)/ $La_2O_3/SiO_2/Si$ wafers. The amorphous hump around 12° 2θ is from the substrate holder. 78

Figure 4.21 X-ray diffraction pattern for two films deposited using the BZN-1.0 + 0.15 mol Bi_2O_3 target, at a deposition temperature of 450 °C, a laser frequency of 3 Hz, a chamber pressure of 100 mTorr, and a target to substrate distance of 7 cm. The bottom pattern was deposited on the 1st Pt/ La, Pt alloy (5 vol % La in Pt)/ $La_2O_3/SiO_2/Si$ wafer and the top pattern was deposited on the 2nd Pt/ La, Pt alloy (5 vol % La in Pt)/ $La_2O_3/SiO_2/Si$ wafer. * denotes substrate peaks. The amorphous hump around 12° 2θ is from the substrate holder. Indexed peaks are from the cubic pyrochlore phase. 78
Figure 4.22 X-ray diffraction patterns for films as a function of deposition temperature, on the 1st Pt/ La, Pt alloy (5 vol % La in Pt)/ $La_2O_3/SiO_2/Si$ wafer, using the BZN-1.0 + 0.15 mol target, at a chamber pressure of 100 mTorr, a laser frequency of 3 Hz, and a target to substrate distance of 7 cm. * denotes substrate peaks. The amorphous hump around 12° 2θ is from the substrate holder. Indexed peaks are from the cubic pyrochlore phase. 79
Figure 4.23 Permittivity as a function of deposition temperature for films deposited using the base composition of BZN-1.0, on Nova substrates, at a target to substrate distance of 7 cm, and a laser frequency of 3 Hz. The films deposited at 450 °C were deposited using a chamber pressure of 50 mTorr. The films deposited at 500 °C and 550 °C were deposited using a chamber pressure of 100 mTorr. The measurements were completed at room temperature using a frequency of 10 kHz and an oscillation voltage of 0.03 V..... 80
Figure 4.24 Permittivity as a function of deposition temperature for films deposited using targets with the base composition of BZN-0.5. The films were deposited at a target to substrate distance of 7 cm and a laser frequency of 3 Hz. The films deposited at 450 °C were deposited using a chamber pressure of 50 mTorr and the films deposited at 500 °C and 550 °C were deposited using a chamber pressure of 100 mTorr. The measurements were completed at room temperature using a frequency of 10 kHz and an oscillation voltage of 0.03 V..... 83
Figure 4.25 Permittivity as a function of chamber pressure for films grown from the BZN-1.0 target, at a substrate temperature of 550 °C, a target to substrate distance of 7 cm, and a laser frequency of 3 Hz. The measurements were completed at room temperature using a frequency of 10 kHz and an oscillation voltage of 0.03 V..... 84
Figure 4.26 Permittivity as a function of target to substrate distance, for films grown using the BZN-1.0 + 0.15 mol Bi_2O_3 target, at a substrate temperature of 550 °C, a chamber pressure of 100 mTorr, and a laser frequency of 3 Hz. The measurements were completed at room temperature using a frequency of 10 kHz and an oscillation voltage of 0.03 V..... 85
Figure 4.27 Temperature dependence of the dielectric constant for films grown using the BZN-1.0 + 0.11 mol Bi_2O_3 target, on Nova substrates, at different substrate temperatures, at a target to substrate distance of 7 cm, a laser frequency of 3 Hz, and a chamber pressure of 100 mTorr. The measurements were completed at a frequency of 10 kHz and an oscillation voltage of 0.03 V. 86

Figure 4.28 TCC as a function of deposition temperature for films deposited using the base target composition of BZN-1.0. The films were deposited on Nova substrates, at a target to substrate distance of 7 cm, and a laser frequency of 3 Hz. The film deposited at 450 °C using the BZN-1.0 + 0.15 mol target was deposited at a chamber pressure of 50 mTorr. The other films were deposited at a chamber pressure of 100 mTorr. 87
Figure 4.29 TCC as a function of deposition for films with a base composition of BZN-0.5. The films were deposited on Nova substrates, at a target to substrate distance of 7 cm, a laser frequency of 3 Hz, and a chamber pressure of 100 mTorr. 88
Figure 4.30 Dielectric constant as a function of temperature for a film deposited using the BZN-1 + 0.15 mol Bi_2O_3 target, on the 1st Pt/ La, Pt alloy (5 vol % La in Pt)/ $La_2O_3/SiO_2/Si$ wafer, at a deposition temperature of 450 °C, a target to substrate distance of 7 cm, a laser frequency of 3 Hz, and a chamber pressure of 100 mTorr. 89
Figure 4.31 Leakage current as a function of time for positive and negative bias on a film grown using the BZN-1.0 + 0.15 mol Bi_2O_3 target, on the 1st Pt/ La, Pt alloy (5 vol % La in Pt)/ $La_2O_3/SiO_2/Si$ wafer, at a deposition temperature of 450 °C, at a target to substrate distance of 7 cm, a laser frequency of 3 Hz, and a chamber pressure of 100 mTorr. 91
Figure 4.32 Leakage current as a function of electric field for positive and negative fields for a film grown using the BZN-1.0 + 0.15 mol Bi_2O_3 target, on the 1st Pt/ La, Pt alloy (5 vol % La in Pt)/ $La_2O_3/SiO_2/Si$ wafer, at a deposition temperature of 450 °C, at a target to substrate distance of 7 cm, a laser frequency of 3 Hz, and a chamber pressure of 100 mTorr. Leakage currents were measured 90 seconds after increasing the field. 91
Figure 4.33 Dielectric constant as a function of electric field for films deposited using the BZN-1.0 + 0.11 mol Bi_2O_3 target, on Nova substrates, at a target to substrate distance of 7 cm, a laser frequency of 3 Hz, and a chamber pressure of 100 mTorr. Note, the film deposited at 550 °C was only cycled once as a function of electric field. The other films were cycled twice. 93
Figure 4.34 X-ray diffraction patterns before and after forming gas anneal on a film grown using the BZN-1.0 target, on Nova substrates, at a substrate temperature of 650 °C, a target to substrate distance of 7 cm, a laser frequency of 10 Hz, and a chamber pressure of 200 mTorr. * denotes substrate peaks. The amorphous hump around 12° 2θ is from the substrate holder. Indexed peaks from the cubic pyrochlore phase. 95
Figure 4.35 Current as a function of time, illustrating the failure of the capacitors. 97
Figure 4.36 The time to failure as a function of the cumulative probability of failure for HALT conditions of 100 °C and a voltage of 10 V. 98
Figure 4.37 The time to failure as a function of the cumulative probability of failure for two samples tested at 85 °C and 10 V. 99
Figure 4.38 The MTF as a function of 1/Temperature. 100
Figure 5.1 Summary of dielectric properties for PLD films and MOD films.' 103
Figure A.1 Probability of failure as a function of time illustrating the raw data and the calculated data. 110

List of Tables

Table 2.1 Comparison of results of HALT for different studies on multilayer capacitors. 29
Table 3.1 Summary of the target compositions batched for this study. 37
Table 4.1 Target composition and film composition for films deposited at 550 °C, at a pressure of 100 mTorr, a target to substrate distance of 7 cm, and a laser frequency of 3 Hz. 57
Table 4.2 Target composition and film composition for targets with excess bismuth. 58
Table 4.3 Film composition as a function of laser exposure of the target. 61
Table 4.4 Film composition as a function of target to substrate distance. 61
Table 4.5 The melting points for some of the BZN species. 64
Table 4.6 The temperature of vaporization for BZN constituents." 64
Table 4.7 Film composition as a function of deposition temperature 65
Table 4.8 Film composition as a function of laser frequency. 65
Table 4.9 Film composition as a function of chamber pressure. 66
Table 4.10 Dielectric properties before and after forming gas annealing 95
Table 4.11 Results of the HALT for PLD films. 99

Acknowledgements

I would like to thank my advisor, Dr. Susan Trolier-McKinstry, for giving me the opportunity to work in her group and play with all of the new toys. I want to thank Motorola and the Semiconductor Research Corporation for providing the funding for this work. I would like to thank Dr. Michael Lanagan and Dr. Russell Messier for serving on my committee.

I would like to thank the following people, who I've had the opportunity to work with, for helping me along my career: Jim Sommerville, Ed Labarge, Rodi, Rita Baranwal, and Dave Miller. They were all wonderful mentors and encouraged me to reach my fullest potential. I would not be where I am without them.

I want to thank the MRL support staff for all of the help and guidance they provided me in this work. I would especially like to thank Bill Drawl for his help and guidance on issues in and outside of the lab. I want to especially thank Takeshi Yoshimura for all of his patience and help teaching me about PLD.

Lastly, I would like to thank my husband Brian for putting up with me through this entire thesis. I am incredibly lucky to have him in my life and here with me at Penn State.

Chapter 1 Introduction and Statement of Goals

1.1 Introduction

As clock rates and integrated circuit gate density increase, discrete chip capacitors do not satisfy the decoupling requirements for high current switching at high frequencies.[1] In addition, some engineers believe that discrete surface mounted passive components are also reaching their limits in performance, cost, reliability, and size. Certainly, the use of integral passives reduces assembly costs and shrinks the required board size.[1,2] Because low value ceramic chip capacitors (<1000 pF) constitute about 40% of all capacitors used in handheld applications, and because they may eliminate some of the above complications, they are being considered for replacement by integral capacitors.[3] These factors are driving researchers to find new materials that can be used in these applications.

To integrate a decoupling capacitor in an integrated circuit, the processing temperature should be below 450 °C. This is mandated because the dielectric would most likely be deposited after the interconnect processing in a standard complementary metal oxide silicon, CMOS, fabrication.[4] Thus, it would be imperative that the dielectric deposition does not perturb any of the underlying layers.

New dielectric materials with high and stable permittivities, low leakage, low dissipation factors, and low processing temperatures are required for such integrated capacitors. The Bi_2O_3-ZnO-Nb_2O_5 (BZN) pyrochlore ceramic system has been shown to exhibit these properties in bulk samples and thin films made by metal organic deposition,

MOD, and pulsed laser deposition, PLD. [5,6,7] BZN thin films also show a field tunability of the dielectric constant.[6] The processing of films by PLD and MOD has been able to produce crystalline films at temperatures of 475 °C and 550 °C, respectively.[6,7] However, many unanswered questions about processing-composition-microstructure-property relations in vapor deposited BZN films remain.

1.2 Statement of Goals

The goals of this work can be divided into the following categories:

1. Development of the deposition parameters to produce single-phase compositions of bismuth-zinc-niobate (BZN) using pulsed laser deposition. This study focused on the following two compositions: $Bi_{1.5}Zn_{1.0}Nb_{1.5}O_7$ (BZN-1) and $Bi_{1.5}Zn_{0.5}Nb_{1.5}O_{6.5}$ (BZN-0.5). This is the first study to make the BZN-1 and BZN-0.5 compositions by pulsed laser deposition. This study focused on the interactions between the growth temperature, the chamber pressure, and laser frequency to determine the parameters required to produce single-phase compositions. These results should be transferable to other physical vapor phase deposition techniques.

2. Determination of the film composition as a function of target composition, target to substrate distance, chamber pressure, substrate temperature, and laser frequency. This should elucidate the relative roles of bombardment, resputtering, evaporation, and the distribution of species within the plume in controlling composition. The composition was measured using Rutherford Backscattering analysis.

3. Characterization of the dielectric properties of the BZN thin films as a function of composition. The specific focus was on the effects of bismuth and zinc stoichiometry on the dielectric properties. The dielectric properties were measured as a function of temperature, frequency, and applied voltage. A preliminary study of the reliability and degradation was completed using highly accelerated lifetime testing, HALT.

Chapter 2 Literature Survey

2.1 Introduction

This thesis focused on producing bismuth-zinc-niobate thin films by pulsed laser deposition. This review describes the background on pulsed laser deposition and the bismuth-zinc-niobate system.

2.2 Pulsed Laser Deposition

A review is given below on the background of pulsed laser deposition, excimer lasers, laser target interactions, the characteristics of laser-induced plasmas, particles generated in the plasma, and nucleation and growth mechanisms in thin films.

2.2.1 Background on Pulsed Laser Deposition

The first thin film growth using lasers dates back to 1965 with the work of Smith and Turner in which they were able to deposit semiconductors, dielectrics, chalcogenides, and organometallics using a ruby laser.[8] There were only a few groups working on the laser deposition of materials and less than 100 papers were published on the topic in the 1960's.[9]

By the middle of the 1970's, there were two major developments in laser deposition. The first breakthrough was in the development of the Q-switch. The Q-switch provided short pulses of laser energy and a high energy density of laser power. The generation of high peak powers led to congruent evaporation, which was observed in several systems from ternary compounds to low-temperature superconductors.[10] The second advancement was the development of a high efficiency second harmonic

generator.[9] The new second harmonic generator was able to create shorter wavelength radiation, which allowed the absorption depth to be shallower and particles from the target were reduced.

By the early 1980's PLD was becoming a viable physical vapor deposition, PVD, technique. For the first time epitaxial semiconductor films, heterostructures, and superlattices grown by PLD showed qualities comparable to those grown by molecular beam epitaxy, MBE.[11,12] PLD became one of the dominant deposition techniques for the development of high temperature superconductors.

2.2.2 Excimer Lasers

Excimer lasers are the most commonly used laser for PLD systems. Excimer lasers produce radiation directly in the UV region. Laser wavelengths between 200 and 400 nm are typically the most useful for thin film growth of nonmetallic materials because insulators exhibit strong absorption in this regime.[13] Excimer lasers can produce high outputs greater than 1 J/pulse and repetition rates of several hundred hertz. KrF and XeCl are two of the most commonly used excimer lasers. KrF is the highest gain system for electrically discharged pumped excimer lasers.[9] A KrF laser with a wavelength of 248 nm was used in this study.

For the case of the KrF laser, excimer molecules are formed in a gas mixture of their component gases. Energy is pumped into the gas mixture through avalanche electric discharge excitation and the pumping creates ionic and electronically excited species that react chemically and produce the excimer molecules.[9] After the excimer molecule is formed, it will decay spontaneously with a lifetime of ~ 2.5 ns.[9] For the laser to produce output energies of several hundred millijoules per laser pulse, there must be an excimer

molecule population on the order of $10^{15}/cm^3$.[9] This is accomplished by having discharge electrodes that are spaced between 2-3 cm apart, which creates discharge voltages between 20-45 kV.[9]

2.2.3 Laser Target Interactions

There are three main regimes in a laser ablation process: 1) interaction of the laser with the target, 2) plasma formation and interaction of the laser beam with the plasma plume, and 3) adiabatic expansion of plasma.[14] In the first step, the laser beam hits the target and the photons are absorbed by the surface and a combination of melting and ablation of the target occurs. In low melting temperature solids, this results in surface melting. It is somewhat less clear that melting occurs for high melting temperature compound such as some oxides, though the surface temperature certainly rises appreciably. The surface temperature of $YBa_2Cu_3O_7$ targets is ~2000-3200 K after the laser hits the target.[14]

After the laser hits the target, there is the formation of the plasma plume, which consists of ions, molecules, neutral particles, and atoms.[14] The plasma plume expands and moves away from the target. The laser beam also interacts with the plasma plume causing further ionization of the species in the plume.

The third regime occurs after the end of the laser pulse. The plume undergoes adiabatic expansion in this regime. The thermal energy of the plasma is rapidly converted to kinetic energy inside the plasma, which leads to very high expansion velocities of the plume.[14]

2.2.4 Characteristics of Plasma Plume

Typical plasma plume temperatures which can be measured by emission spectroscopy during the initial expansion of the plume are ~10,000 K, which is well above the boiling points of most materials (≤ 3000 K).[9] It can be very difficult to investigate the components of the plasma plume because none of the techniques can measure all of the species inside of the plume at one time. The most commonly used experimental methods for plasma studies are optical diagnostics such as time-resolved emission spectroscopy or laser-induced fluorescence.[15] Some of the other techniques available are time of flight mass spectroscopy, ion probes, and high-speed photography and imaging.

Optical emission spectroscopy can be set up using a photodiode and a quartz crystal monitor, and is principally used for identifying the species in the laser plume from tabulated atomic lines and molecular bands.[9] Figure 2.1 shows the optical spectra for plasmas at different pressures for $Y_1Ba_2Cu_3O_{7-x}$, YBCO. As the oxygen pressure was increased, the intensity of the oxide components in the plasma plume increased. This indicates that the species inside the plume become oxidized as oxygen is introduced to the chamber.

The velocity distributions of various species in the plume can also be determined. Figure 2.2 shows the velocity distributions for a plume produced using an YBCO target in vacuum. The copper ground state species, the lightest species in the plume, show the broadest velocity distribution of the species. The barium ground state species, the heaviest species, show the slowest average velocity. The ionized barium species show higher velocities than the ground state barium species.[17]

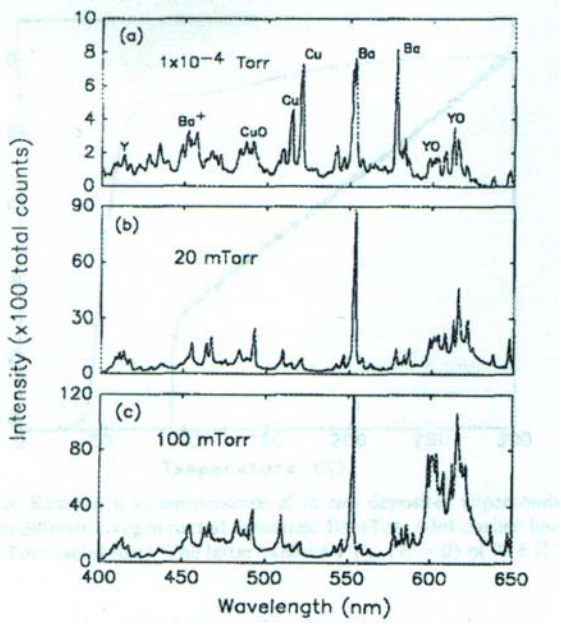

Figure 2.1 Optical spectra of the laser plume produced from a YBCO target at different oxygen pressures at a laser fluence of 1.5 J/cm^2.[16]

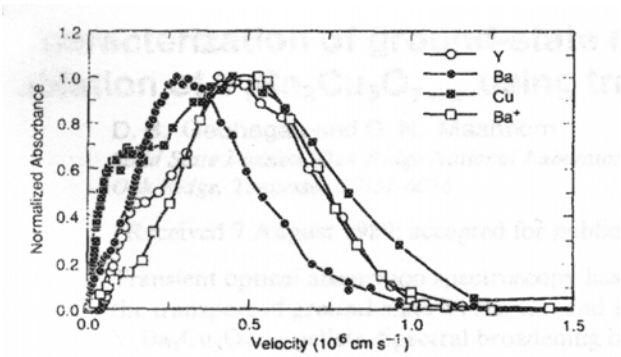

Figure 2.2 Velocity distributions of ground state Y, Ba, Cu, and Ba^+ as determined by optical absorption (target to substrate distance-5 cm and laser fluence of 1 J/cm^2).[17]

There are two main categories for measurements of the angular distribution of the plume, film-based measurements or probe-based measurements. Film based methods are the most widely used method for determining the angular distribution. There are two major assumptions used to determine the angular distribution using a film method: the particle sticking coefficient is unity and there is no resputtering of the film by the incident

particle.[9] The angular distribution using a film is measured ex situ, by measuring the thickness of the deposited film as a function of position from the deposition axis. Figure 2.3 shows the deposition geometry used to determine the angular distribution, where z is the deposition axis and x is the distance from the deposition axis. It is found that PLD results in sharply peaked thickness distributions with the functional form of $\sim\cos^p \theta$, with $8 < p < 14$.[18] In contrast, thermal evaporation sources can have thickness profiles of $\sim\cos^4 \theta$.[18] Thus, PLD deposits over fairly small areas, unless special setups are used to raster the plume over large areas.[19]

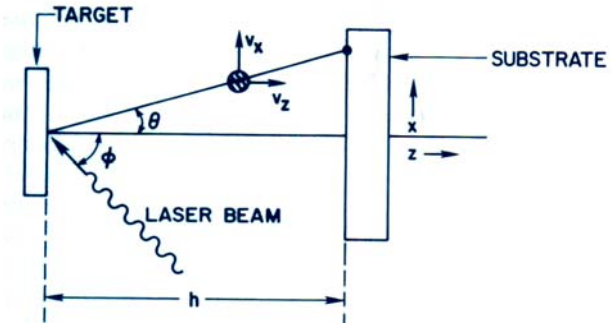

Figure 2.3 Shows the plasma plume deposition geometry, where z is the deposition axis and x is the distance from the deposition axis.[9]

Background gases such as oxygen, ozone, and nitrogen can be used to incorporate gas into the growing film and dramatically change the characteristics of the plasma. The background gas pressure can cause the following effects: (1) an increase in fluorescence due to collisions on the expansion front and interplume collisions, (2) a sharpening of the plume boundary, which indicates a shock front, (3) a slowing of the plume relative to the propagation in vacuum, (4) confinement of the plume.[9] The addition of background gas decreases the energy of the ablated species because of an increased number of collisions with the gas.[9] This can reduce the resputtering of the growing film. Controlling the

effects of background gases are critical to producing stoichiometric films and will be further discussed in the next section.

2.2.5 Control of Stoichiometry

One of the major advantages to using PLD over other vapor deposition techniques is the ability to grow films from complex multicomponent targets and produce films with the same stoichiometry as the target. The control of stoichiometry of the film in PLD is extremely complex, and there are many factors that can cause variations in the composition of the film from the target composition. The variations in composition can be broken into three main categories: target, plume, and growth effects.[20] The target can cause stoichiometric variations in the film if there is preferential ablation from the target, segregation on the target surface caused by phase transformations on the target, or thermal evaporation caused by being below the ablation threshold for the material.[21] A second factor that can be important in the plume is the relative distributions of ablated versus evaporated components of the plume. As was shown by Venkatesan et al., under some deposition conditions the plume consists of two components, an ablated component and an evaporated component.[22] The ablated component has the stoichiometry of the target, but the evaporated component is non-stoichiometric.[22] In this study, it is believed that the target effects are negligible for the BZN system. The fluence used in this study should be above the ablation threshold.

The interactions in the plasma plume causes variations in the film composition if the different species in the plume have different angular distributions. The different angular distributions can be caused by different masses of the species and different charge states of the species in the plume.

The angular distribution of species is also affected by the use of background gases. The collision of plume species with background gas molecules would be expected to preferentially broaden the angular distribution of the low-mass species, since the smallest collisionally induced momentum changes would be likely to result in large velocity changes.[9] Similarly, the trajectories of high mass plume particles are relatively unaffected by background gas collisions.[9] However, it is possible that these effects could be overwhelmed by the narrowing of the plume with increasing pressure.

The third main cause of the films having different stoichiometries from the target can occur during the growth of the film at the substrate. The species may have different sticking coefficients, there may be preferential evaporation from the substrate, or resputtering may occur at the substrate.[20] The energy of the species reaching the substrate can range between 1 to 1000 eV, which is enough energy to sputter atoms off of the substrate.[9] It is critical to control all of these parameters if stoichiometric films are to be grown using PLD.

2.2.6 Particulate Generation

One of the biggest disadvantages to using PLD in commercial applications is the formation of particles during deposition. There are several different mechanisms that can cause the formation of particles. Particles can be formed from (1) defects in the target surface that are removed during the target-laser interactions, (2) rapid expansion of trapped gas bubbles underneath the target surface, which causes forcible ejection of surface material, (3) splashing of the molten layer which is caused by the subsurface superheated layer, (4) condensation in the vapor due to supersaturation.[9] Particles that are formed from the solid target tend to be irregular in shape, while particles formed in

the liquid state tend to be spherical in shape, and the particles formed in the vapor phase may be spherical or polyhedral. Particles formed in the solid and liquid phases tend to have sizes in the submicron to micron size scale, and particles formed in the vapor phase tend to have sizes in the nanometer size scale.[9]

There has been extensive work to eliminate particles from being deposited onto the growing film. One method uses velocity filtration of the plasma by placing a rotating vane particle filter in the plume.[23] This method is based on the fact that the particulates are slower than the atomic and molecular species in the plasma plume. Using velocity filtration, Pechen et al. were able to reduce the particle density in $YBa_2Cu_3O_{7-x}$, YBCO, films by a factor of 10^5. [24] Another method used to reduce the particles is to use off-axis geometry for the growing film. In this method, the substrate is placed at 90° to the plume. This method works to decrease the number of particles because the macroparticles are constrained to travel along their initial trajectory direction, while the atomic and molecular species are scattered in the plume.[9] One of the disadvantages to this method is that the deposition rate is reduced.

2.2.7 Film Nucleation and Microstructure of Vapor Deposited Thin Films

There are three basic growth modes for initial film formation: island (or Volmer-Weber), layer (or Frank-van der Merwe), and Stranski-Krastanov.[25] Figure 2.4 shows the three basic growth modes for initial film growth.

Island growth occurs when small clusters nucleate on the substrate and grow in three dimensions to form islands on the surface of the substrate. Island growth typically occurs when atoms or molecules are more strongly bound to each other than to the

substrate surface and is observed in metals deposited on insulators, alkali halide crystals, and graphite.[25]

Layer growth occurs when the smallest nucleus forms in two dimensions, which results in the formation of sheets. This is typically observed when the atoms are more strongly bound to the substrate than to each other.[25] Layer growth is observed in some cases of epitaxial growth.

The third growth mechanism is a combination of island and layer growth. This mechanism occurs by first forming layers on the substrate. Then layer growth stops and islands start to form on the surface of the layers. The transition from layer growth to island growth is not completely understood. This growth mode is observed in metal films grown on metal substrates and metal films grown on semiconductors.[25]

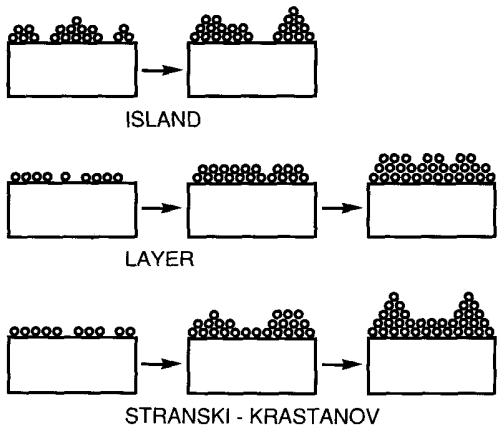

Figure 2.4 Three basic modes of thin film growth.[25]

After the initial nucleation of the film, the microstructure of the film is controlled by several different mechanisms. Thin films prepared by physical vapor deposition show a wide range of microstructures and properties, which are highly dependent on the deposition conditions.[26] There are several different structure zone models, SZM, that have been used to classify the morphology of films as a function essentially of adatom

mobility.[27] SZMs have been used to relate the microstructure of the thin films to T/T_m, where T is the deposition temperature and T_m is the melting temperature of the material and the deposition pressure. Figure 2.5 shows the SZM proposed by J. Thornton for sputtered metals as a function of T/T_m and pressure. Thornton proposed there were four different zones (1, T, 2, 3) within the film growth conditions.

The Zone 1 structures are formed by amorphous and crystalline films and are caused by shadowing effects. There is limited adatom surface diffusion, because of the reduced temperature. As a result, incoming atoms tend to stick where they first strike, yielding columnar structures.[25,28] Zone 1 structures can be observed at higher substrate temperatures and higher pressures when there is not enough adatom mobility on the surface of the film. Zone 1and Zone T structures are strongly affected by the deposition pressure. As the deposition pressure is increased, the energy of the species in the plasma decreases due to thermalization, giving less adatom mobility to the species. Zone T is the transition zone between Zone 1 and Zone 2. Zone T is recognized by its fibrous dense grain structure.[28]

Zone 2 structures are controlled by adatom diffusion and are not controlled by the chamber pressure. The structures are characterized by columnar grains with highly faceted surfaces. The structures may form platelet or needle shapes.[28]

Zone 3 growth is controlled by bulk diffusion as the deposition temperature is increased and is not affected by the pressure.[26] The grain shape in Zone 3 may be equiaxed or columnar.[28]

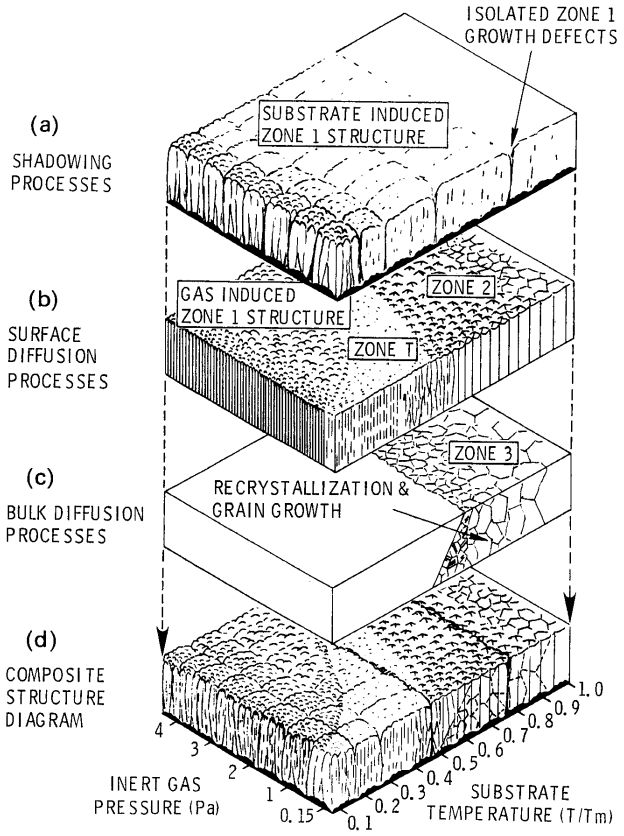

Figure 2.5 Schematic showing the superposition of physical processes that establishes the structural zones.[28]

2.3 Bismuth- Zinc-Niobate

There have been several researchers that have studied the ternary system of Bi_2O_3-ZnO-Nb_2O_5 (BZN).[29-36] There are two main phases in the BZN system, $Bi_{1.5}Zn_{1.0}Nb_{1.5}O_7$ (BZN-1) and $Bi_2Zn_{2/3}Nb_{4/3}O_7$ (BZN-2/3).

2.3.1 Crystallography of Bismuth-Zinc-Niobate

Levin et al. determined the crystal structures of $Bi_2Zn_{2/3}Nb_{4/3}O_7$ and $Bi_{1.5}Zn_{0.92}Nb_{1.5}O_{6.92}$. [37,38] The crystal structures were determined for bulk powder samples

using a combination of electron diffraction, x-ray diffraction, and neutron powder diffraction.

2.3.2 Crystal Structure of $Bi_2Zn_{2/3}Nb_{4/3}O_7$

The crystal structure of $Bi_2Zn_{2/3}Nb_{4/3}O_7$, BZN-2/3, was determined to be a monoclinic zirconolite-like structure with lattice parameters a=13.1037 Å, b=7.6735 Å, c=12.1584 Å, and β=101.318°.[37] Figure 2.6 shows the crystal structure for the BZN-2/3 composition. The top view shows the octahedrally coordinated rings of niobium with the zinc atoms located at the centers of the rings. The side view shows the layers of the octahedrally coordinated niobium that are connected in a similar manner to hexagonal tungsten bronze layers. The side view also shows the layer of bismuth cations between the octahedrally coordinated niobium. The structure refinements show that there are two possible positions for the zinc atom to occupy, which leads to built-in disorder in the crystal structure. Figure 2.7 illustrates the two possible positions for the zinc atoms in the structure.

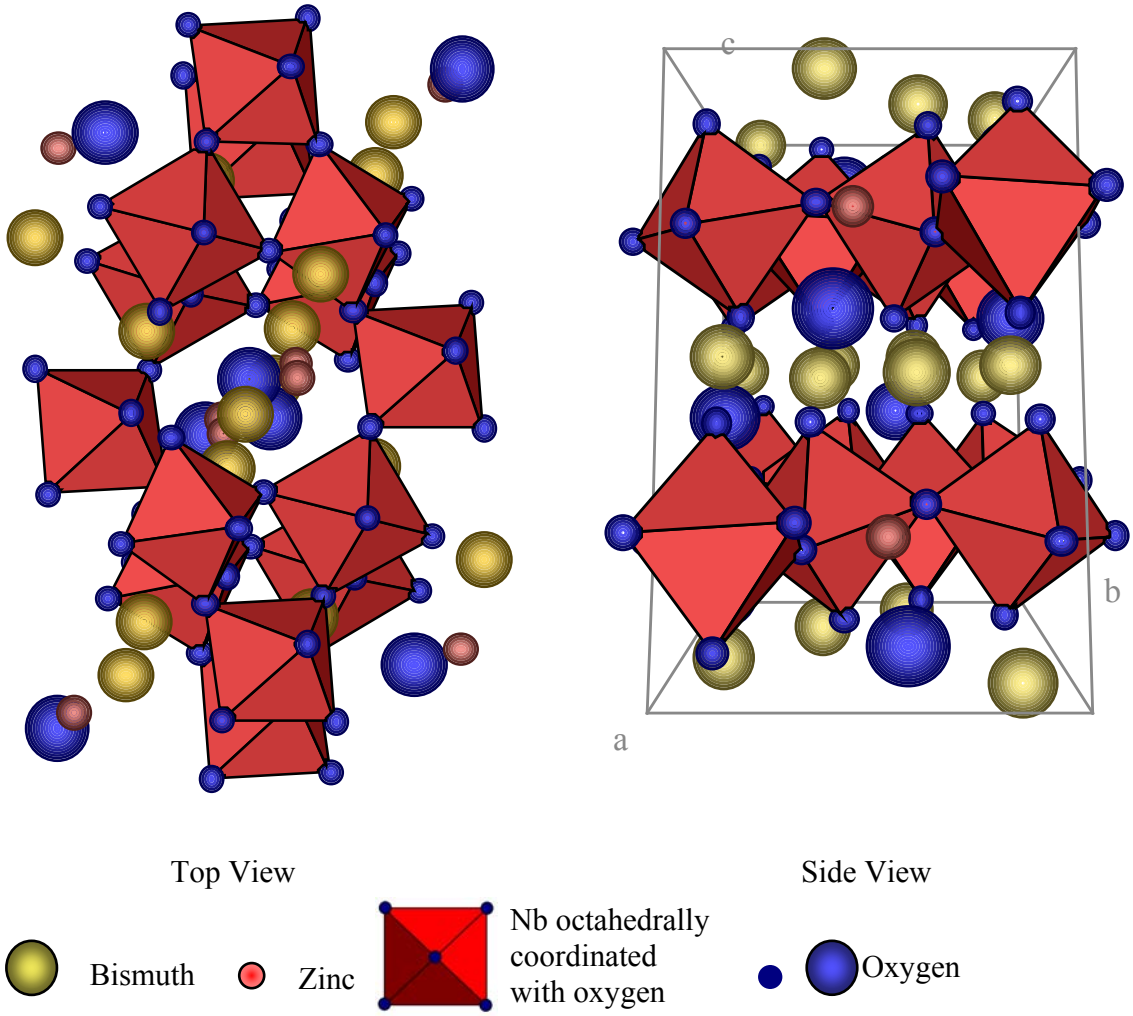

Figure 2.6 Crystal structure for BZN-2/3.

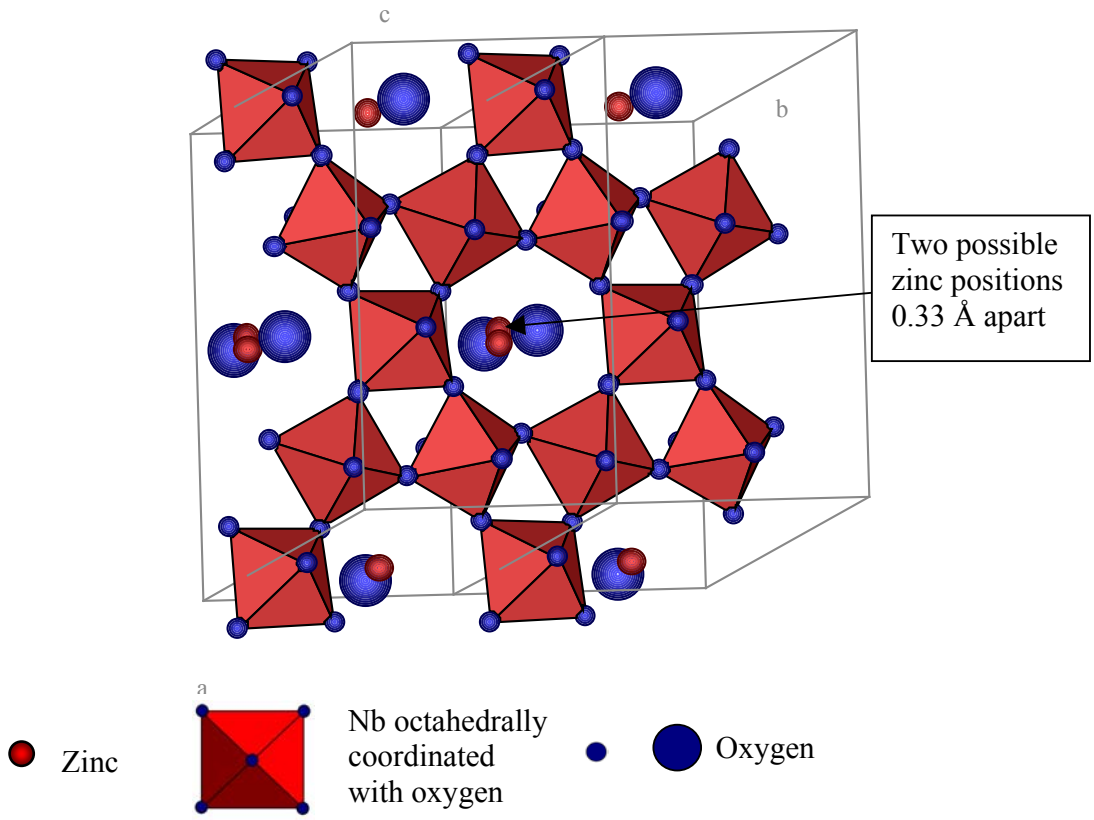

Figure 2.7 Crystal structure of BZN-2/3 illustrating the two possible positions for the zinc atoms.

2.3.3 Crystal Structure of $Bi_{1.5}Zn_{1.0}Nb_{1.5}O_7$

In initial crystallographic studies on $Bi_{1.5}Zn_{1.0}Nb_{1.5}O_7$, BZN-1.0, the samples were found to be mixtures of a cubic pyrochlore phase and small amounts of ZnO.[38] When the Zn content was reduced to $Bi_{1.5}Zn_{0.92}Nb_{1.5}O_{6.92}$, the resulting powders were found to be single phase by x-ray diffraction. Rietvelt refinements completed using neutron powder diffraction data determined that the material has the cubic pyrochlore structure $A_2B_2O_6O'$ with a space group of Fd3m and a lattice parameter of 10.5616 Å.[38] It was determined that both the Bi and the Zn are located on the A sites in the structure. The refinement indicates that the composition should be written as

$Bi_{1.5}Zn_{0.42}(Zn_{0.5}Nb_{1.5})O_{6.92}$. Figure 2.8 shows the crystal structure for the $Bi_{1.5}Zn_{0.92}Nb_{1.5}O_{6.92}$ composition.

The structural analysis determined that the A cations are randomly displaced by ~0.39 Å from the ideal eight-fold coordinated positions. The displacement of the A cations occurs along the six <112> directions which are perpendicular to the O'-A-O' bonds.[38] The O' ions were randomly displaced by ~0.46 Å along all of the twelve <110> directions. The displacements in the O'-A-O' bonds correspond to the lowest frequency bending mode, and probably leads to the high dielectric constant and the low temperature dielectric relaxation that is present in this phase.[38]

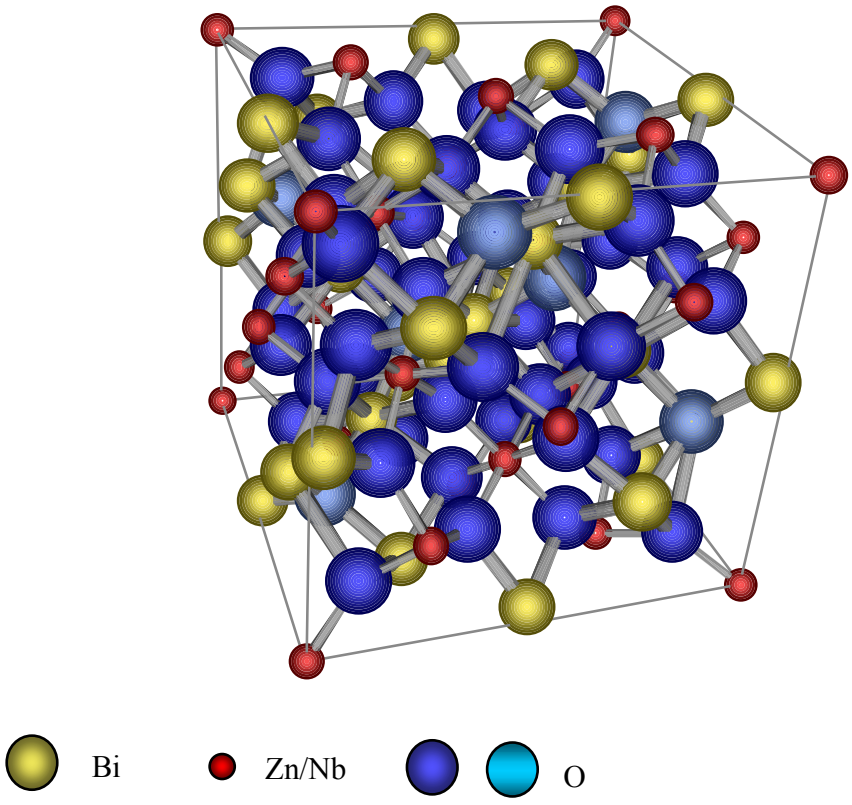

Figure 2.8 Crystal structure for the $Bi_{1.5}Zn_{0.92}Nb_{1.5}O_{6.92}$ composition.

2.4 Bismuth-Zinc-Niobate Bulk Dielectric Properties

Ceramic BZN-1 has a dielectric constant of ~ 150, tan $\delta \leq 0.0004$, and a temperature coefficient of capacitance, TCC, ~ -400 ppm/°C, while BZN-2/3 has a dielectric constant of ~80, tan $\delta \leq 0.0004$ and a TCC of ~ + 150 ppm/°C.[34,36] BZN-1 and BZN-2/3 can be sintered at temperatures below 950 °C, which makes them appealing for devices in low temperature cofired ceramics (LTCC). One of the main applications is for NPO, (negative or positive, but almost zero) temperature coefficient of capacitance, capacitors. Since BZN-1 and BZN-2/3 have different signs and magnitudes to their TCC, it is possible to make a NPO capacitor by mixing appropriate ratios of the two compositions.

BZN-1 shows a relaxation in the dielectric constant as a function of temperature and frequency. Figure 2.9 shows the dielectric constant and loss for BZN-1 for temperatures between 12 and 250 K and frequencies between 2 and 100 kHz. The crystallography of BZN-1 (section 2.3.3) most probably leads to the dielectric relaxation in this composition.[39]

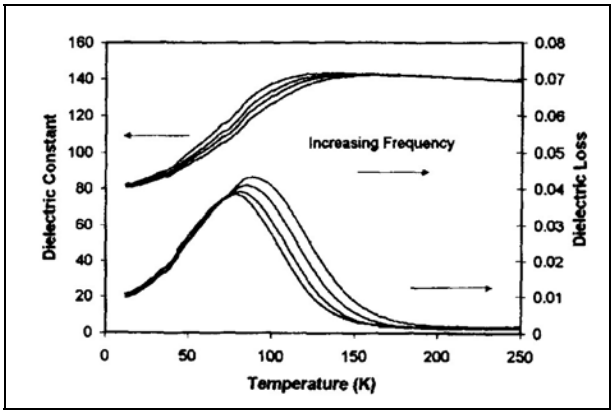

Figure 2.9 Dielectric constant and loss as a function of temperature for 2, 10, 30, and 100 kHz from left to right for BZN-1.[36]

The BZN-2/3 composition shows little to no dielectric relaxation. Figure 2.10 shows the dielectric constant and loss for BZN-2/3 for a temperature range of 12 to 250 K and frequency range between 2 and 100 kHz. At approximately 27 K, the slope of the dielectric constant changes and the dielectric loss begins to increase. The origin of this is not understood at present.

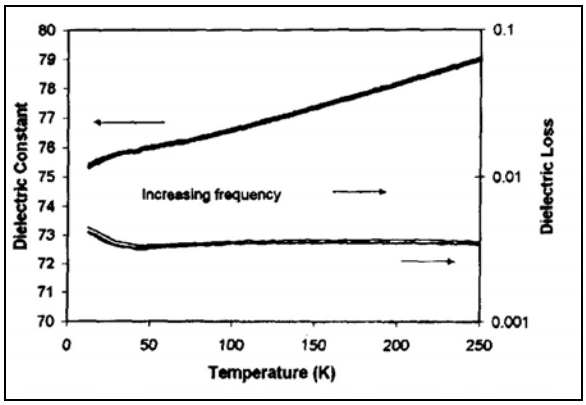

Figure 2.10 Dielectric constant and loss as a function of temperature for 2, 10, 30, and 100 kHz from left to right for BZN-2/3.[36]

2.4 Bismuth-Zinc-Niobate Thin Films

There is currently a small amount of work on bismuth-zinc-niobate thin films. H. Cheng et al. studied films grown from $Bi_2(Zn_{1/3}Nb_{2/3})O_7$ (BZN-2/3) targets by PLD.[7,40,41,42] In these studies, BZN-2/3 was deposited on indium-tin oxide coated glass and MgO [100] substrates. The films were deposited at temperatures between 400 °C and 600 °C. The maximum dielectric constant was measured to be ε_r ~320 at 1 kHz at a deposition temperature of 550 °C.[40] The dielectric loss was not reported. Figure 2.11 shows the dielectric constant as a function of temperature for different deposition temperatures.

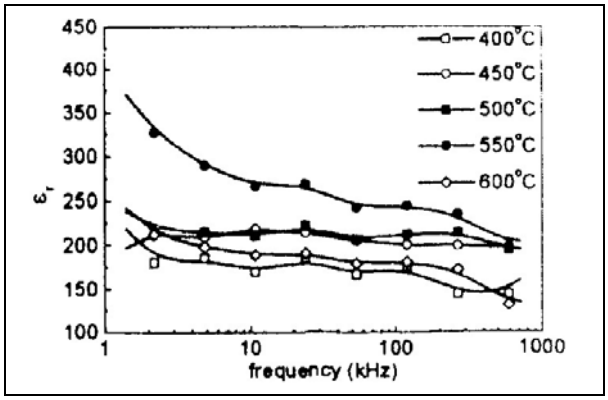

Figure 2.11 Dielectric properties measured from 1 kHz to 1 MHz for BZN-2/3 thin films deposited on MgO substrates at 400-600 °C for 30 minutes.[40]

The reported dielectric constant is much larger than reported values for the bulk composition of BZN-2/3, (~80).[31] One possibility for the large dielectric constant is space charge polarizability, which would be consistent with the decrease in the dielectric constant measured at higher frequencies. In the current work, dielectric properties similar to these were initially measured when platinum electrodes with a poor interface quality were used as the top electrode. Dielectric properties on the Cheng[7] films were also measured using terahertz spectroscopy. The dielectric constant in the THz frequency regime, was $(\varepsilon')_{f \bullet THz}=32$.[41]

Ren et al. and R. Thayer studied $Bi_2(Zn_{1/3}Nb_{2/3})O_7$, BZN-2/3, and $Bi_{1.5}Zn_{1.0}Nb_{1.5}O_7$, BZN-1.0, and $Bi_{1.5}Zn_{0.5}Nb_{1.5}O_{6.5}$, BZN-0.5, films prepared by metal organic deposition.[6,43] Figure 2.12 shows a summary of the dielectric properties as a function of the firing temperature for the three compositions.

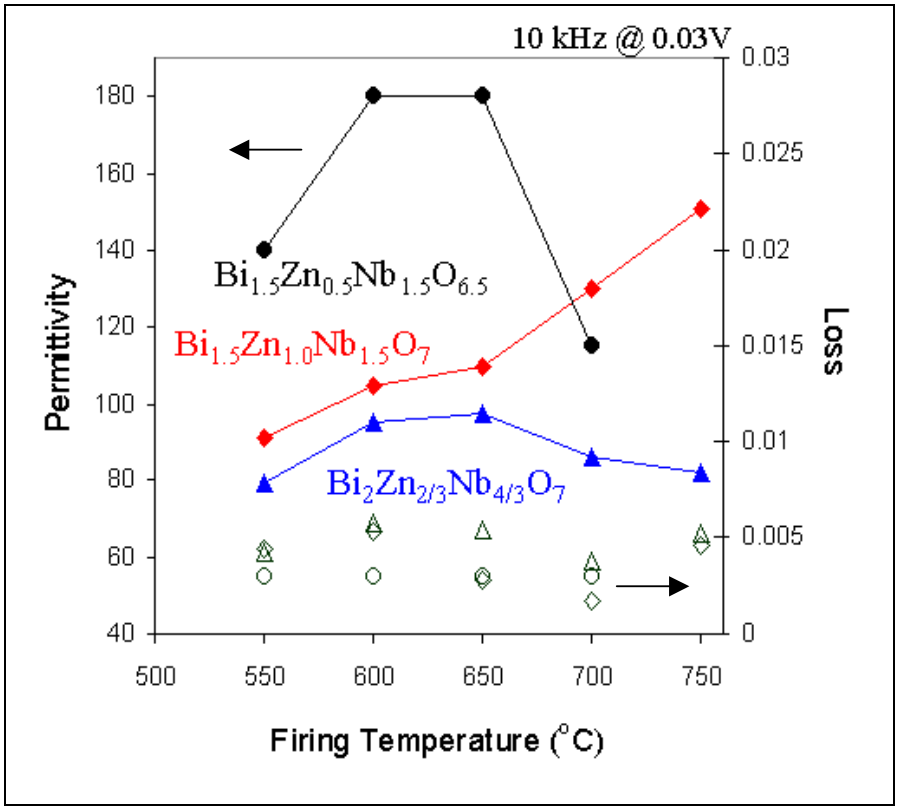

Figure 2.12 Dielectric constant as a function of firing temperature for BZN-1, BZN-0.5, and BZN-2/3 thin films.[6,43]

The maximum dielectric constant was 180 for BZN-0.5 films fired at 600 °C. BZN-1 films had a maximum permittivity of 150, which matched results in bulk BZN-1 samples. Both BZN-1 and BZN-0.5 formed the cubic pyrochlore structure at temperatures greater than 550 °C. BZN-2/3 formed the cubic pyrochlore structure when crystallized between 550 °C to 650 °C and at a firing temperature of 750 °C formed the monoclinic structure.[6] BZN-2/3 with the monoclinic structure at a firing temperature of 750 °C had a permittivity of 80, which was similar to results for bulk BZN-2/3.

Thayer measured the thickness dependence of the capacitance for the BZN-1 composition and found the capacitance to be nearly thickness independent (at least for thicknesses ≥ 500 Å). Figure 2.13 shows the capacitance as a function of film thickness.

Figure 2.13 shows a summary of the temperature coefficient of capacitance, TCC, as a function of firing temperature for the MOD films. BZN-1 and BZN-0.5 films show a negative TCC of –400 ppm/°C and –350 ppm/°C, respectively, for the maximum firing temperature. BZN-2/3 has a positive TCC of 150 ppm/°C.

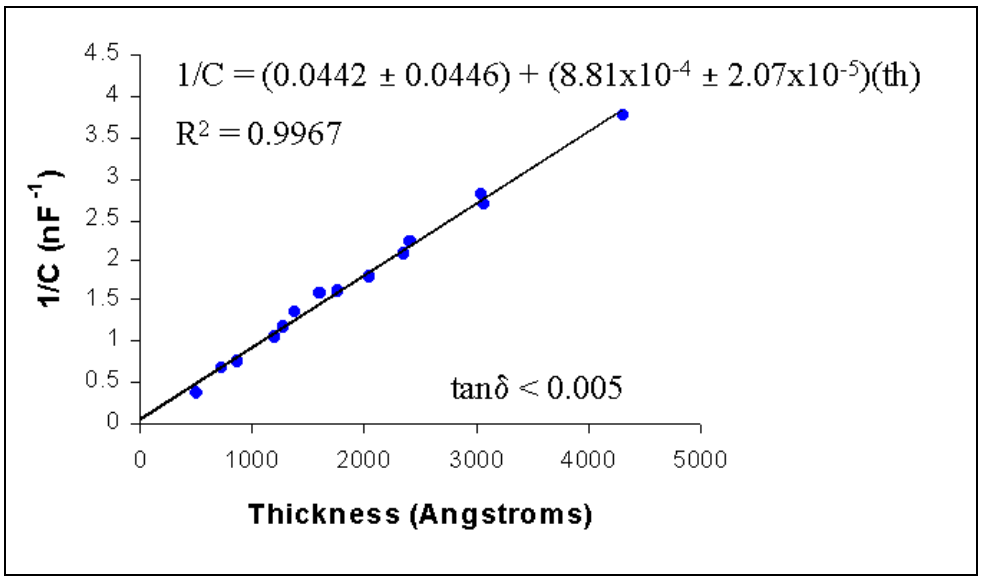

Figure 2.13 Capacitance as a function of thickness for BZN-1 films produced by MOD.[43]

The BZN-1 and BZN-0.5 films produced by MOD showed a low temperature dielectric relaxation (see Figure 2.15) that is similar to the relaxation shown in bulk BZN-1. Figure 2.16 shows the temperature and frequency dependence of the dielectric properties for BZN-2/3 films produced by MOD. Little to no dielectric relaxation was observed.

Ren et al. showed that the BZN-1.0 had a field dependent dielectric constant (tunability) and the dependence increased as the firing temperature and permittivity increased (see Figure 2.17). The dielectric constant changed 10% under a bias of 830 kV/cm and the curve was symmetric with respect to zero bias and had no hysteresis.[6]

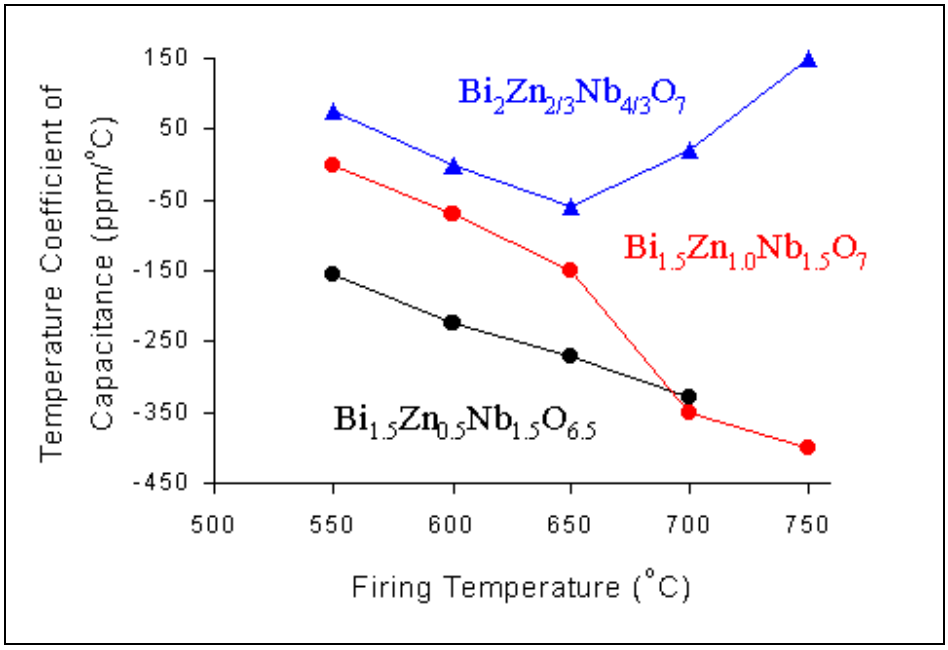

Figure 2.14 Temperature coefficient of capacitance as a function of firing temperature for MOD films.[6,43]

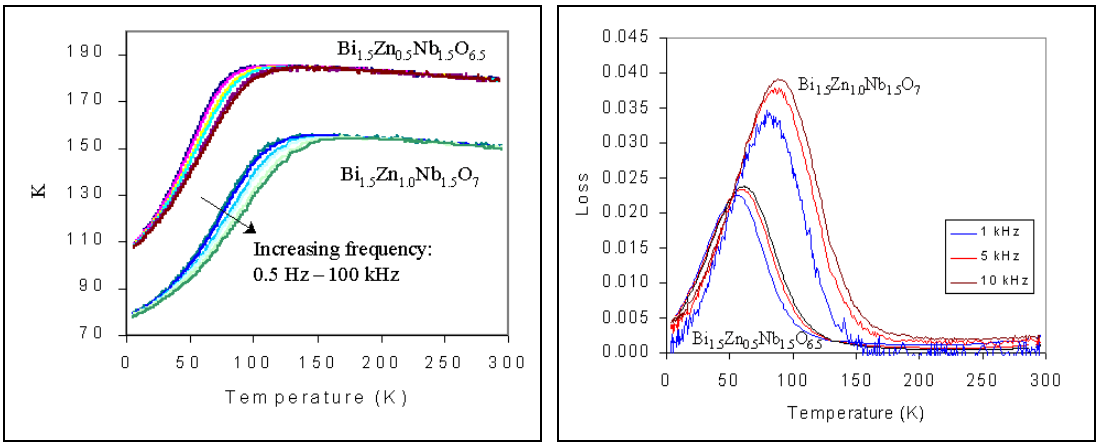

Figure 2.15 Temperature dependence of the dielectric constant and loss for BZN-1 and BZN-0.5 films produced by MOD.[43]

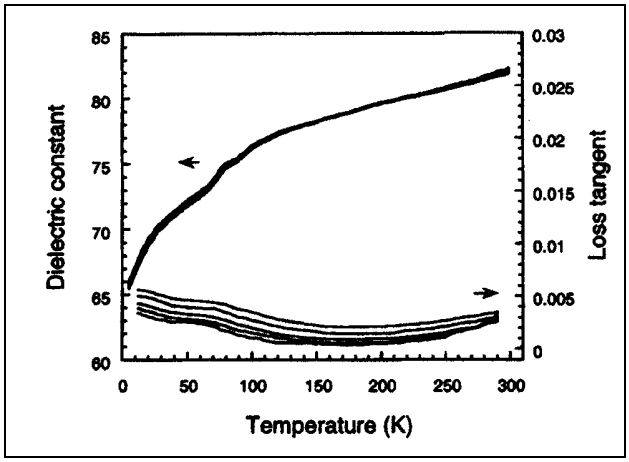

Figure 2.16 Temperature dependence of the dielectric constant for BZN-2/3 measured at 0.5, 1, 2, 5, 10 kHz. For the dielectric constant curve, the top curve was measured at the lowest frequency and for the loss tangent curve the top curve was measured at the highest frequency.[6]

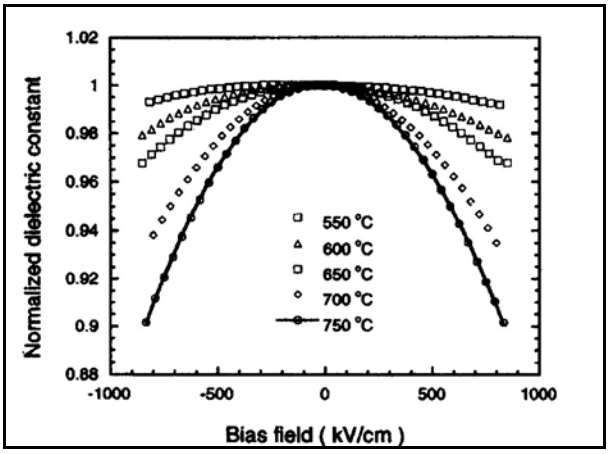

Figure 2.17 Normalized dielectric constant as a function of dc bias field for BZN-1 at different firing temperatures measured at 10 kHz.[6]

Thayer was able to measure the field dependence out to higher fields and at liquid nitrogen temperatures for BZN-1.0 and BZN-0.5. Figure 2.18 and Figure 2.19 show the permittivity as a function of bias field for BZN-1.0 and BZN-0.5, respectively. BZN-1 has 30 % tunability in the permittivity and BZN-0.5 has 26 % tunability in the

permittivity at 1.8 MV/cm.[43] There was no hysteresis in the permittivity as a function of bias field.

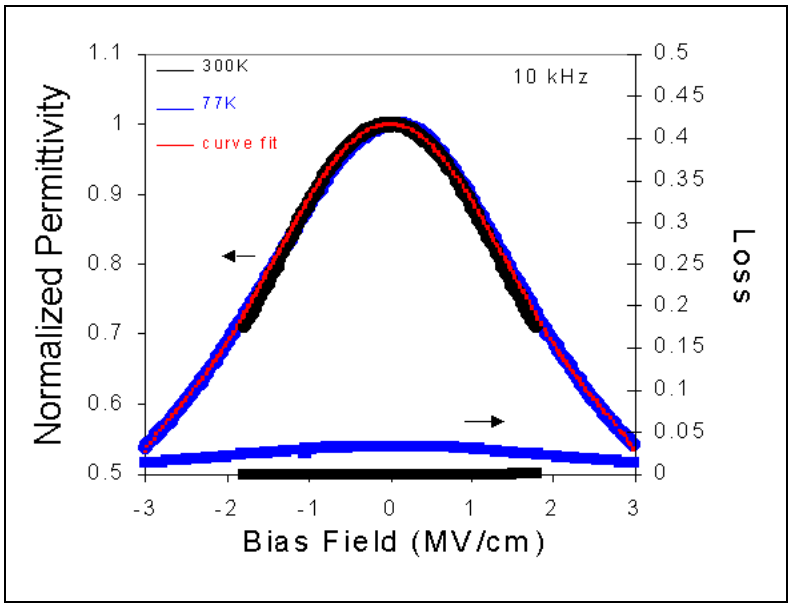

Figure 2.18 Normalized permittivity as a function of bias field measured at different temperatures for a BZN-1 film produced by MOD and fired at 750 °C.[43]

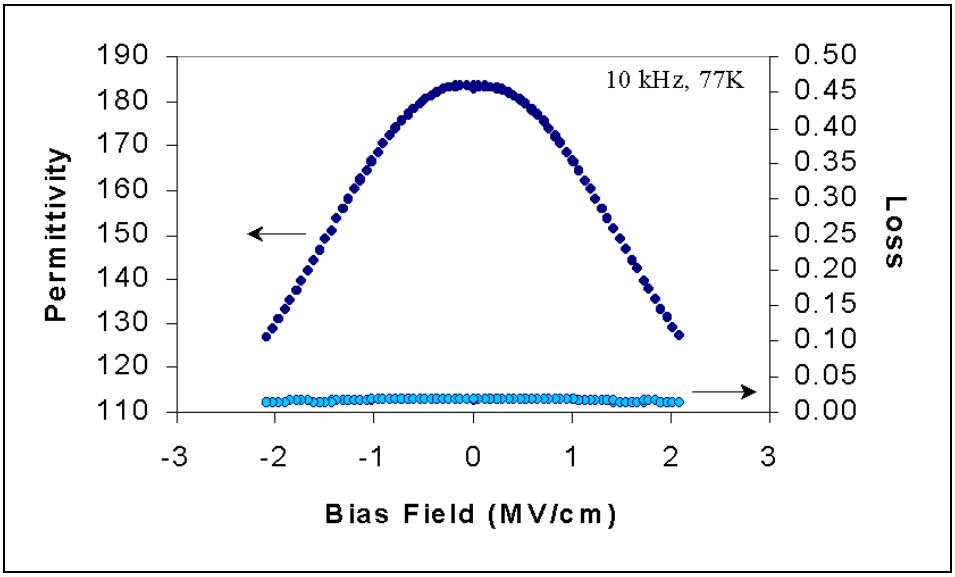

Figure 2.19 Permittivity as a function of bias field at 77 K for BZN-0.5 film produced by MOD at a firing temperature of 650 °C.[43]

2.5 Degradation and Reliability in Ceramic Materials

There are currently no studies completed on the dc degradation and reliability of BZN thin films or bulk samples. This section will review degradation mechanisms observed in ceramic materials and discuss a method for determining the reliability of a material using highly accelerated lifetime testing (HALT).

Degradation in dielectric ceramics denotes a long-term decrease in the high insulation resistance of the material under dc voltages.[44] Degradation may occur at dc fields far below the dielectric strength of the material and is typically the limiting factor for the lifetime of the capacitor.[45] The degradation of a material is affected by the grain size, doping, stoichiometry, secondary phases, porosity, and the electrode properties.[46] There are two main categories of models that have been used to describe the degradation: the grain boundary model and the reduction model.

The grain boundary model relates dc-field induced deterioration of the grain boundaries to the degradation of the material. It is known that the grain boundaries in dielectric ceramics often exhibit higher specific resistivities than the bulk of the grains. The concentration of high electrical fields in the grain boundaries leads to local dielectric breakdown at the grain boundaries.[45]

The reduction model on the other hand, assumes that the relatively high mobility of oxygen vacancies causes the electromigration of the oxygen vacancies towards the cathode of the capacitor. The oxygen vacancies pile up at the cathode and are compensated by electrons injected at the cathode. The ceramic material then undergoes a reduction, which leads to an increase in the electronic conductivity of the material.[45]

Highly accelerated lifetime testing, HALT, can be used to determine the reliability of ceramic capacitors. The following empirical relationship can be used to determine the time to failure at any voltage and temperature:

$$\frac{t_1}{t_2} = \left(\frac{V_2}{V_1}\right)^n \exp\left[\frac{E_a}{k}\left(\frac{1}{T_1} - \frac{1}{T_2}\right)\right] \qquad (2.\ 1)$$

where t_1 is the mean time to failure at V_1 and T_1, t_2 is the mean time to failure at V_2 and T_2, V_1 and V_2 are the test voltages, n is the voltage acceleration factor, E_a is the activation energy, k is Boltzmann's constant, and T_1 and T_2 are the test temperatures in K.[47] Researchers have reported a variety of different values for the voltage acceleration factor and activation energy. Table 2.1 shows a comparison of different HALT and the variation in n and E_a for multilayer ceramic capacitors. The values typically used in industry are n=3 and E_a= 1.1 eV.[48]

Table 2.1 Comparison of results of HALT for different studies on multilayer capacitors.

Dielectric Material	n	E_a (eV)	Reference
$BaTiO_3$-X7R, Z5U	3.0	1.0	Munikoti (47)
$BaTiO_3$-X7R	5.4-7.1	1.21	Maher (48)
$BaTiO_3$-X7R	6.5	1.3-1.4	Mann ([49])

Chapter 3 Experimental Procedure

3.1 Description of Deposition Equipment

Bismuth-zinc-niobate thin film samples were produced by pulsed laser deposition (PLD) using a high vacuum chamber that was designed by Maffei.[50]

3.1.1 Excimer Laser

The laser used was a Lambda Physik Compex 102, which was operated using a krypton fluorine gas mixture to produce radiation at 248 nm. The laser pulses were 30 ns in duration. The pulse frequency was typically varied between 1 and 10 Hz. All of the depositions were made using the laser in the constant energy mode at 250 mJ.

3.1.2 Laser Optics

Figure 3.1 shows the chamber schematic. The laser was focused onto the target using a plano-convex fused silica lens with a focal length of 0.5 m.[51] The laser spot size was varied by changing the position of the lens, and thus the energy density could be varied. The energy density was varied between 1.5 and 2.5 J/cm^2. Typically, an energy density of 2.5 J/cm^2 was used. The focused beam was introduced into the chamber through a fused silica window. The window was rotated before every deposition to reduce the optical damage to the window. The window was typically cleaned after 20 to 30 depositions with deionized water and an optics cleaner EMG (Lambda Physik, Germany).

3.1.3 Targets

The laser was focused onto ceramic targets that were 1.5” in diameter. Targets were mounted on stainless steel holders using silver conductive paint (Alfa Aesar, Ward Hill, MA), and the organic vehicle was burned out by heating the bonded holder and the target on a hot plate at 125 °C for 3 to 4 hours. The targets were then heated in an oven for 2 hours at 150 °C to insure the target was bonded well to the mounts. Targets were resurfaced after every deposition using 240 grit sandpaper.

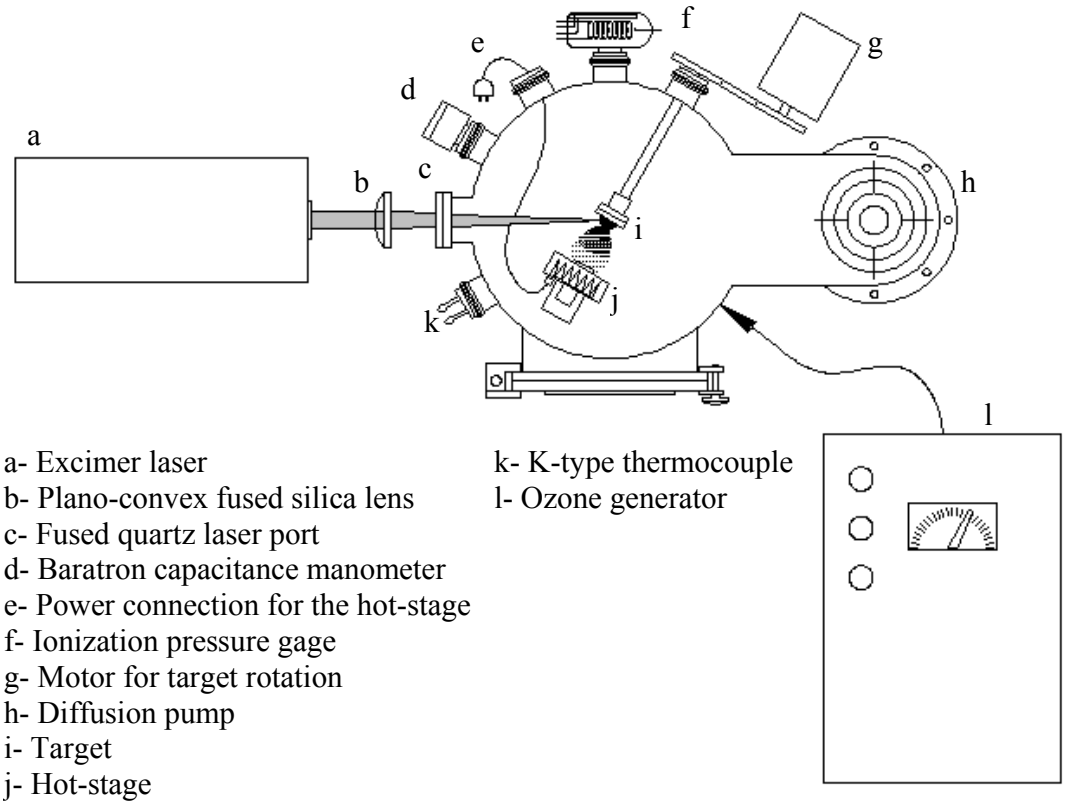

a- Excimer laser
b- Plano-convex fused silica lens
c- Fused quartz laser port
d- Baratron capacitance manometer
e- Power connection for the hot-stage
f- Ionization pressure gage
g- Motor for target rotation
h- Diffusion pump
i- Target
j- Hot-stage
k- K-type thermocouple
l- Ozone generator

Figure 3.1 PLD chamber schematic.[52]

3.1.4 Substrate Mounting

Substrates were mounted onto the hot stage using silver conductive paint (Alfa Aesar, Ward Hill, MA). The entire sample holder assembly was then placed in the chamber so that the center of the substrate would be in line with the center of the plume. Figure 3.2 shows a schematic of the substrate heater. The hot stage was a block style heater wound with Thermocoax heating element (Thermocoax Inc., Alpharetta, GA). Thermocoax consists of a Kanthal resistive heating element surrounded by a high purity MgO powder swaged into an inconel jacket.[51] The hot stage was powered by a Hewlett Packard type 6268B dc supply. A type-K thermocouple was positioned in the stainless steel mounting block to measure the temperature. The samples were heated to 100 °C in the chamber. The chamber was then pumped down. The hot stage was typically operated between 400 and 650 °C.

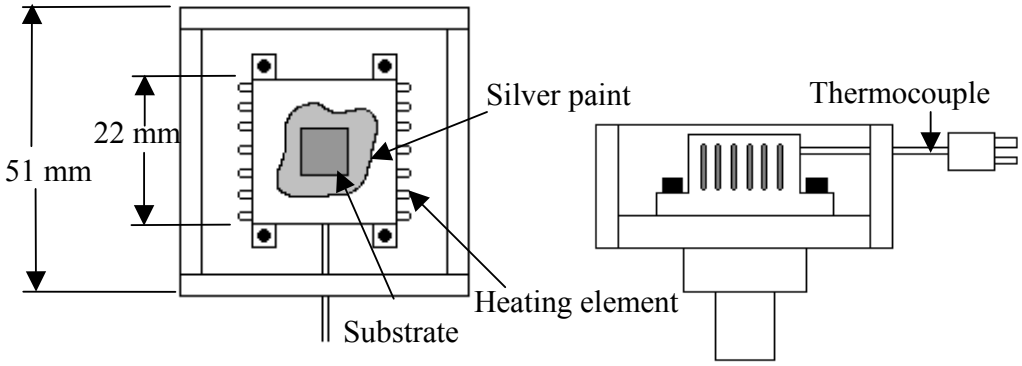

Figure 3.2 Substrate heater.[52]

3.1.5 Vacuum System

The chamber was pumped down from atmosphere to 30 mTorr using an Alcatel model 2033CP rotary pump. The valve to the rotary pump was then closed and the

backing valve and the gate valve on the diffusion pump were opened. The chamber was then pumped down to lower pressures, typically ~10^{-6} torr, using a Varian model M6 diffusion pump running with Fomblin 25/6 oil.

For all depositions, a mixture of 10 % ozone and 90 % oxygen was used as the ambient gas. The ozone was supplied by a PCI-G1 ozone generator. The gas flow into the chamber was introduced using mass flow controllers from MKS instruments. The mixture of ozone and oxygen was introduced at 100 sccm. The chamber pressure was controlled manually by closing the gate value to the diffusion pump. Pressures between 50 and 400 mTorr were achieved for depositions. The gate valve was closed after the depositions.

After deposition, the samples were cooled in the chamber under vacuum. The samples were cooled at approximately 10 °C/min. The samples were removed from the chamber once the temperature was below 100 °C.

3.2 Substrates

A majority of the films were grown on Pt/Ti/SiO_2/(100) Si wafers (Nova Electronic Materials, Inc., Richardson, TX). The wafers had a 1 μm thermal oxide, 200 Å titanium buffer layer, and 1,500 Å platinum layer. The Nova wafers were 4" diameter wafers. Some films were grown on platinum electrodes produced using an ultra high vacuum molecular beam epitaxy, UHV MBE, vacuum chamber (courtesy of J. P. Maria, NCSU). These wafers were Pt/ La, Pt alloy (5 vol % La in Pt)/ La_2O_3/SiO_2/Si. These wafers had 200 Å Pt, 800 Å Pt/ La alloy (5 vol % La in Pt), 50 Å La_2O_3, and 270 Å thermal oxide of SiO_2. All wafers were cut using a diamond scribe into approximately 1 cm x 1 cm pieces and blown off with N_2 gas before mounting onto the heater.

1 cm^2 (100) MgO single crystal substrates (Commercial Crystal Laboratories, Naples, FL) were used as the substrates for Rutherford Backscattering analysis, RBS. MgO substrates were used because the MgO signals did not interfere with the cation signals from the film. Prior to growth, the MgO substrates were dipped in acetone followed by a dip in isopropanol and then dried using N_2 gas.

3.3 BZN Target Fabrication

The targets were fabricated using a standard mixed oxide fabrication route. The starting materials were reagent-grade oxide powders of Bi_2O_3 and Nb_2O_5 (Aldrich Chemical Company ltd, Sheboygan, WI) and ZnO (J.T. Baker Chem. Co. Phillipsburg, NJ). The $Bi_{1.5}Zn_{0.5}Nb_{1.5}O_{6.5}$, BZN-0.5, target was batched using a stoichiometric mixture of powders. A 60 % vol solid slurry was prepared by adding deionized water and 1 vol % (10 % dispersant solution of Tamol 963 (Rohm and Haas, Philadelphia, PA) and was milled for 24 hours using zirconia media. The powder was then dried at 120 °C for 24 hours, and sieved through an 80 mesh screen. The powder was then calcined at 850°C for 4 hours in a closed alumina crucible to minimize any volatilization of the compounds. The BZN-0.5 target was mixed phase of $BiNbO_4$ and cubic pyrochlore. Figure 3.3 shows the XRD of the BZN-0.5 target.

The $Bi_{1.5}Zn_{1.0}Nb_{1.5}O_7$, BZN-1, target and $Bi_2Zn_{2/3}Nb_{4/3}O_7$, BZN-2/3, targets were prepared using a columbite precursor method.[53] The columbite was batched the same way the BZN-0.5 was batched. An initial calcination step between ZnO and Nb_2O_5 was completed at 1000 °C for 4 hours to form $ZnNb_2O_6$. Columbite formation was confirmed through x-ray diffractometry. Stoichiometric mixtures of columbite and Bi_2O_3 were

batched for the BZN-1 and BZN-2/3 compositions and milled. They were then sieved and calcined at 800 °C for 4 hours in air in a covered crucible.

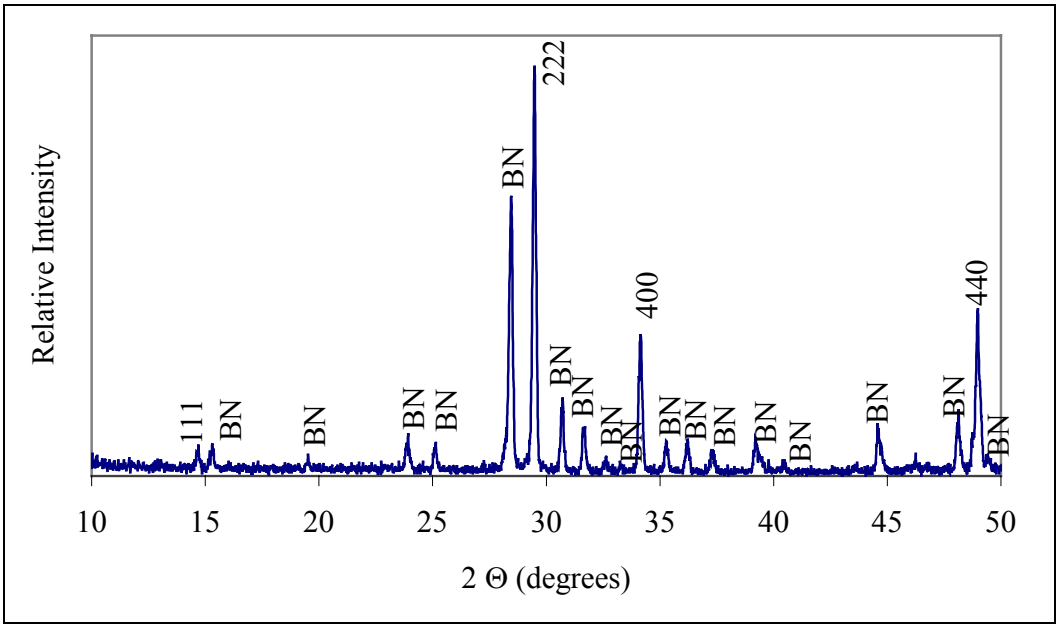

Figure 3.3 X-ray diffraction pattern for the BZN-0.5 target. Indexed peaks are from the cubic pyrochlore phase. BN stands for $BiNbO_4$ (PDF: 16-0295).

The calcined powders were milled in deionized water and dispersant using zirconia media for 24 hours. The powders were dried at 120 °C for 24 hours. Approximately 5 wt % acryloid binder was added and the powder was sieved. The targets were uniaxially pressed at approximately 82 MPa in a 1.75" diameter mold. The targets were placed on zirconia setters and covered with an alumina crucible. The targets were heated from room temperature to 600 °C at 3 °C/min and held at 600 °C for 4 hours for binder burnout. Then the targets were heated at 3 °C/min to 1000 °C and held at 1000°C for 4 hours. The furnace was then allowed to cool back to room temperature. The resulting targets were >95% of the theoretical density. Both the BZN-1 and BZN-2/3 targets were phase pure within the resolution of the XRD equipment. Figure 3.4 and

Figure 3.5 shows the XRD pattern for the BZN-1 and BZN-2/3 compositions, respectively.

Targets with excess Bi_2O_3 were also batched. The excess Bi_2O_3 was added prior to the last milling step. The amount of excess Bi_2O_3 added to the target was determined from the RBS analysis of the thin films. Table 3.1 shows a summary of the compositions of targets batched for this study.

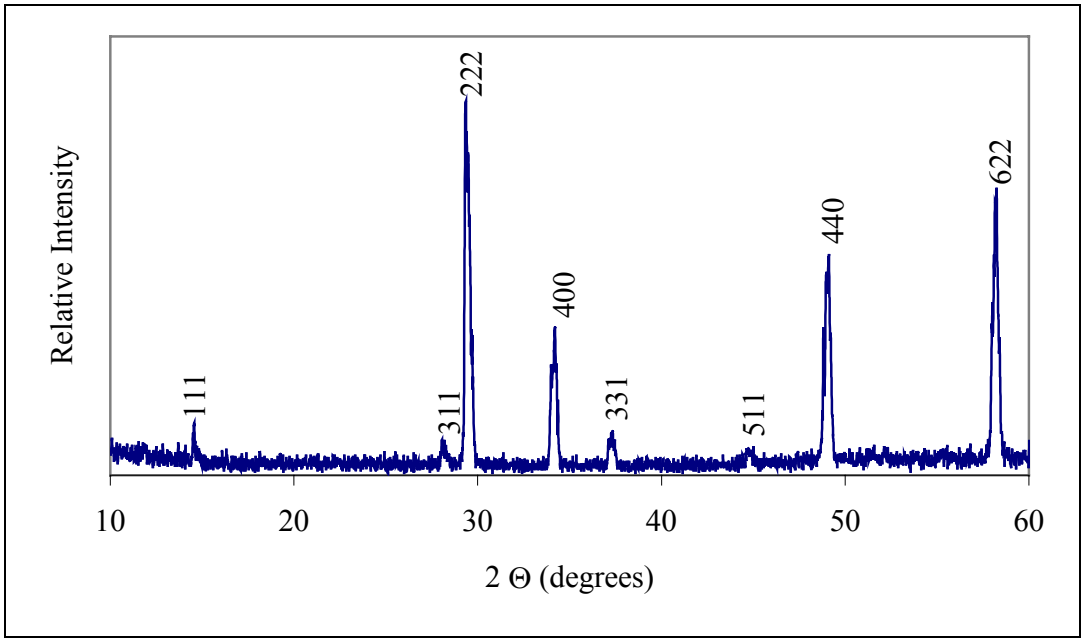

Figure 3.4 X-ray diffraction pattern for the BZN-1 target. Indexed peaks are from the cubic pyrochlore phase.

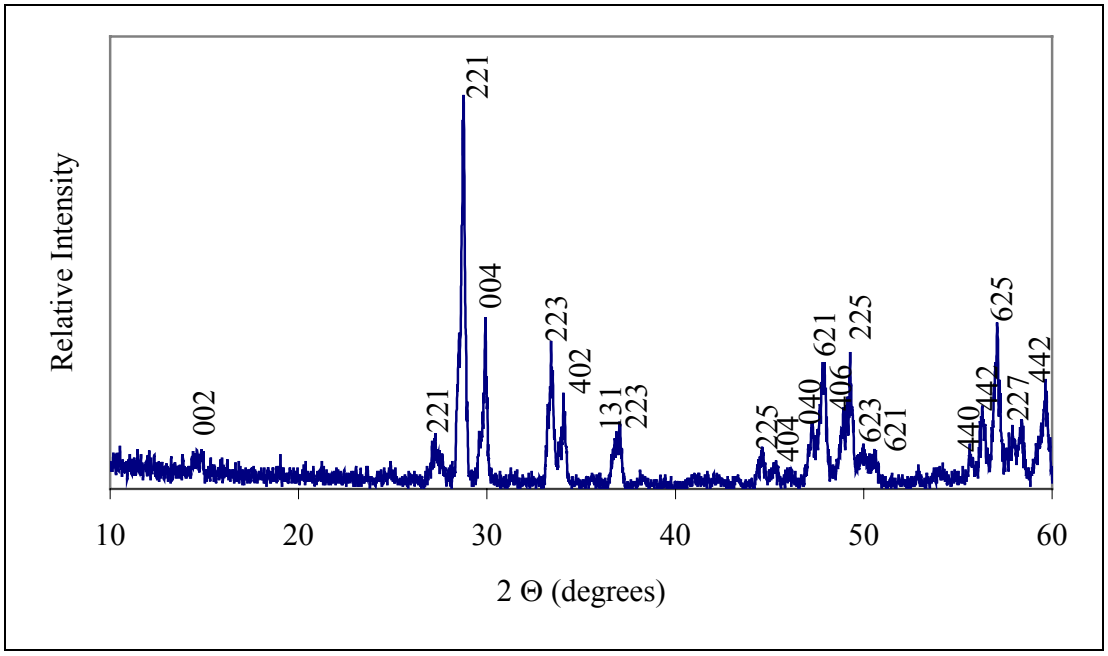

Figure 3.5 X-ray diffraction pattern of the BZN-2/3 target. Indexed peaks are from the monoclinic phase.[37]

Table 3.1 Summary of the target compositions batched for this study.

Target Composition	Reference Name
$Bi_{1.5}Zn_{1.0}Nb_{1.5}O_7$	BZN-1
$Bi_{1.5}Zn_{1.0}Nb_{1.5}O_7$ + 0.11 mol Bi_2O_3	BZN-1 + 0.11 mol Bi_2O_3
$Bi_{1.5}Zn_{1.0}Nb_{1.5}O_7$ + 0.15 mol Bi_2O_3	BZN-1 + 0.15 mol Bi_2O_3
$Bi_{1.5}Zn_{0.5}Nb_{1.5}O_{6.5}$	BZN-0.5
$Bi_{1.5}Zn_{0.5}Nb_{1.5}O_{6.5}$ + 0.03 mol Bi_2O_3	BZN-0.5 + 0.03 mol Bi_2O_3
$Bi_{1.5}Zn_{0.5}Nb_{1.5}O_{6.5}$ + 0.15 mol Bi_2O_3	BZN-0.5 + 0.15 mol Bi_2O_3
$Bi_2Zn_{2/3}Nb_{4/3}O_7$	BZN-2/3

3.3 Deposition of BZN

All of the BZN films were deposited using the on-axis ablation geometry. Specific processing parameters such as target to substrate distance, pressure, and temperature will be discussed in the results and discussion chapter. The target to substrate distance was varied between 4 and 7 cm. The chamber pressure was varied

from vacuum (10^{-6}) to 400 mTorr. The deposition temperature was varied between 400 and 650 °C.

For most of the depositions on Nova substrates, a thin film ~75 Å was grown at 250 °C, at a target to substrate distance of 7 cm, a laser frequency of 10 Hz, and chamber pressure of 200 mTorr. The precoating of the wafers was completed to prevent the platinum from hillocking. Figure 3.6 shows the Nova substrate heated to 650 °C for five minutes. The bright spots are the platinum hillocking on the surface of the substrate. These types of defects were observed in previous studies.[54] Figure 3.7 shows an SEM image of a film deposited at a substrate temperature of 250 °C and then heated to 650 °C for 30 minutes; there are no visible defects on the surface of the film showing that the thin film prevented the hillocking.

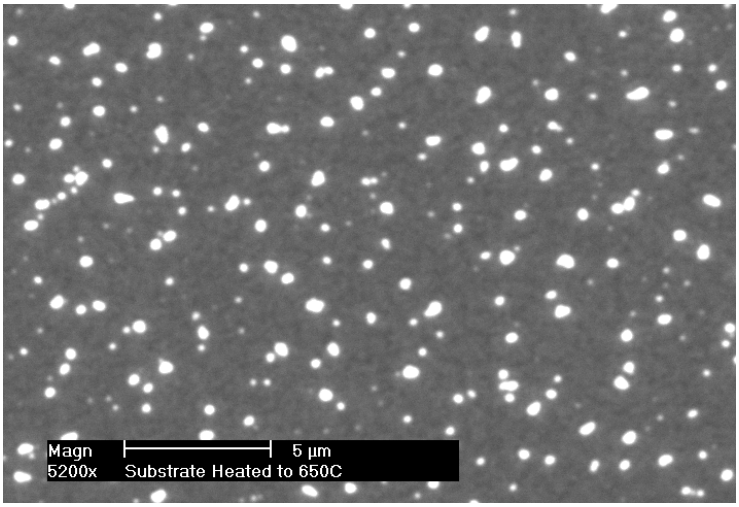

Figure 3.6 Nova substrate heated to 650 °C for 5 minutes in vacuum.

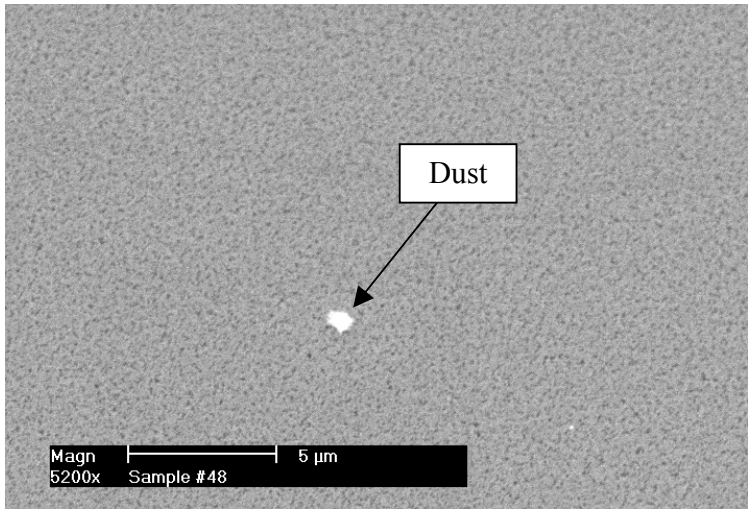

Figure 3.7 Nova substrate with BZN film deposited at a substrate temperature of 250 °C, at a target to substrate distance of 7 cm, a laser frequency of 3 Hz, a chamber pressure of 200 mTorr, and a deposition time of 15 seconds. The film was then heated to 650 °C and held at 650 °C for 30 minutes.

In order to measure the film thickness, a small portion of the film was etched using 30 vol % HF and 70 vol % deionized water to expose the bottom platinum electrode. The thickness of the films was measured using an Alpha-step 2000 surface profilometer (Tencor Instruments, Mountain View, CA) and scanned over 500 μm distances on the film. The typical film thickness was between 200 and 400 nm.

3.4 Top Electrode Deposition and Fabrication

The top electrodes were typically 100 Å chromium/ 1500 Å gold deposited by evaporation or sputtering. The Cr/Au was deposited on the entire film and then patterned by photolithography. No variations in the electrical properties were observed between top electrodes that were deposited by evaporation versus sputtering. Sputtering of Cr/Au was the primary deposition method used for the top electrodes. A CMS-18 thin film deposition system (Kurt J. Lesker Company, Pittsburgh, PA) was the sputtering system used. The chamber was pumped down to $< 10^{-8}$ torr before deposition. The chromium

was sputtered using an RF magnetron sputter gun at 200 W. The gold was sputtered using a DC magnetron sputter gun at 200 W. Both chromium and gold targets were presputtered for 2 minutes at an argon pressure of 30 mTorr, before the shutter was opened. This was done to insure that oxides that might have formed on the targets were sputtered off of the targets before the shutter was opened to the samples. The metals were deposited in an argon ambient at a chamber pressure of 5 mTorr. The samples were then moved from the deposition chamber into a loadlock that was located in a Class 100 cleanroom.

The patterning procedure for the top electrodes was completed using the following steps. 1) The samples were placed onto a hotplate at 160 °C for 5 minutes to remove any water on the samples. 2) The samples were blown off with N_2 and placed onto a spinner. 3) Two to three drops of hexamethyldisilazane, HMDS, (Sigma Aldrich, Milwaukee, WI) were spun on the samples at 4000 rpm for 40 seconds as an adhesion promoter for the photoresist. 4) Shipley 1811 photoresist (Shipley, Newton, MA) was dispensed onto the sample until the sample was completely covered and was then spun at 4000 rpm for 40 seconds. The edges of the samples were wiped with a Q-tip with acetone to remove any photoresist. The samples were softbaked at 100 °C for 1 minute. 5) The samples were exposed using a Karl Suss MJB 3 aligner (Waterbury Center, VT) at 3 W/cm^2. The lamp produced radiation between 280 and 450 nm. 6) The photoresist was developed using Microposit 351 (Shipley, Newton, MA) at a ratio of 1:5 developer: water for 45 seconds. The samples were hardbaked at 115 °C for 10 minutes. 7) The samples were etched in Type TFA gold etch, (Transene Company Inc., Danvers, MA) for 1 minute and rinsed with water. 8) The Cr was then removed in Type 1020 chromium

etch (Transene Company Inc., Danvers, MA) for 30 seconds. 9) The samples were soaked in acetone for 20 minutes to remove the photoresist and then rinsed in isopropanol.

The electrodes patterned typically were 100 μm x 100 μm to 400 μm x 400 μm. The electrode area was measured using the SEM. The electrode area was very consistent between batches. It was found that electrodes prepared in this way resulted in low loss tangents for the capacitors. A study was completed to see if annealing the Cr/Au electrodes would improve the dielectric properties, but the properties degraded after annealing at 400 °C for 30 minutes probably due to the formation of Cr_2O_3 at the interface.

For a few samples, 1500 Å platinum electrodes were deposited by sputtering using another sputtering tool Balzers Model SCD 050 (Technotrade, Manchester, NH) at a current of 63 mA and 0.05 mbar argon. These electrodes were deposited through a shadow mask and did not need to be patterned. These electrodes needed to be annealed at 650 °C for 1-2 minutes either to remove impurities in the electrodes or to improve the dielectric electrode interface.

3.5 X-ray Analysis

The crystallinity of the BZN thin films was characterized with a Scintag DMC-105 X-ray diffractometer (Scintag, Inc., Sunnyvale, CA) using Cu K_α radiation. The samples were mounted using double sided tape to a plexi-glass holder that was machined to the thickness of the wafer. The samples were scanned at 2 °/min between 2-theta angles of 10 to 70°.

3.6 Electrical Property Analysis

The dielectric properties of the BZN thin films were measured using a Hewlett Packard 4284A multi-frequency LCR meter using probes. The samples were packaged into 24 pin ceramic packages (Spectrum Semiconductor Materials, Inc., San Jose, CA) to complete the electrical property measurements at temperatures and for HALT analysis. Figure 3.8 shows the chip package used in these tests. The 1st pin was the ground contact for HALT analysis. The remaining 23 pins were used for HALT measurements. The 1st and 6st pins on each side were the ground contacts for the other measurements at temperature.

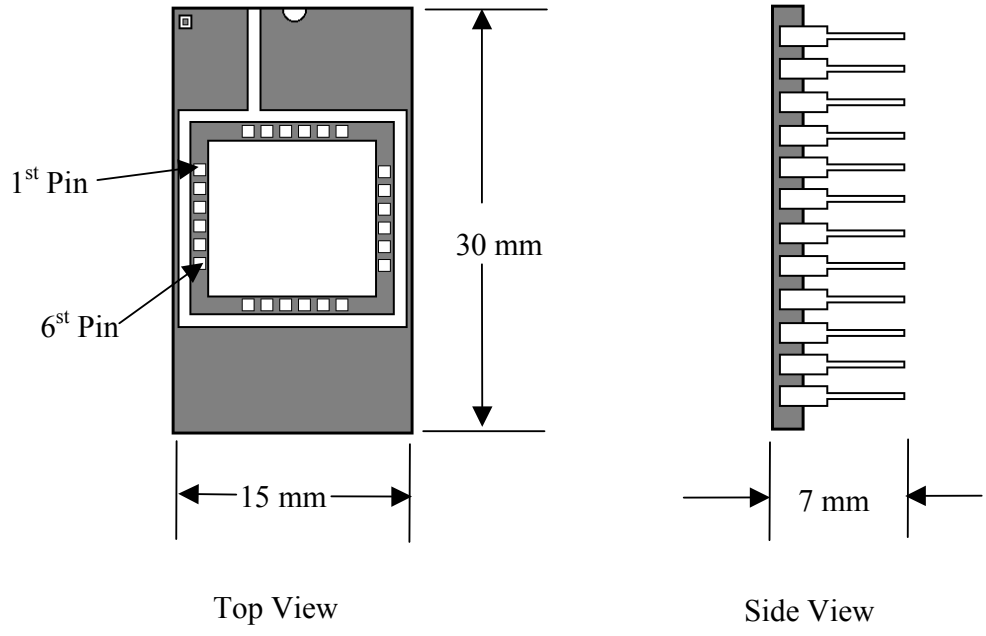

Figure 3.8 Schematic of the chip package.

The electrical contacts to the samples were completed by wirebonding from the package to the sample's electrodes. Wirebonding was completed using the Model 4123

Wedge Bonder (Kulicke & Soffa Industries, Inc., Horsham, PA) with 1 mil aluminum wire.

For temperatures between 140 and –160 °C, a computer controlled Delta 9023 temperature oven (Delta Design, Inc., San Diego, CA) with a cooling ramp rate of 5 °C/min was used. The measurement frequencies were typically between 500 Hz and 1 MHz.

Another measurement setup was used to measure the dielectric properties from room temperature to 4 K. The sample was mounted using a conductive epoxy onto sapphire single crystal substrates with 4 gold pads on the sapphire. Wirebonds were made from the sample's electrodes to the gold pads on the sapphire. Gold wires were then attached to the sapphire substrate using silver paint. The gold wires were then connected to 4-point probe contacts on the end of a rod. The sample was then slowly lowered into liquid helium at approximately 2 °C/min. The electrical properties were measured using a Keithley 3330 LCZ meter (Cleveland, OH), which was run using Labview (National Instruments, Austin, TX).

3.7 HALT Measurements

Highly accelerated lifetime tests (HALT) were performed using Labview (National Instruments, Austin, TX) based software to monitor the current across the BZN thin film capacitor as a function of time. The setup monitored 23 electrodes simultaneously. HALT measurements were conducted at temperatures from 85-150 °C with dc fields of 250-400 kV/cm.

3.8 Composition Characterization

Rutherford backscattering spectroscopy, RBS, was performed on some of the films at Argonne National Laboratory by Dr. Peter Baldo. The probe size was 1 mm^2 and was focused onto the center of the sample. The films for compositional analysis were grown on 1 cm^2 MgO single crystals and had a thickness between 400 and 600 Å. The composition of the oxygen in the films was not determined using RBS because RBS analysis can be inaccurate for light elements. The amount of oxygen was calculated using the standard oxidation states of the bismuth, zinc, and niobium, assuming ionic compensation of defects. The composition was normalized to the niobium composition.

3.9 Morphology Characterization

The film microstructure was investigated using a scanning electron microscope, SEM, Hitachi S-3001. The samples were not coated for SEM analysis. An atomic force microscope, Digital Instruments Dimension 3100, Santa Barbara, CA was used in tapping mode to investigate the surface morphology and the surface roughness of the films.

Chapter 4 Results and Discussion

This chapter is subdivided into three main sections. The first section looks at the effects of target to substrate distance, deposition pressure, and laser frequency on the growth of BZN thin films by PLD. Particular emphasis is placed on the factors that influence the crystallization temperature and the film composition. In the second section, the dielectric properties are reported as a function of the processing conditions. The third section discusses the reliability of the BZN capacitors.

4.1 Deposition Study

In pulsed laser deposition, many of the deposition parameters are correlated (i.e. a change in chamber pressure also affects the growth rate and the amount of bombardment experienced by the growing film). Thus, a number of parametric studies of the deposition parameters were made, recognizing that there is some overlap in the effects of the controllable parameters.

4.1.1 Target to Substrate Distance

The deposition rate of films grown by PLD changes dramatically as a function of distance from the target. Figure 4.1 shows the deposition rate as a function of target to substrate distance, using the $Bi_2Zn_{2/3}Nb_{4/3}O_7$ target, at a laser frequency of 10 Hz, and a chamber pressure of 200 mTorr. All seven of the targets showed approximately the same deposition rate as a function of target to substrate distance.

The deposition rate was determined from the thickest portion of the film. The deposition rate decreased as the substrate was moved further away from the target and consequently from the plasma plume. Figure 4.2 shows the plasma plume as function of

target to substrate distance for a chamber pressure of 100 mTorr. The substrate is located just outside of the plume at distances greater than 6 cm. The change in deposition rate as a function of target to substrate distance is similar to PLD work completed using $PbZr_xTi_{1-x}O_3$ (PZT) targets, where the deposition rate changed from 22 Å/s to 4 Å/s at target to substrate distances of 3 cm and 7 cm, respectively (measured using chamber pressures of 100 and 300 mTorr).[55]

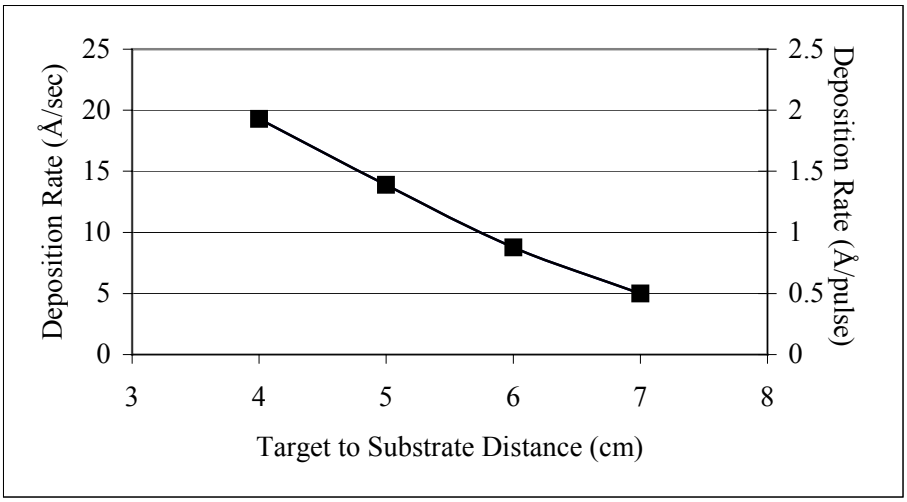

Figure 4.1 Deposition rate as a function of target to substrate distance for films grown using the $Bi_2Zn_{2/3}Nb_{4/3}O_7$ target, a substrate temperature of 550 °C, a laser frequency of 10 Hz, and a chamber pressure of 200 mTorr.

The area of the film with uniform thickness increased as the target to substrate distance was increased, as is characteristic of the PLD process.[9] For most of the experiments in this study, a target to substrate distance of 7 cm was chosen because it produced films with the largest uniform thickness across the substrate. The typical variation in the thickness of a film across a 1.5 cm x 1.5 cm substrate deposited at a target to substrate distance of 7 cm was $\pm$ 200 Å for a 2000 Å thick film. The target to substrate

distance of 7 cm was also chosen because the growth rate of the films was the lowest. The low growth rate was chosen to facilitate rearrangement of the material on the substrate before the next pulse.

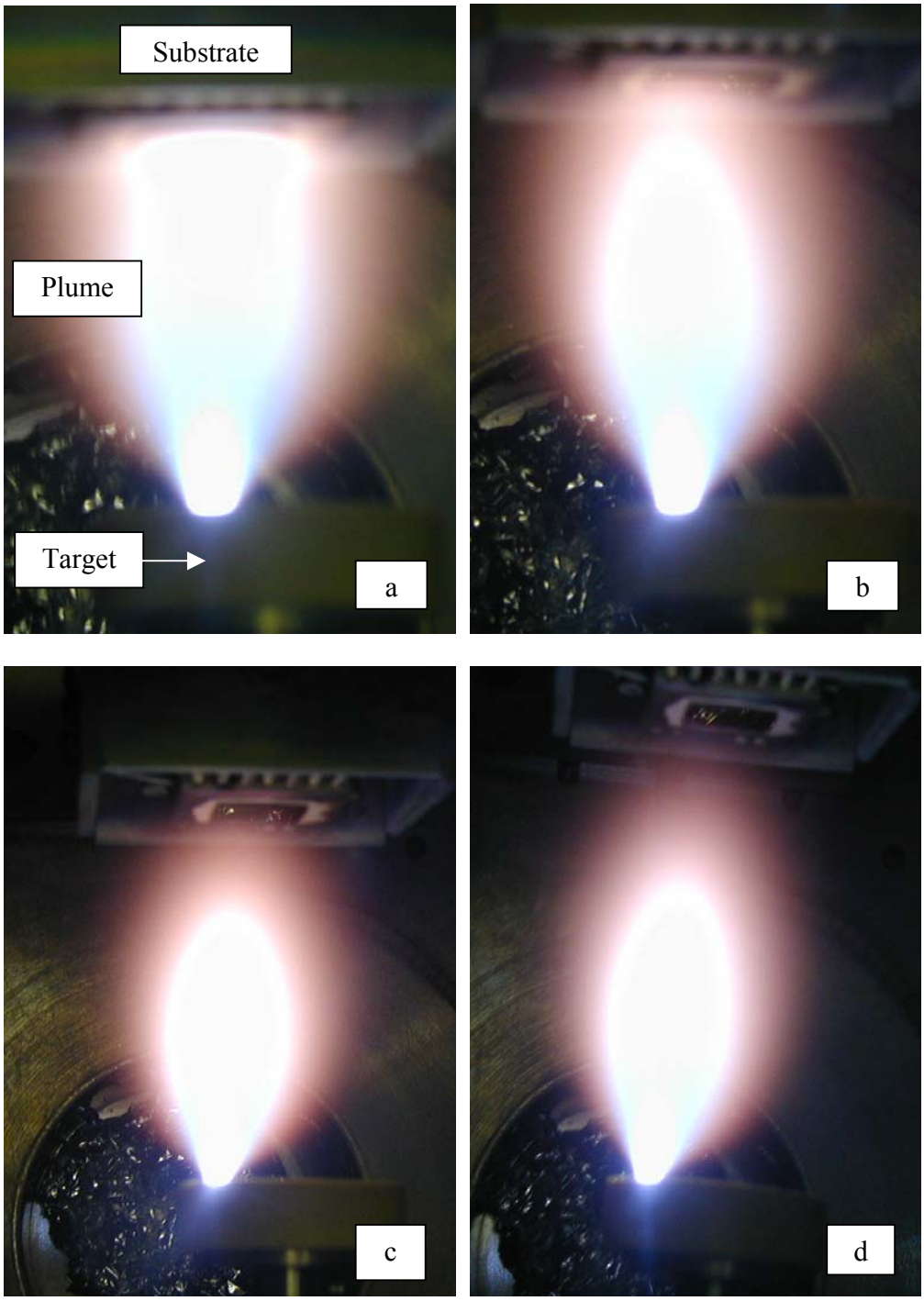

Figure 4.2 Plasma plume as a function of target to substrate distance: a) 4 cm; b) 5 cm; c) 6 cm; d) 7 cm. The images were taken using the BZN-1 target at a chamber pressure of 100 mTorr.

4.1.2 Deposition Pressure

The deposition pressure was varied from 50 mTorr to 400 mTorr with a target to substrate distance of 7 cm, and a laser frequency of 3 Hz. Figure 4.3 shows the deposition rate as a function of chamber pressure. The deposition rate increased as the chamber pressure was increased. Figure 4.4 shows images of the plasma plume as a function of chamber pressure. The plume narrows as the chamber pressure is increased. As the plume becomes more focused, the deposition rate increases. The change in the plume size is caused by the increased number of collisions between the plume and the gas in the chamber.[9] This increase in deposition rate was also observed by Lichtenwainer et al. in PLD work on PZT. In that work, the deposition rate was measured at O_2 pressures of 10, 100, 300, and 900 mTorr. It was found that the deposition rate increased with pressure up to 300 mTorr, but by 900 mTorr the deposition rate decreased.[55] The plume was observed to focus as the chamber pressure was increased, which resulted in the initial increase in deposition rate. The authors claimed that once the chamber pressure was too high, the effect of gas scattering within the plume lead to a decrease in the deposition rate.[55] The work in this thesis appears to correspond to the lower pressure portion of their data.

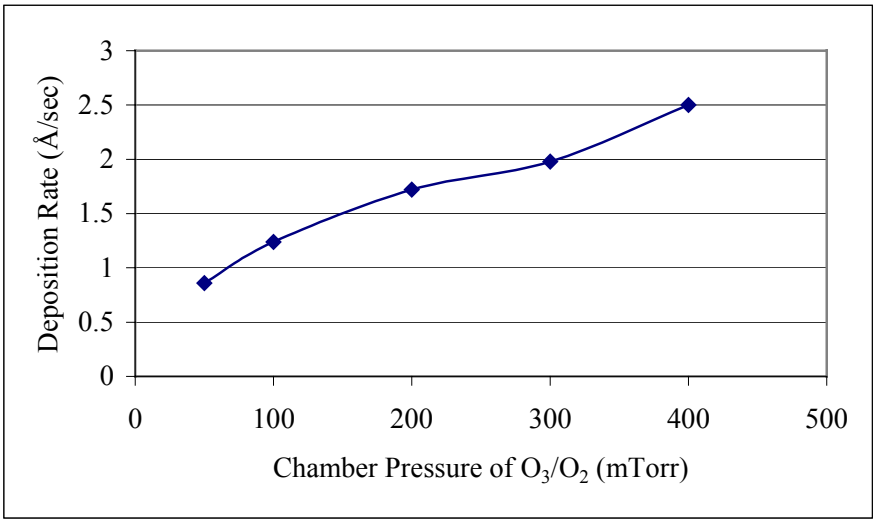

Figure 4.3 Deposition rate as a function of chamber pressure (of 10 % O_3 and 90 % O_2) for films deposited at 550 °C, at a target to substrate distance of 7 cm, and at a laser frequency of 3 Hz.

Figure 4.5 shows SEM images of the surface morphology as a function of chamber pressure for films that are ~3000 Å thick. As the pressure increased, the surface of the films appears to be rougher, which is consistent with lower adatom mobility of the deposited species. This was probably caused by the increased number of collisions with the background gas, which caused a decrease in the energy of the species in the plasma plume, and decreased bombardment. All of the films show an average grain size of 50 nm. Fox et al. measured the grain size of the platinum on Pt/Ti/SiO_2/Si wafers after annealing at 650 °C for 20 minutes and observed ~ 50 nm columnar grains.[54] This indicates that there is limited adatom mobility on the surface of the growing film and that the growth is probably dominated by the substrate morphology. Figure 4.6 shows the cross sectional TEM image of a film grown at 100 mTorr. The film shows dense columnar structure.

Figure 4.7 shows the x-ray diffraction patterns of films grown using a BZN-1.0 target as a function of chamber pressure. The films are crystalline and single-phase cubic pyrochlore (within the XRD detection limits), when grown at chamber pressures above 100 mTorr. The film grown at 50 mTorr shows a second phase of bismuth niobate. The possible cause of the formation of the secondary phase of bismuth niobate will be discussed more in the next section. The Scherrer formula was used to estimate the crystallite size which was calculated to be ~ 60 nm.[56] This is similar to the observed morphology shown in Figure 4.5 and Figure 4.6. This indicates that each grain is a single crystallite.

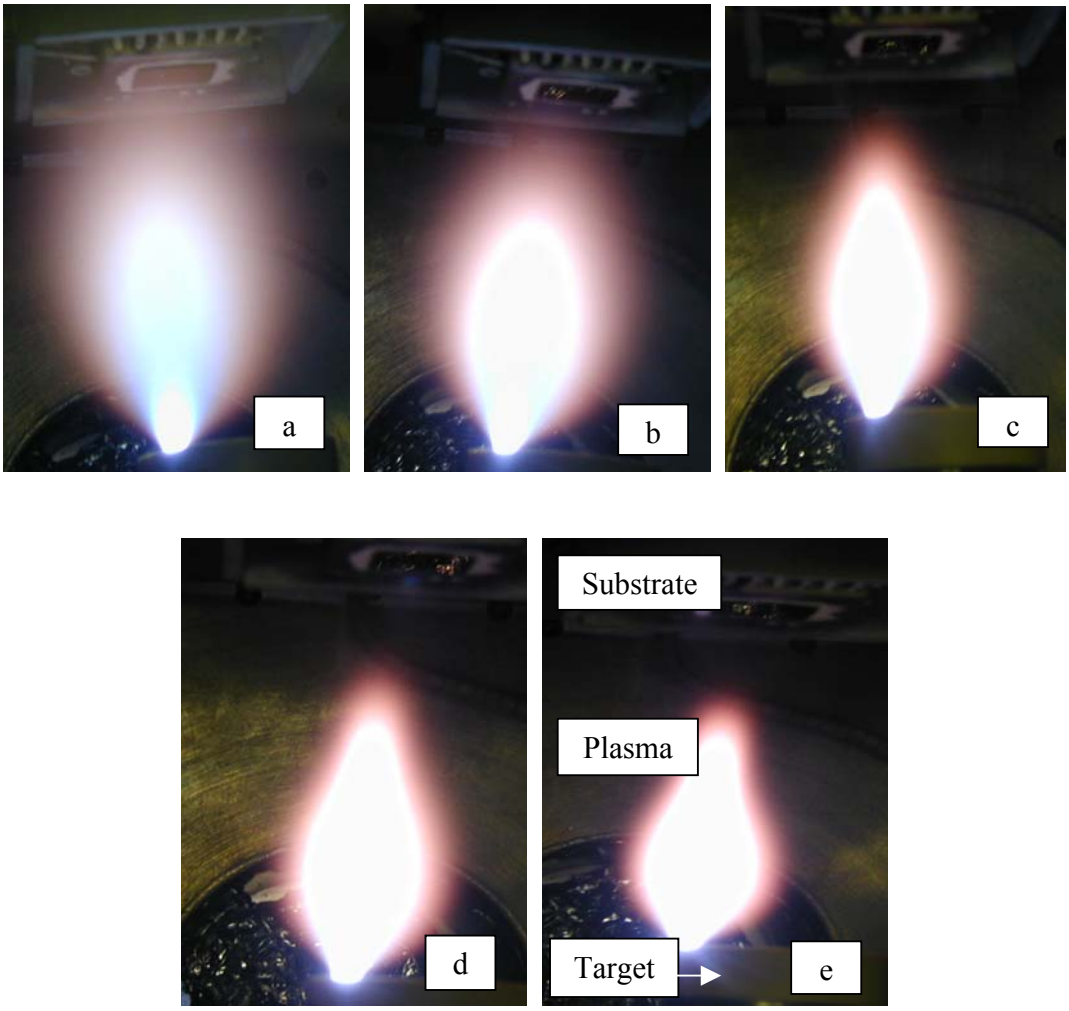

Figure 4.4 Plasma plume as a function of chamber pressure: a) 50 mTorr; b) 100 mTorr; c) 200 mTorr; d) 300 mTorr; e) 400 mTorr.

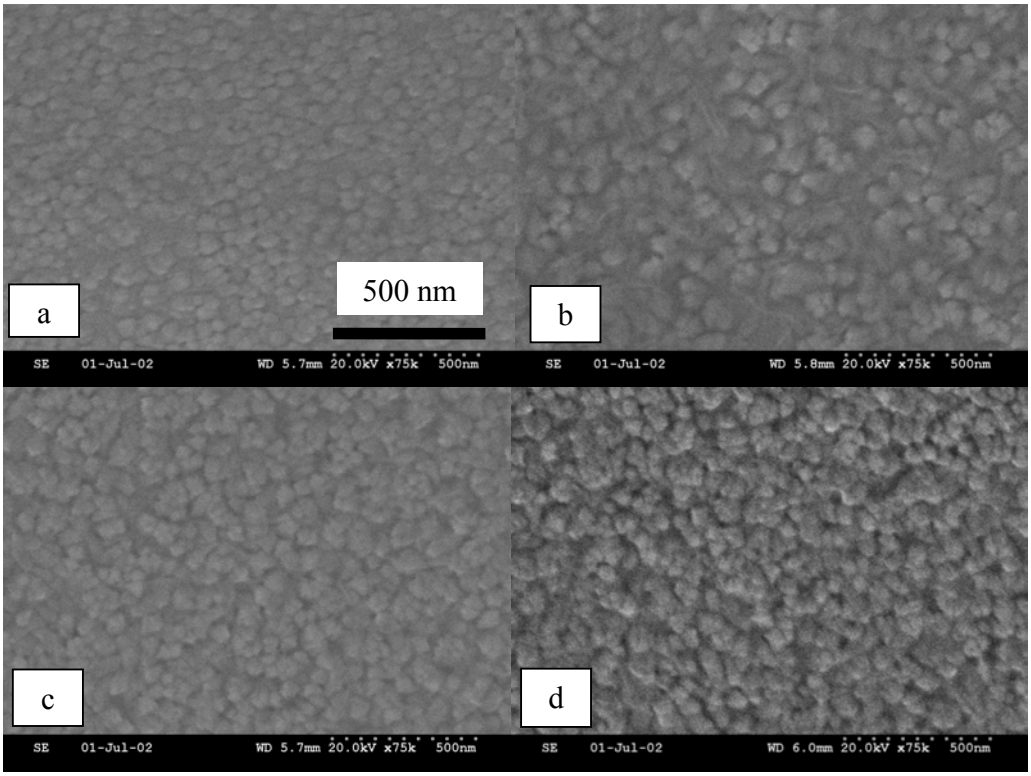

Figure 4.5 Surface morphology as a function of chamber pressure: a) 100 mTorr; b) 200 mTorr; c) 300 mTorr; d) 400 mTorr. The films were deposited using the BZN-1 target, on Nova substrates, at a target to substrate distance of 7 cm, a substrate temperature of 550 °C, and a laser frequency of 3 Hz. Films were ~ 300 nm thick.

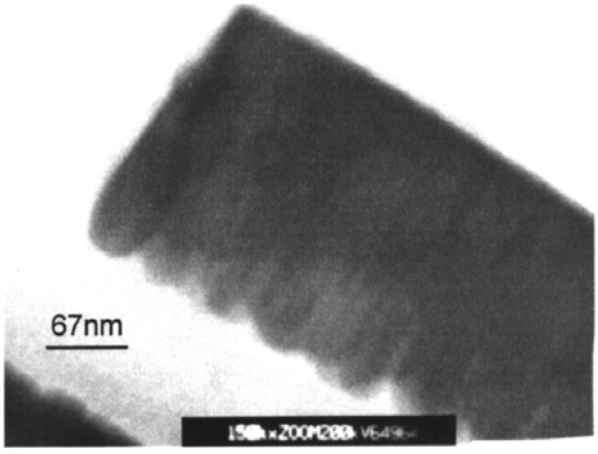

Figure 4.6 TEM cross sectional image of a film deposited using the BZN-1.0 target, at a substrate temperature of 550 °C, a chamber pressure of 100 mTorr, a target to substrate distance of 7 cm, and a laser frequency of 3 Hz. Image courtesy of Dr. Jaenam Kim.

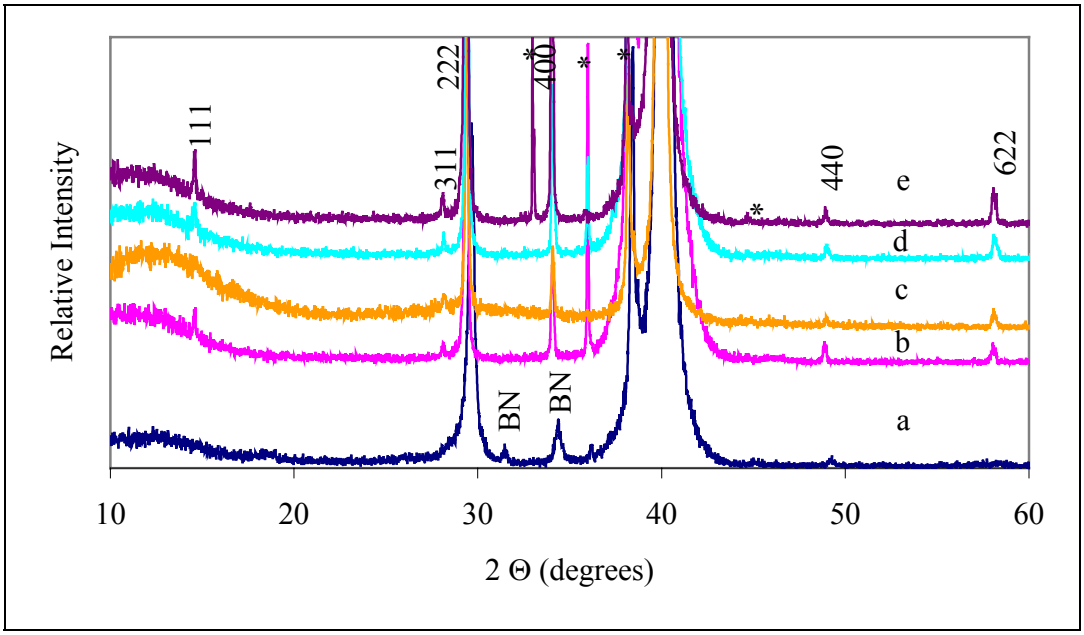

Figure 4.7 X-ray diffraction patterns as a function of chamber pressure for films grown from the BZN-1.0 target, at a substrate temperature of 550 °C, a laser frequency of 3 Hz, and a target to substrate distance of 7 cm. * denotes substrate peaks and BN stands for $BiNbO_4$. The amorphous hump around 12° 2θ is from the substrate holder. Indexed peaks are from the cubic pyrochlore phase. a) 50 mTorr, b) 100 mTorr, c) 200 mTorr, d) 300 mTorr, e) 400 mTorr.

4.1.3 Laser Frequency

Figure 4.8 shows the deposition rate as a function of laser frequency for films deposited using the BZN-1 + 0.11 mol Bi_2O_3, at a target to substrate distance of 7 cm, a substrate temperature of 550 °C, and a chamber pressure of 100 mTorr. The deposition rate increased as the laser frequency was increased. Approximately the same amount of material was deposited on the substrate each laser pulse. Figure 4.9 shows the x-ray diffraction patterns for the films as a function of laser frequency. The crystallinity of the films does not change as a function of laser frequency.

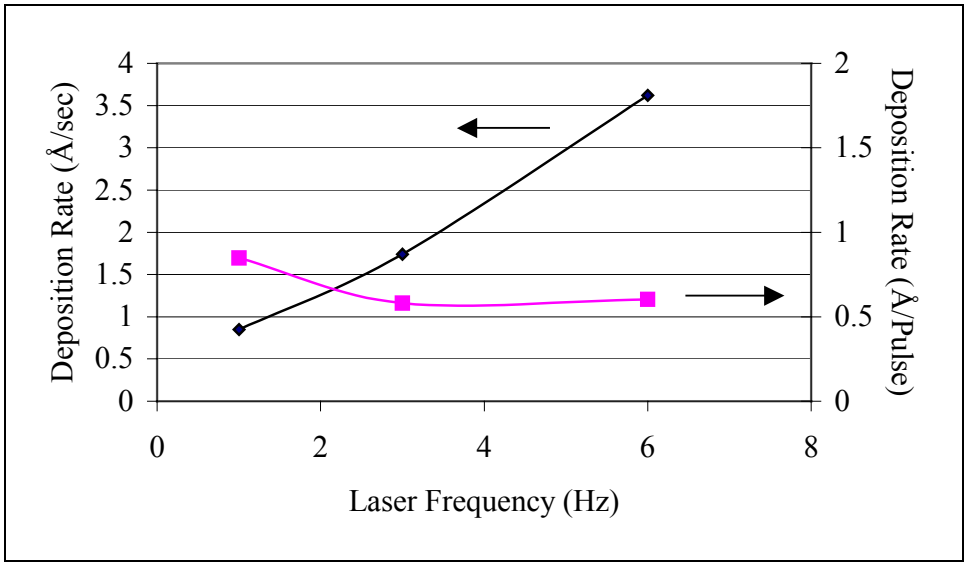

Figure 4.8 Laser frequency as a function of deposition rate for films grown using the BZN-1 + 0.11 mol Bi_2O_3 target, at a target to substrate distance of 7 cm, a substrate temperature of 550 °C, and a chamber pressure of 100 mTorr.

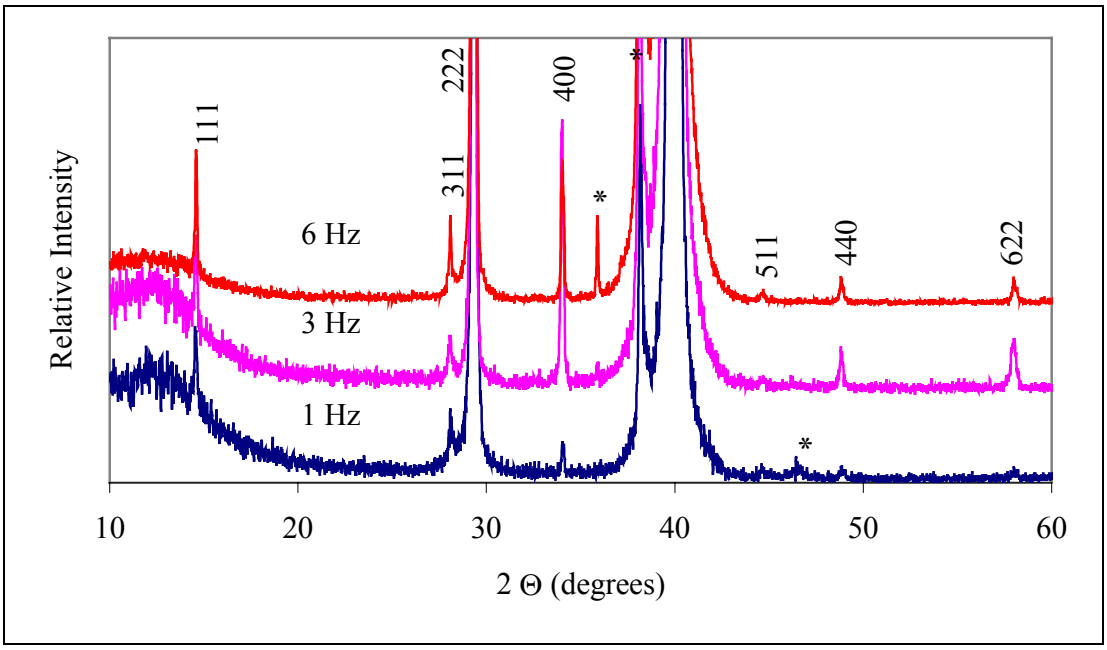

Figure 4.9 X-Ray diffraction patterns as a function of laser frequency for films grown from the BZN-1.0 + 0.11 mol Bi_2O_3 target, on Nova substrates, at a target to substrate distance of 7 cm, a substrate temperature of 550 °C, and a chamber pressure of 100 mTorr. * denotes substrate peaks. The amorphous hump around 12° 2θ is from the substrate holder. Indexed peaks are from the cubic pyrochlore phase.

4.2 Composition of BZN Thin Films

The composition of the films was determined by Rutherford backscattering analysis, RBS, at Argonne National lab by Dr. Peter Baldo. The accuracy of the RBS analysis is $\pm$ 5 mol % for each of the cations. The oxygen content was calculated assuming the standard oxidation state of each of the cations. This would be consistent with the possibility that any cation vacancies were ionically compensated by oxygen vacancies. Full ionization of the defects was assumed. This compensation mechanism is consistent both with the known tolerance of the pyrochlore structure to oxygen vacancies (i.e. there are $A_2B_2O_6$ pyrochlores) and with the observation (to be discussed in Section 4.3) that all of the films had low dielectric loss. The calculations would also be correct if second phases developed, since they give only global compositions. The compositions were normalized to the niobium content, because it was the least likely of the three cations to be volatile at the typical deposition temperatures and pressures.

4.2.1 Composition of BZN Thin Films as a Function of Target Composition

The initial films made by PLD were produced using stoichiometric targets and Table 4.1 shows a summary of the compositions of the target and the deposited film, for films deposited at 550 °C, a target to substrate distance of 7 cm, a laser frequency of 3 Hz, and a chamber pressure of 100 mTorr. Both of the films show bismuth and zinc deficiency, with similar transfer ratios from the target to the film for each of the cations. Figure 4.10 shows the x-ray patterns for the two films. The x-ray patterns show that both of the films crystallized into the cubic pyrochlore structure at these deposition conditions. No second phase bismuth niobate was observed here for the film from the BZN-0.5 target

even-though the Zn deficiency is substantial. TEM studies for phase purity should be completed to confirm this result.

Table 4.1 Target composition and film composition for films deposited at 550 °C, at a pressure of 100 mTorr, a target to substrate distance of 7 cm, and a laser frequency of 3 Hz.

Target Composition	Film Composition
$Bi_{1.5}Zn_{1.0}Nb_{1.5}O_7$ (BZN-1.0)	$Bi_{1.39}Zn_{0.64}Nb_{1.5}O_{6.48}$
$Bi_{1.5}Zn_{0.5}Nb_{1.5}O_{6.5}$ (BZN-0.5)	$Bi_{1.35}Zn_{0.34}Nb_{1.5}O_{6.11}$

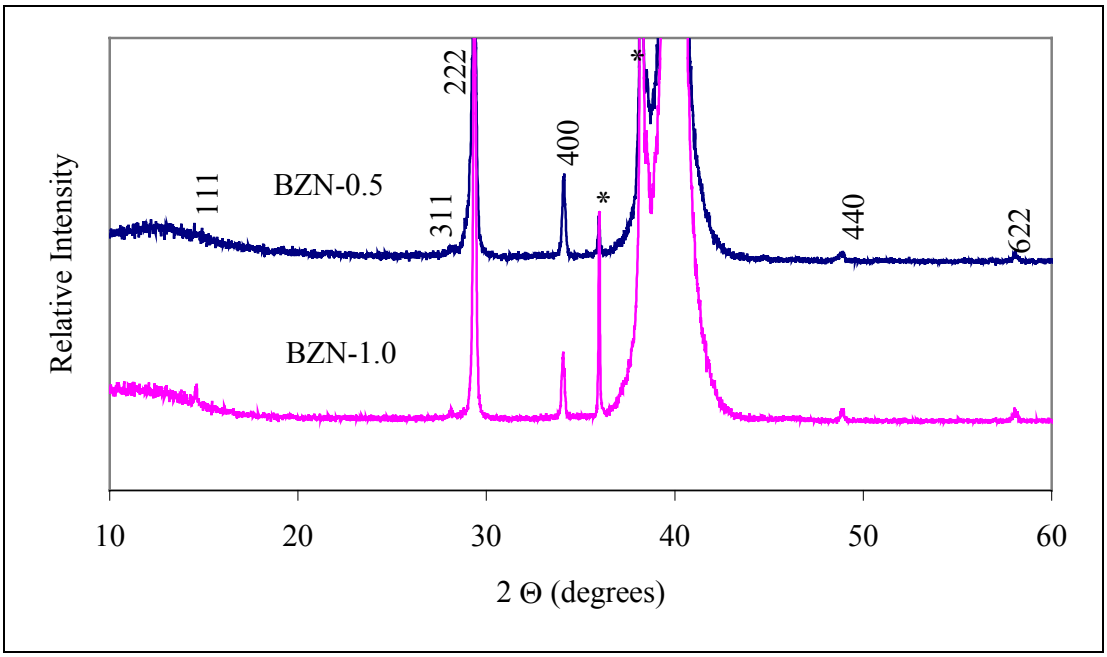

Figure 4.10 X-ray diffraction patterns for films deposited using BZN-0.5 and BZN-1.0 targets, on Nova substrates, at a substrate temperature of 550 °C, a target to substrate distance of 7 cm, a laser frequency of 3 Hz, and a chamber pressure of 100 mTorr. * denotes substrate peaks. The amorphous hump around 12° 2θ is from the substrate holder. Indexed peaks are from the cubic pyrochlore phase.

New targets were batched to add excess bismuth in the targets based on the amount that was deficient in the initial films. The zinc stoichiometry was not changed because films deposited by metal organic deposition, MOD, with the $Bi_{1.5}Zn_{0.5}Nb_{1.5}O_{6.5}$

composition showed high permittivities of 180 ($Bi_{1.5}Zn_{1.0}Nb_{1.5}O_7$ had $\varepsilon_r \sim 150$), a loss of 0.005 at 10 kHz, and could be processed 100 °C lower than BZN-1.0.[43] The resulting targets were multiphase mixtures of cubic pyrochlore and Bi_2O_3. Table 4.2 shows the composition of the new targets and the films deposited from them at a target to substrate distance of 7 cm, a laser frequency of 3 Hz, a chamber pressure of 100 mTorr. The deposition temperature was 550 °C for the BZN-1.0 compositions and 500 °C for the BZN-0.5 compositions. Figure 4.11 shows the x-ray diffraction patterns for films grown using the BZN-1.0 + 0.11 mol Bi_2O_3 and BZN-1.0 + 0.15 mol Bi_2O_3 targets. The x-ray diffraction patterns show that both films are crystalline and no secondary phases were detected. Figure 4.12 shows the x-ray diffraction for films grown using the BZN-0.5 + 0.03 mol Bi_2O_3 and BZN-0.5 + 0.15 mol Bi_2O_3. The film grown using the BZN-0.5 + 0.15 mol Bi_2O_3 shows a small amount of $BiNbO_4$ in the film. The film grown using the BZN-0.5 + 0.03 mol Bi_2O_3 shows single phase cubic BZN with the detection limits of the x-ray diffraction equipment that was used in these studies.

Table 4.2 Target composition and film composition for targets with excess bismuth.

Target Composition	Film Composition
$Bi_{1.5}Zn_{1.0}Nb_{1.5}O_7$ BZN-1.0 + 0.11 mol Bi_2O_3	$Bi_{1.46}Zn_{0.60}Nb_{1.5}O_{6.54}$
$Bi_{1.5}Zn_{1.0}Nb_{1.5}O_7$ BZN-1.0 + 0.15 mol Bi_2O_3	$Bi_{1.55}Zn_{0.54}Nb_{1.5}O_{6.62}$
$Bi_{1.5}Zn_{0.5}Nb_{1.5}O_{6.5}$ BZN-0.5 + 0.03 mol Bi_2O_3	$Bi_{1.59}Zn_{0.34}Nb_{1.5}O_{6.48}$
$Bi_{1.5}Zn_{0.5}Nb_{1.5}O_{6.5}$ BZN-0.5 + 0.15 mol Bi_2O_3	$Bi_{1.61}Zn_{0.32}Nb_{1.5}O_{6.49}$

Note: The films grown using the BZN-1.0 + 0.11 mol Bi_2O_3 and BZN-1.0 + 0.15 mol Bi_2O_3 targets were deposited at 550 °C. The films grown using the BZN-0.5 + 0.03 mol Bi_2O_3 and BZN-0.5 + 0.15 mol Bi_2O_3 targets were deposited at 500 °C. All of the films were deposited at a chamber pressure of 100 mTorr, a target to substrate distance of 7 cm, and a laser frequency of 3 Hz.

The film compositions showed that the Zn content was essentially unchanged by the addition of excess Bi for all of the targets. The measured variation of Zn content in the films is within the experimental error of RBS. Under these growth conditions, the

concentration of the Zn in the film divided by the concentration in the target is ~ 50-60 % for the BZN-1.0 targets and 60-70 % for the BZN-0.5 targets. Bulk samples of a base $Bi_{1.5}Zn_{1.0}Nb_{1.5}O_7$ composition remained single phase with Zn deficiencies of 16 mol % on the A site, but at 20 mol % there was a second phase of $BiNbO_4$.[5]

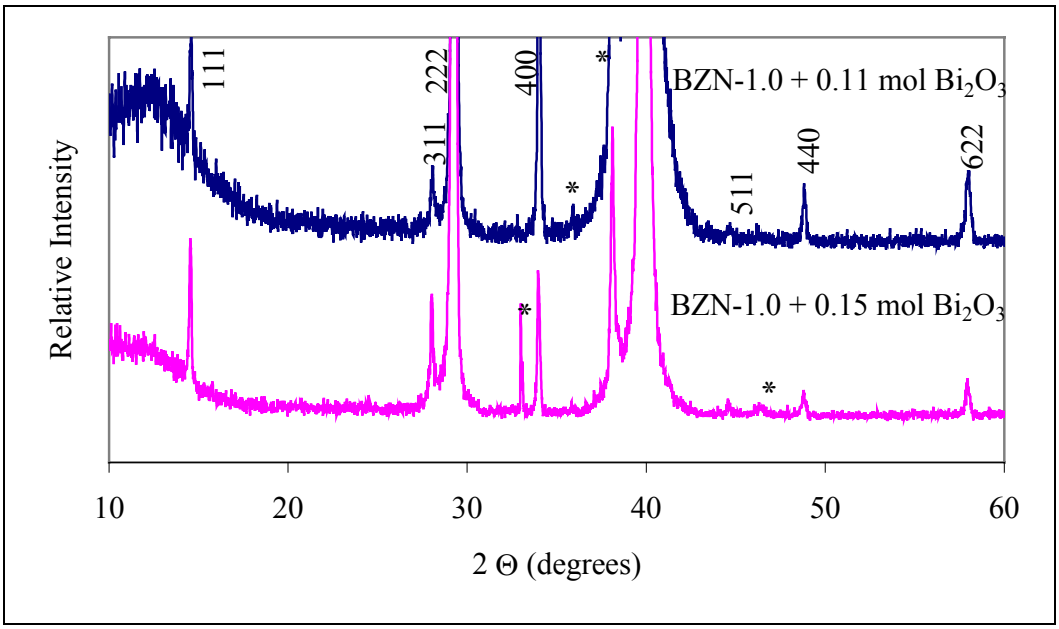

Figure 4.11 X-ray diffraction patterns as a function of target composition for films grown on Nova substrates, at a substrate temperature of 550 °C, a target to substrate distance of 7 cm, a laser frequency of 3 Hz, and a chamber pressure of 100 mTorr. * denotes substrate peaks. The amorphous hump around 12° 2θ is from the substrate holder. Indexed peaks are from the cubic pyrochlore phase.

In MOD films, it was possible to grow films with 50 mol % Zn deficiencies.[43] In this work $BiNbO_4$ was only detected in the BZN-0.5 + 0.15 mol Bi_2O_3 film processed under these conditions. It is very difficult to detect small amounts of secondary phases using standard x-ray diffraction techniques on thin film samples. It would be necessary to do high resolution TEM to confirm unambiguously if there are secondary phases present in the films. There were always problems with the BZN-0.5 films having a large

uncertainty in the lattice parameter calculations, which could suggest interference in the x-ray diffraction from a secondary phase, possibly $BiNbO_4$ or a fluorite. Further discussion on the Zn composition will be given in the section on composition as a function of pressure. If the x-ray diffraction phase purity results are correct, it would suggest that it may be possible to minimize the appearance of $BiNbO_4$ in bulk ceramic specimens by decreasing the concentration of bismuth in the samples.

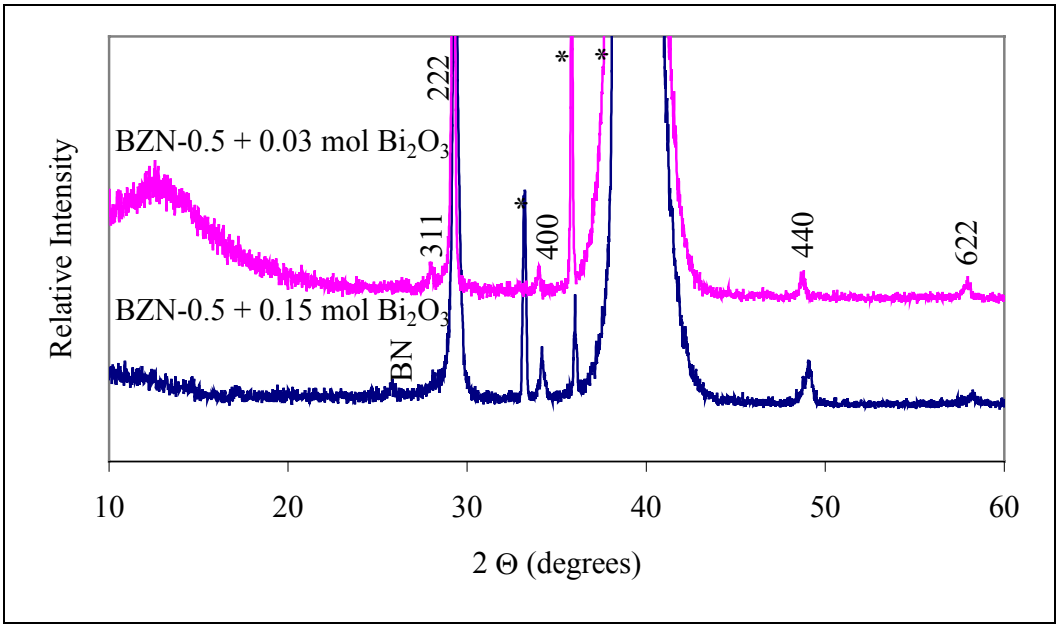

Figure 4.12 X-ray diffraction patterns as function of target composition for films grown on Nova substrates, at a substrate temperature of 500 °C, a target to substrate distance of 7 cm, a laser frequency of 3 Hz, and a chamber pressure of 100 mTorr. * denotes substrate peaks and BN stands for $BiNbO_4$. The amorphous hump around 12° 2θ is from the substrate holder. Indexed peaks are from the cubic pyrochlore phase.

4.2.2 Composition as a Function of Laser Exposure

The film composition was studied as a function of laser exposure of the target. This study was completed to determine if there were changes in the composition of the film as function of laser ablation of the target. Table 4.3 shows the film composition as a

function of laser exposure of the target. The differences in composition between films deposited as a function of laser exposure are within the measurement error of RBS analysis. It can be concluded that the composition does not change as a function of laser exposure between 1200-6600 shots by the laser, which were the typical range of shots used to grow all of the films in this study.

Table 4.3 Film composition as a function of laser exposure of the target.

Laser shots on the target	Film Composition
1260	$Bi_{1.56}Zn_{0.54}Nb_{1.5}O_{6.63}$
6660	$Bi_{1.62}Zn_{0.51}Nb_{1.5}O_{6.69}$

Note: Films were deposited using the BZN-1.0 + 0.15 mol Bi_2O_3 target, at a target to substrate distance of 7 cm, at a laser frequency of 3 Hz, a deposition temperature of 550 °C, and a chamber pressure of 100 mTorr.

4.2.3 Composition as a Function of Target to Substrate Distance

The film composition was studied as function of target to substrate distance to determine the effects of the position of the substrate in relation to the plasma plume. Table 4.4 shows the film composition as a function of target to substrate distance. As the target to substrate distance is decreased, the bismuth content in the film is decreased. The zinc content remains unchanged within the error of the RBS.

Table 4.4 Film composition as a function of target to substrate distance.

Target to substrate distance (cm)	Film composition
4	$Bi_{1.24}Zn_{0.52}Nb_{1.5}O_{6.13}$
5	$Bi_{1.30}Zn_{0.53}Nb_{1.5}O_{6.23}$
6	$Bi_{1.45}Zn_{0.48}Nb_{1.5}O_{6.41}$
7	$Bi_{1.55}Zn_{0.54}Nb_{1.5}O_{6.62}$

Note: The films were deposited using the BZN-1.0 + 0.15 mol Bi_2O_3 target. The films were deposited at substrate temperature of 550 °C, a chamber pressure of 100 mTorr, and a laser frequency of 3 Hz.

Compositional differences from the target to the film can be caused by several factors. Stoichiometric differences in the BZN films appear to be dominated by different angular distributions of species within the plasma plume and resputtering effects. Large composition changes based on being below the power density threshold for ablation were ruled out based on composition data as a function of gas pressure (see section 4.2.6).

The angular distribution of species in a background gas would be expected to preferentially broaden the angular distributions of the low-mass species, because even small collisionally-induced momentum changes would result in large velocity changes.[9] At a chamber pressure of 100 mTorr the shape of the plume is broad, and zinc species probably have the broadest spread of all of the cations inside the plume because they are the lightest. Thus, only ~50 % of the zinc reaches the substrate. The other 50 % of the zinc is located on the periphery of the plume and does not reach the substrate. Thus, the zinc species would not be affected strongly by changes in target to substrate distances, which would account for the relative independence of zinc content on this variable.

In contrast, the trajectories of high-mass plume particles are relatively unaffected by background gas collisions, since a larger change in momentum would be required to effect any changes in the particle velocity.[9] This indicates that the bismuth or bismuth oxide, probably the heaviest plume species, would be located in the center of the plasma plume. A diagnostic technique, like optical spectroscopy, would be needed to confirm the angular distributions of the species in the plasma plume.

The cause of the decrease in bismuth content could be resputtering associated with the energetic bombardment of the growing film in the plasma plume. Similar, resputtering was observed in $Ba(Pb_{0.75}\ Bi_{0.25})O_3$ films grown using a sputtering system.

At a chamber pressure of 100 mTorr, the films were highly barium deficient directly under the target where resputtering should be most severe. As the substrate was moved away from the target, the barium concentration approached the target composition.[57] Bismuth and its oxides have high volatilities, so it is reasonable that bombardment could cause the resputtering of bismuth, yielding the observed bismuth deficiency in the film. Resputtering has been reported to be observed in the vapor phase growth of many materials.[58,59] Figure 4.2 showed that the substrate is located inside the plasma plume at target to substrate distances less than 6 cm. This could lead to an increase in bombardment from a number of effects. First, smaller to target to substrate distances would lead to less thermalization of the plume species. Secondly, the resulting charge acquired by the substrate surface could increase the level of bombardment by charged species in the plume. This could explain why the samples grown at target to substrate distances greater than 5 cm have significantly more bismuth in the film. The constant zinc content with target to substrate distances of 4 to 7 cm suggests that resputtering is less critical for this element.

Note that there was no indication of an increase in the substrate temperature as the substrate was moved further inside the plasma plume measured by the thermocouple located behind the substrate during the deposition.

4.2.4 Composition as a Function of Deposition Temperature

Another reason for the bismuth and zinc deficiencies could be evaporation. Table 4.5 shows the melting temperatures for some of the species. Elemental bismuth and zinc have the lowest melting temperatures. However, they are most likely oxidized in the film.

Bi_2O_3 has the lowest melting temperature of all of the relevant oxides. Table 4.6 shows the vaporization temperatures for some of the species.

Table 4.5 The melting points for some of the BZN species.[60]

Material	Melting Point (°C)
Bi	271.40
Bi_2O_3	817
Nb	1937
Nb_2O_5	1512
Zn	419
ZnO	1975

Table 4.6 The temperature of vaporization for BZN constituents.[60,61,62]

Material	Temperature of vaporization (°C) at 5 mPa	Temperature of vaporization (°C) at 10 Pa	Temperature of vaporization (°C) at 100 Pa	Temperature of vaporization (°C) at 1600 Pa
Bi	-	768	892	-
Bi_2O_3	920	-	-	-
Nb	-	2934	3251	-
Zn	-	solid	477	-
ZnO	-	-	-	1500

Note: 1 Pa=0.0075 Torr

In order to assess whether vaporization of any of the species was critical in controlling composition, the composition was measured as a function of deposition temperature. This was done to determine two effects. First, vaporization of bismuth and zinc from the film would be expected to increase as a function of substrate temperature. Second, it is possible that the species could have different sticking coefficients as a function of substrate temperature. Table 4.7 shows the film composition as a function of deposition temperature. The variation in the zinc composition is within the experimental error of the RBS measurement, so the zinc vaporization is negligible for the deposition conditions used in this study. The bismuth content is more widely variable (also within

the experimental error), but clearly does not decrease with increasing temperature. Thus, thermally induced volatility of Bi compounds also appears to be unimportant at the temperatures utilized here. These results are consistent with reports on mass loss from MOD BZN films.[6]

Table 4.7 Film composition as a function of deposition temperature

Deposition Temperature (°C)	Film Composition
450	$Bi_{1.42}Zn_{0.50}Nb_{1.5}O_{6.38}$
550	$Bi_{1.55}Zn_{0.54}Nb_{1.5}O_{6.62}$
600	$Bi_{1.57}Zn_{0.51}Nb_{1.5}O_{6.62}$

Note: The films were deposited using the BZN-1.0 + 0.15 mol Bi_2O_3 target. The films were deposited at a target to substrate distance of 7 cm, a chamber pressure of 100 mTorr, and a laser frequency of 3 Hz.

4.2.5 Composition as Function of Laser Frequency

The effects of deposition rate on the composition of the films were studied by changing the laser frequency. The laser frequency should be an independent means of controlling growth rate, unlike target to substrate distance, where resputtering cannot be controlled independently. Table 4.8 shows the film composition as a function of the laser frequency. The differences of composition between the film deposited at 3 and 10 Hz are within the measurement error of RBS analysis. It can be concluded that the composition does not change as a function of laser frequency. This is also consistent with low volatility of all of the constituents at these temperatures.

Table 4.8 Film composition as a function of laser frequency.

Laser Frequency (Hz)	Film Composition
3	$Bi_{1.39}Zn_{0.64}Nb_{1.5}O_{6.48}$
10	$Bi_{1.41}Zn_{0.62}Nb_{1.5}O_{6.49}$

Note: Films were deposited using the BZN-1.0 target, at a substrate temperature of 550 °C, a target to substrate distance of 7 cm, and a chamber pressure of 100 mTorr.

4.2.6 Composition as a Function of Chamber Pressure

Table 4.9 shows the film composition as a function of chamber pressure. The bismuth and zinc contents both increase significantly as a function of increasing chamber pressure and approached the stoichiometry of the target. This suggests that the low Zn content at low pressures is not due to being below the ablation threshold. This observed composition changes could be due to a number of effects, including the decrease in bombardment at higher pressures or changes in the plume shape leading to better confinement of the ablated species. Figure 4.4 showed that the angular spread of the plasma plume decreased and became more focused onto the substrate as the chamber pressure was increased. The changing of the shape of the plasma plume as a function of oxygen pressure can have significant effects on the energy of the ablated species, their chemical state, and the oxygen-to-ablated species flux ratio at the substrate.[55] It is believed that in the current work, plume confinement dominates over the change in bombardment in controlling the zinc composition as a function of pressure. This is because the zinc content was essentially independent of target to substrate distance for depositions at 100 mTorr, even when the substrate was placed in the plume, where resputtering is expected to be severe.

Table 4.9 Film composition as a function of chamber pressure.

Chamber Pressure (mTorr)	Film Composition
100	$Bi_{1.39}Zn_{0.64}Nb_{1.5}O_{6.48}$
200	$Bi_{1.42}Zn_{0.74}Nb_{1.5}O_{6.62}$
300	$Bi_{1.58}Zn_{0.83}Nb_{1.5}O_{6.95}$
400	$Bi_{1.69}Zn_{0.90}Nb_{1.5}O_{7.19}$

Note: Films were deposited using the BZN-1.0 target, at a target to substrate distance of 7 cm, a laser frequency of 3 Hz, and a deposition temperature of 550 °C.

As stated previously, collisions of plume species with background gas would be expected to preferentially broaden the angular distributions of the low-mass species, since even small collisionally-induced momentum changes would be likely to result in large velocity changes.[9] This would lead to preferential depletion of zinc species from the center of the plasma plume. The substantial plume narrowing as the pressure increases could then be responsible for the dramatic increase in the zinc content as a function of increasing chamber pressure. The bismuth content also increased with increasing chamber pressure, and in some cases exceeded the target composition ratio.

Figure 4.13 shows the lattice parameter as a function of chamber pressure for films grown from the BZN-1 target. As the chamber pressure is increased, the lattice parameter of the films decreases. This is surprising because the bismuth and zinc content in the films increases as the chamber pressure increases and it might be expected that the structure would expand to accommodate the cations. It is interesting that all of the films show smaller lattice parameters than bulk $Bi_{1.5}Zn_{0.92}Nb_{1.5}O_{6.92}$, which has a lattice parameter of 10.5616 Å.[38] The origin of this is not known, but several possible causes will be discussed in the conclusions on composition.

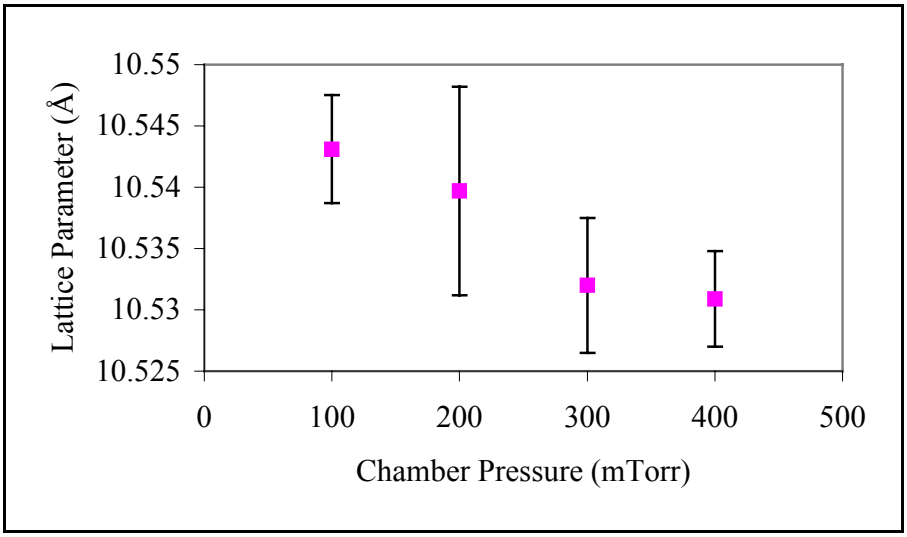

Figure 4.13 Lattice parameter as a function of chamber pressure for films grown from the BZN-1.0 target, at a substrate temperature of 550 °C, a laser frequency of 3 Hz, and a target to substrate distance of 7 cm.

4.2.6 Composition Summary

Composition control of BZN films is strongly affected by a variety of deposition conditions. It was shown that the cubic pyrochlore structure in PLD films is tolerant of substantial bismuth and zinc stoichiometry variations, at least within the detection limits of x-ray diffraction. The substrate temperature, laser frequency, and target exposure did not affect the composition of the films. The target to substrate distance and the chamber pressure had significant effects on the film composition. As the target to substrate distance decreased, the bismuth content in the film decreased and the zinc content remained relatively unchanged. This was probably caused by resputtering of the bismuth species by the plasma plume. Increasing the chamber pressure changed the shape of the plasma plume and increased the bismuth and zinc content in the films.

Figure 4.14 shows a summary of the lattice parameter as a function of chamber pressure for the three BZN-1.0 targets. It is interesting that all of the films show smaller lattice parameters than bulk $Bi_{1.5}Zn_{0.92}Nb_{1.5}O_{6.92}$, which has a lattice parameter of 10.5616 Å.[38]

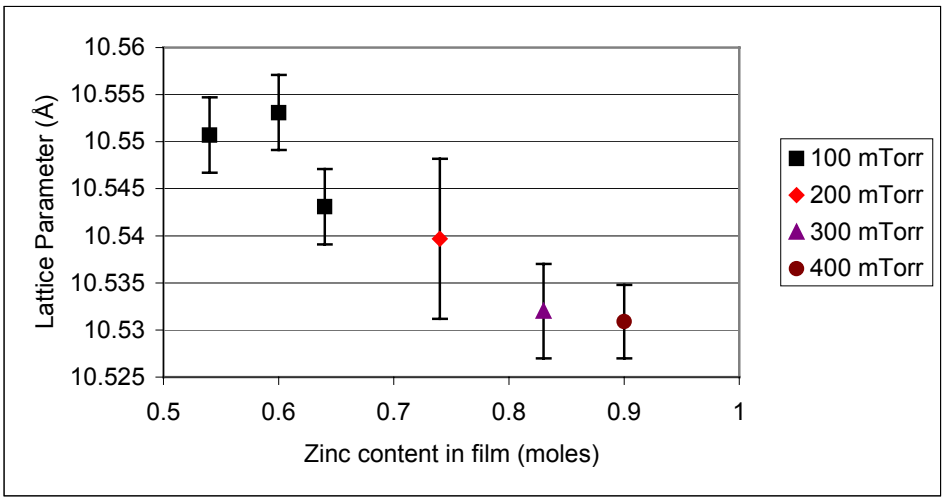

Figure 4.14 Lattice parameter as a function of zinc content for films grown at different chamber pressures.

The lattice parameters do increase towards the bulk value as the chamber pressure was decreased. There are several possible causes for these lattice parameters changes. First, as the pressure is decreased, the energetic bombardment of the growing film increases. It was observed previously that with increasing bombardment the lattice parameter increased in both $SrRuO_3$ and $Pb(Mg_{1/3}Nb_{2/3})O_3$-$PbTiO_3$ films grown by PLD.[51,63] This bombardment might account for the increase in lattice parameter as a function of decreasing pressure. A second possibility is that as the pressure is increased the changes in bismuth and zinc content could lead to the formation of a (different) secondary phase. Although all of the films reported here were single-phase as measured

by x-ray diffraction, it is very difficult to detect small amounts of second phase material in films. So, if a second phased formed, possibly a fluorite phase, this could possibly cause the stoichiometry changes yielding smaller lattice parameters than measured in bulk samples. It is also possible that with changing pressure the composition of a secondary phase would change, so that all the samples are multiphase, but with different stoichiometries and concentrations of the second phase.

Figure 4.15 shows a schematic of the proposed bismuth and zinc distributions in the plasma plume as a function of chamber pressure and target to substrate distance. As the chamber pressure increases, the plume becomes more focused and the angular distribution of the zinc and bismuth overlap each other more closely, leading to approximately stoichiometric transfer from the target to the substrate.

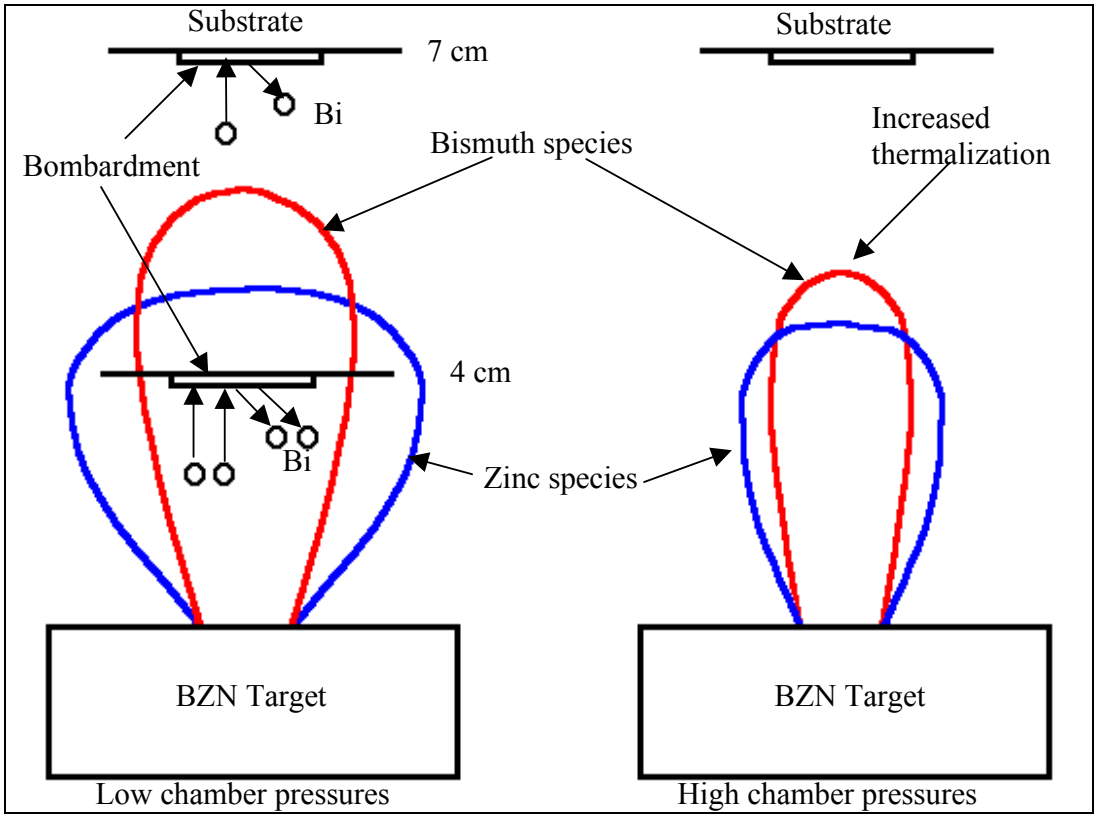

Figure 4.15 Schematic of the bismuth and zinc distributions as a function of chamber pressure and target to substrate distance.

4.3 Phase Formation

This section looks at the phase formation of the cubic pyrochlore structure as functions of the chamber pressure, laser frequency, and the substrate. Each of these parameters affects the growth of the film and has different effects on the adatom mobility of the growing film. The focus of this study was to determine the critical parameters that controlled the crystallization temperature of the cubic pyrochlore structure and to determine the minimum crystallization temperature needed to form single-phase cubic pyrochlore thin films.

4.3.1 Crystallization Temperature as a Function of Chamber Pressure

Figure 4.16 shows the x-ray diffraction patterns for films deposited using the BZN-1.0 target, on Nova substrates, at a chamber pressure of 200 mTorr, a target to substrate distance of 7 cm, and a laser frequency of 10 Hz. The films were between 350 and 450 nm thick. The films crystallized into the cubic pyrochlore structure at substrate temperatures of 550 °C and higher. Below 550 °C the films were amorphous.

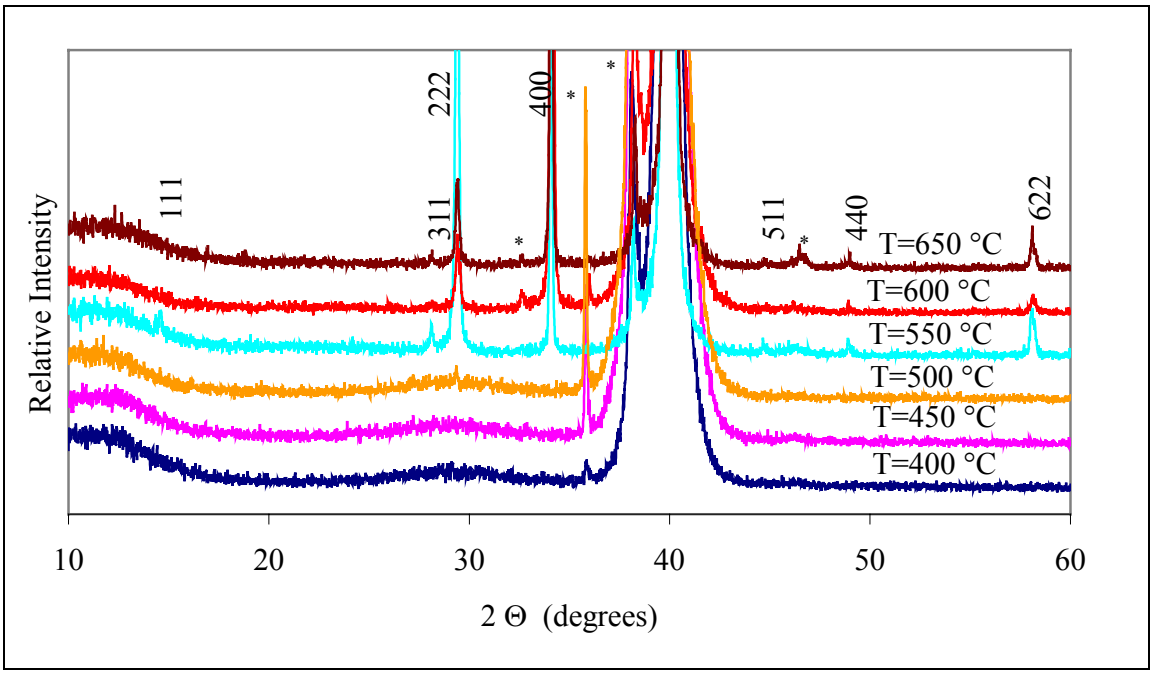

Figure 4.16 X-ray diffraction patterns for films deposited using the BZN-1.0 target, on Nova substrates, at a laser frequency of 10 Hz, a target to substrate distance of 7 cm, and a chamber pressure of 200 mTorr. * denotes substrate peaks. The amorphous hump around 12° 2θ is from the substrate holder. Indexed peaks are from the cubic pyrochlore phase.

Figure 4.17 shows the x-ray diffraction pattern for films deposited using the BZN-1.0 target, at a chamber pressure of 100 mTorr, a target to substrate distance of 7 cm, and a laser frequency of 3 Hz. Both the chamber pressure and the laser frequency were

changed for this set of samples. The laser frequency was previously shown to have no effect on the crystallization temperature (see Figure 4.9 and Figure 4.18), so it is not believed to be an important variable. The pressure was decreased in order to decrease thermalization of the arriving species. The resulting bombardment should provide additional adatom mobility to the growing film, which could decrease the crystallization temperature. From the results in Figure 4.17, it can be concluded that the crystallization temperature is 500 °C when deposited at a chamber pressure of 100 mTorr using the BZN-1.0 target.

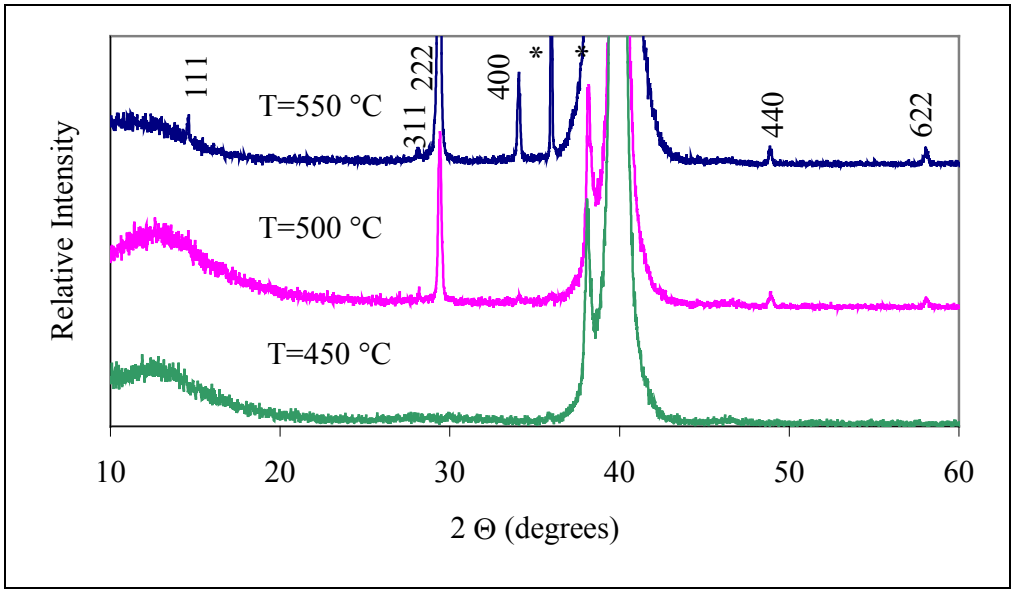

Figure 4.17 X-ray diffraction pattern for films deposited using the BZN-1.0 target, on Nova substrates, a target to substrate distance of 7 cm, a laser frequency of 3 Hz, and at a chamber pressure of 100 mTorr. * denotes substrate peaks. The amorphous hump around 12 ° 2θ is from the substrate holder. Indexed peaks are from the cubic pyrochlore phase.

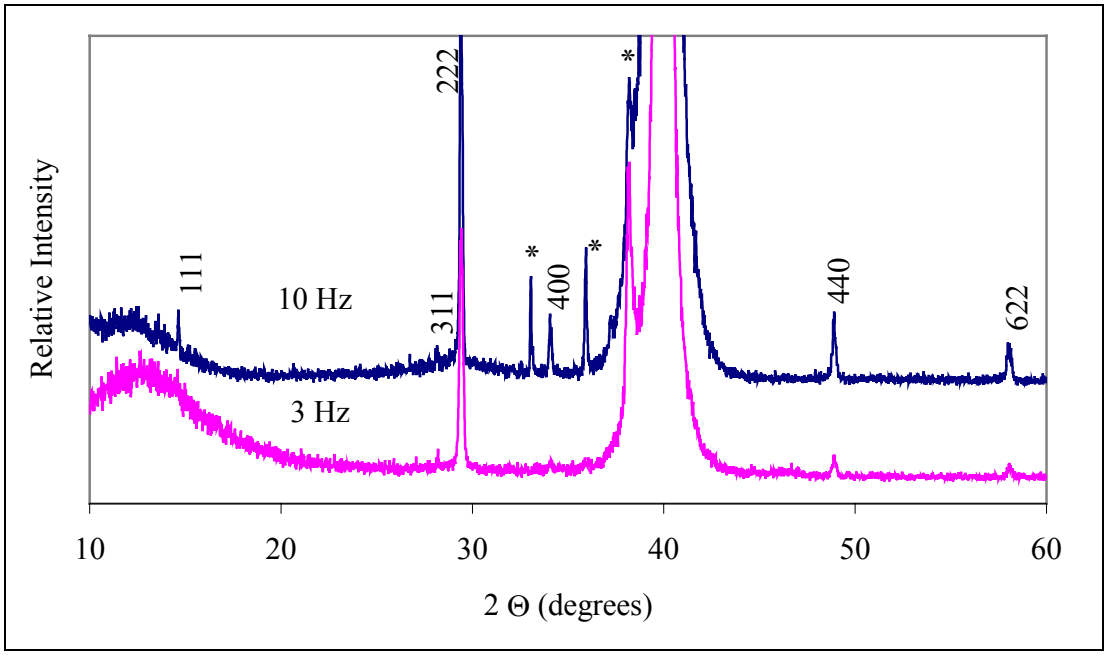

Figure 4.18 X-ray diffraction patterns as a function of laser frequency for films deposited using the BZN-1.0 target, on Nova substrates, a target to substrate distance of 7 cm, and a chamber pressure of 100 mTorr. * denotes substrate peaks. The amorphous hump around 12° 2θ is from the substrate holder. Indexed peaks are from the cubic pyrochlore phase.

Thus, the crystallization of the cubic pyrochlore structure does not seem to be strongly affected by increasing the growth rate, but it is affected by changing the chamber pressure. By reducing the chamber pressure to 100 mTorr, the crystallization temperature was reduced by 50 °C. The change in the crystallization temperature may be caused by two main factors. First, increasing the chamber pressure partially thermalizes the ablated species.[9] Films deposited under lower bombardment conditions (i.e. higher pressures) would require more energy, i.e. temperature, to cause the film to crystallize. Secondly, it was shown previously that the composition of the film changes significantly as the pressure is increased. The film grown at 100 mTorr is appreciably more Zn deficient than the one grown at 200 mTorr. It was shown in MOD films that the BZN-0.5 composition had optimized dielectric properties at a firing temperature of 650 °C versus

the BZN-1.0 composition that had optimized dielectric properties when fired at 750 °C.[6,43] It would be very interesting in the future to repeat the crystallization studies as a function of chamber pressure using a target batched with excess ZnO.

Figure 4.19 shows the AFM images as a function of substrate temperature for films deposited using the BZN-1.0 target, at a chamber pressure of 100 mTorr, a laser frequency of 3 Hz, and a target to substrate distance of 7 cm. The film deposited at 450 °C is amorphous and shows very small surface features with an average surface grain size of 10 nm. The surface grain size increases to 50 nm at the crystallization temperature of 550 °C. The microstructure of the film grown at 500 °C shows a combination of the fine microstructure at 450 °C and the larger grain structure observed at 550 °C. This might be an indication that the film grown at 500 °C is not completely crystallized and that the fine grains in the structure are amorphous. High resolution TEM studies would need to be completed to confirm this.

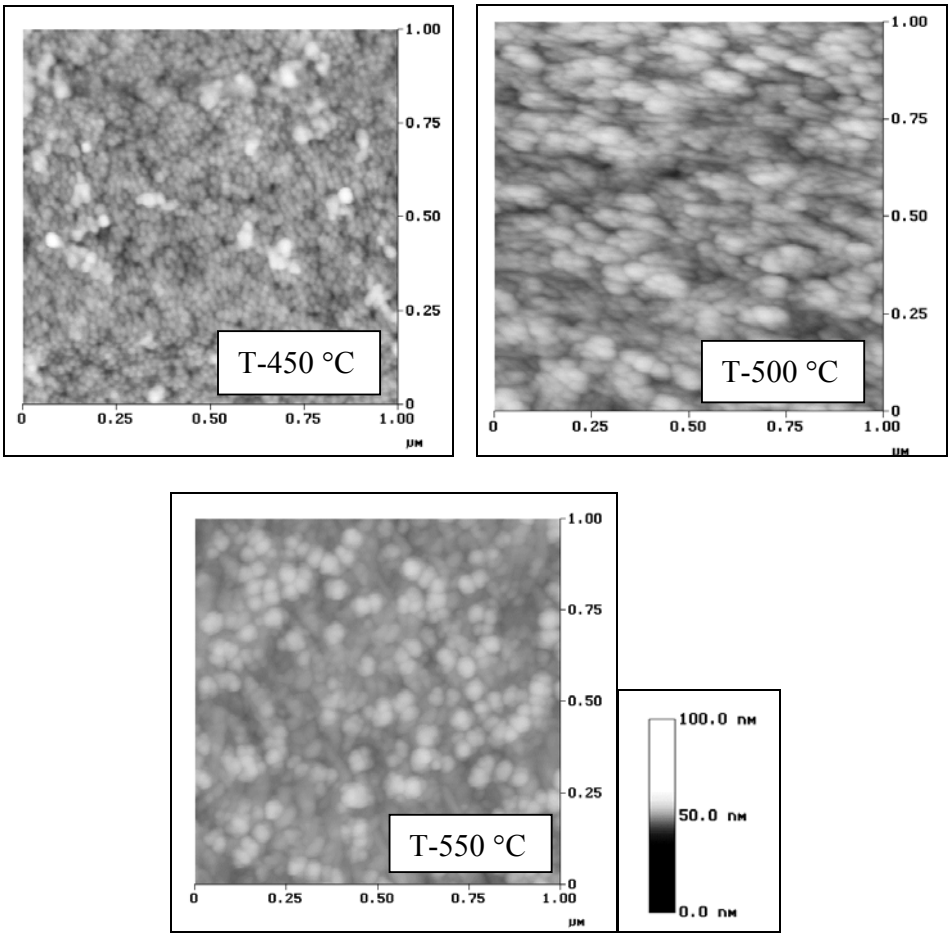

Figure 4.19 AFM images as a function of deposition temperature for films grown from the BZN-1.0 target, on Nova substrates, at a chamber pressure of 100 mTorr, a laser frequency of 3 Hz, and a target to substrate distance of 7 cm.

4.3.2 Effects of Substrate on the Crystallization Temperature

Some films were grown using platinum electrodes produced using an ultra high vacuum molecular beam epitaxy, UHV MBE, vacuum chamber (courtesy of J. P. Maria, NCSU). These wafers were Pt/ La, Pt alloy (5 vol % La in Pt)/ $La_2O_3/SiO_2/Si$. The wafers had 200 Å Pt, 800 Å Pt, La alloy (5 vol % La in Pt), 50 Å La_2O_3, and 270 Å thermal SiO_2. These wafers were used because they are more stable at high

temperatures T > 650 °C and did not require a film deposited at 250 °C, before heating to the deposition temperature. The wafers produced by UHV MBE were grown individually and there were variations between the wafers. Figure 4.20 shows the x-ray patterns for the two wafers grown by MBE. The 1st wafer pattern shows a stronger intensity (111) platinum peak than the 2nd wafer pattern. This suggests that the pattern of the 2nd wafer is either not as crystalline and/or less well textured than the 1st wafer. These differences in the wafers had dramatic effects on the crystallization temperature for the BZN-1.0.

Figure 4.21 shows two films grown under identical deposition conditions using the BZN-1.0 + 0.15 mol Bi_2O_3 target, at a deposition temperature of 450 °C, a laser frequency of 3 Hz, a target to substrate distance of 7 cm, and a chamber pressure of 100 mTorr, but on different Pt/ La, Pt alloy (5 vol % La in Pt)/ $La_2O_3/SiO_2/Si$ wafers. The film grown on the 2nd Pt/ La, Pt alloy (5 vol % La in Pt)/ $La_2O_3/SiO_2/Si$ wafer is crystalline, but the film grown on the 1st wafer is amorphous. The minimum deposition temperature on the Nova substrates was 500 °C, but by using the 2nd Pt/ La, Pt alloy (5 vol % La in Pt)/ $La_2O_3/SiO_2/Si$ wafer, the crystallization temperature was lowered to 450°C. These results indicate that the 2nd Pt/ La, Pt alloy (5 vol % La in Pt)/ $La_2O_3/SiO_2/Si$ wafer enhances the nucleation of cubic BZN and lowers the crystallization temperature. This is advantageous to the use of BZN films for on-chip applications, such as integrated decoupling capacitors or on-chip capacitors.

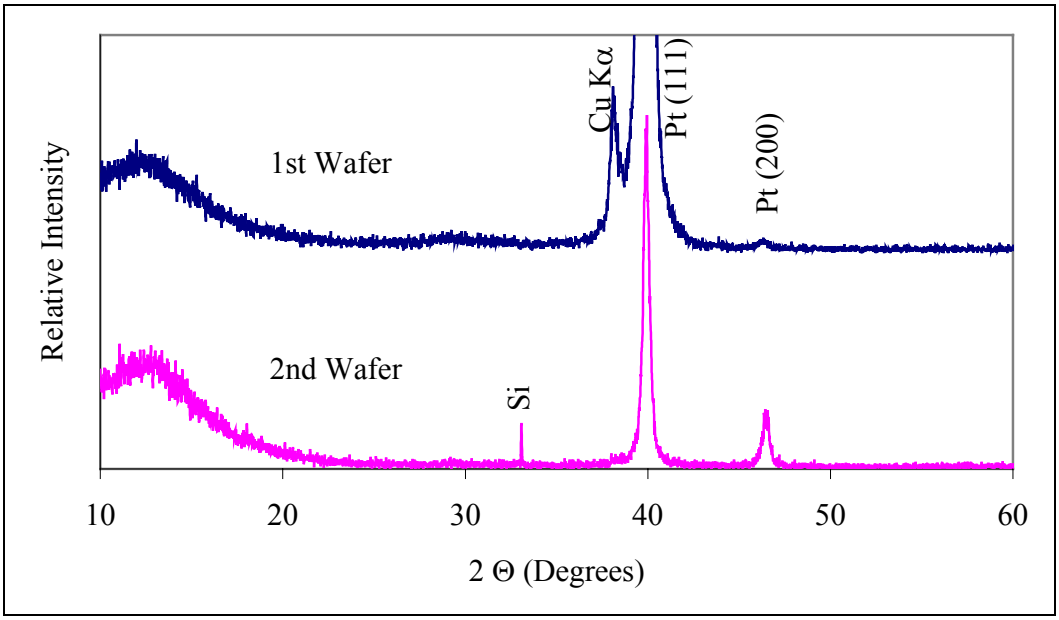

Figure 4.20 X-ray diffraction patterns for two of the Pt/ La, Pt alloy (5 vol % La in Pt)/ $La_2O_3/SiO_2/Si$ wafers. The amorphous hump around 12° 2θ is from the substrate holder.

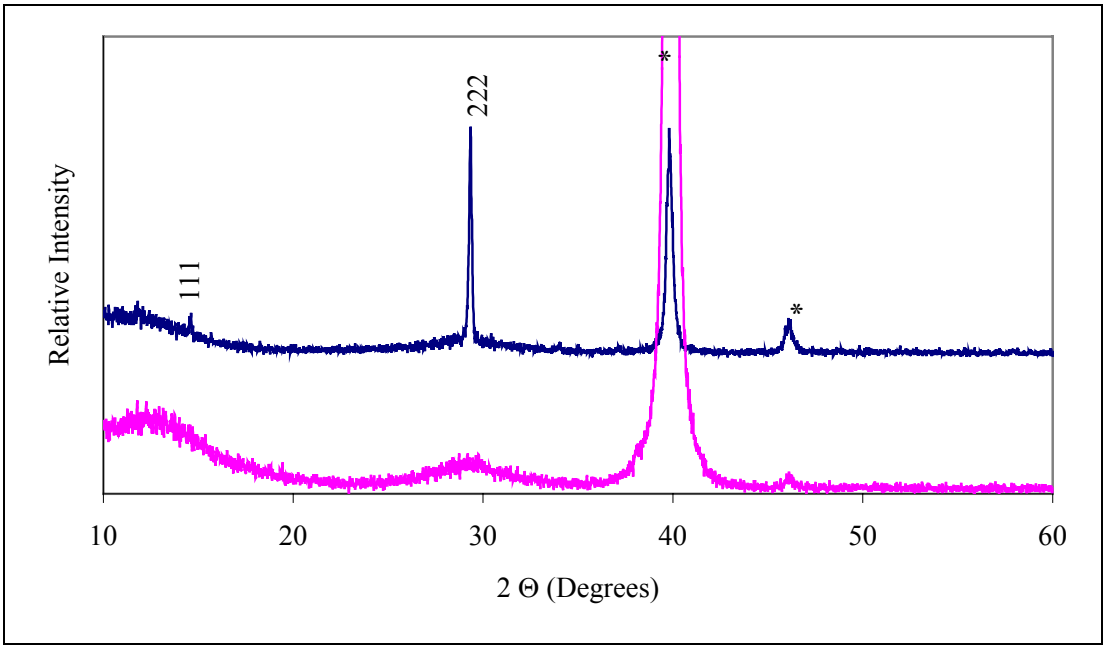

Figure 4.21 X-ray diffraction pattern for two films deposited using the BZN-1.0 + 0.15 mol Bi_2O_3 target, at a deposition temperature of 450 °C, a laser frequency of 3 Hz, a chamber pressure of 100 mTorr, and a target to substrate distance of 7 cm. The bottom pattern was deposited on the 1st Pt/ La, Pt alloy (5 vol % La in Pt)/ $La_2O_3/SiO_2/Si$ wafer and the top pattern was deposited on the 2nd Pt/ La, Pt alloy (5 vol % La in Pt)/ $La_2O_3/SiO_2/Si$ wafer. * denotes substrate peaks. The amorphous hump around 12° 2θ is from the substrate holder. Indexed peaks are from the cubic pyrochlore phase.

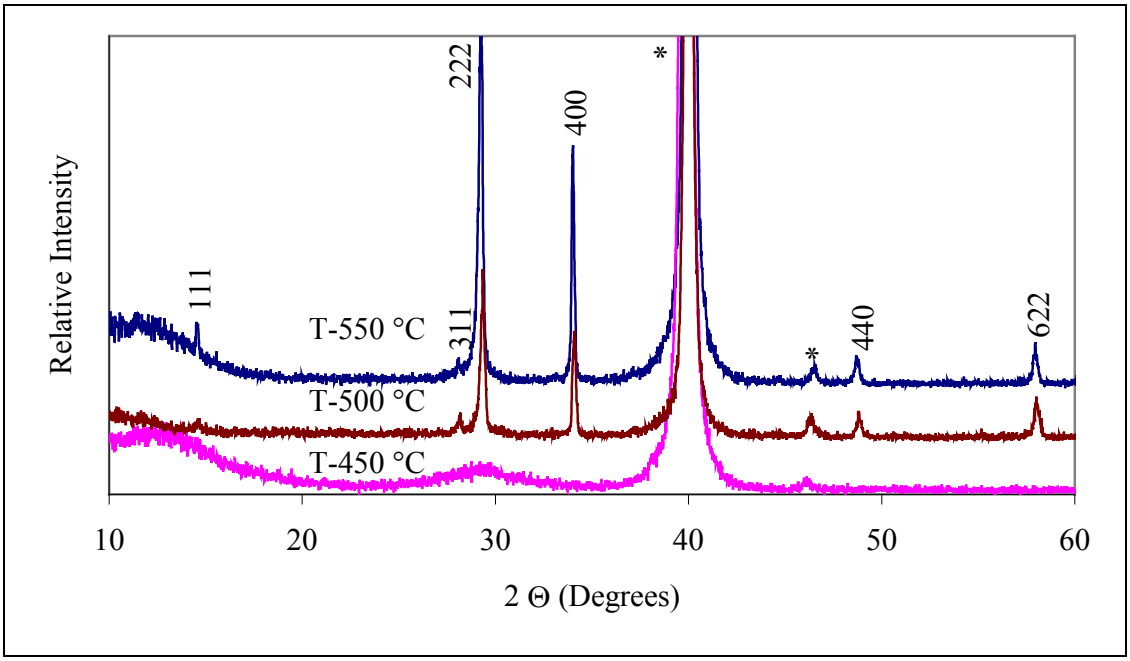

Figure 4.22 X-ray diffraction patterns for films as a function of deposition temperature, on the 1st Pt/ La, Pt alloy (5 vol % La in Pt)/ $La_2O_3/SiO_2/Si$ wafer, using the BZN-1.0 + 0.15 mol target, at a chamber pressure of 100 mTorr, a laser frequency of 3 Hz, and a target to substrate distance of 7 cm. * denotes substrate peaks. The amorphous hump around 12° 2θ is from the substrate holder. Indexed peaks are from the cubic pyrochlore phase.

4.4 Dielectric Properties

4.4.1 Permittivity as a Function of Deposition Temperature

Figure 4.23 shows the permittivity as a function of deposition temperature for films deposited using the BZN-1.0 base composition. The maximum permittivity occurs at the maximum deposition temperature for all three of the targets in Figure 4.23. The loss is less then 0.007 for all of the films. The films deposited at 450 °C were amorphous and the films were crystalline at deposition temperatures of 500 °C and above. The films grown at a substrate temperature of 450 °C were grown using a chamber pressure of 50

mTorr. The pressure of 50 mTorr was selected to determine if increasing the energy of the species of the plume would decrease the deposition temperature. This approach was shown previously (Figure 4.17) to be successful in reducing the crystallization temperature to 500 °C by lowering the pressure from 200 mTorr to 100 mTorr. However, it was found that using a chamber pressure of 50 mTorr was not sufficient to lower the deposition temperature further.

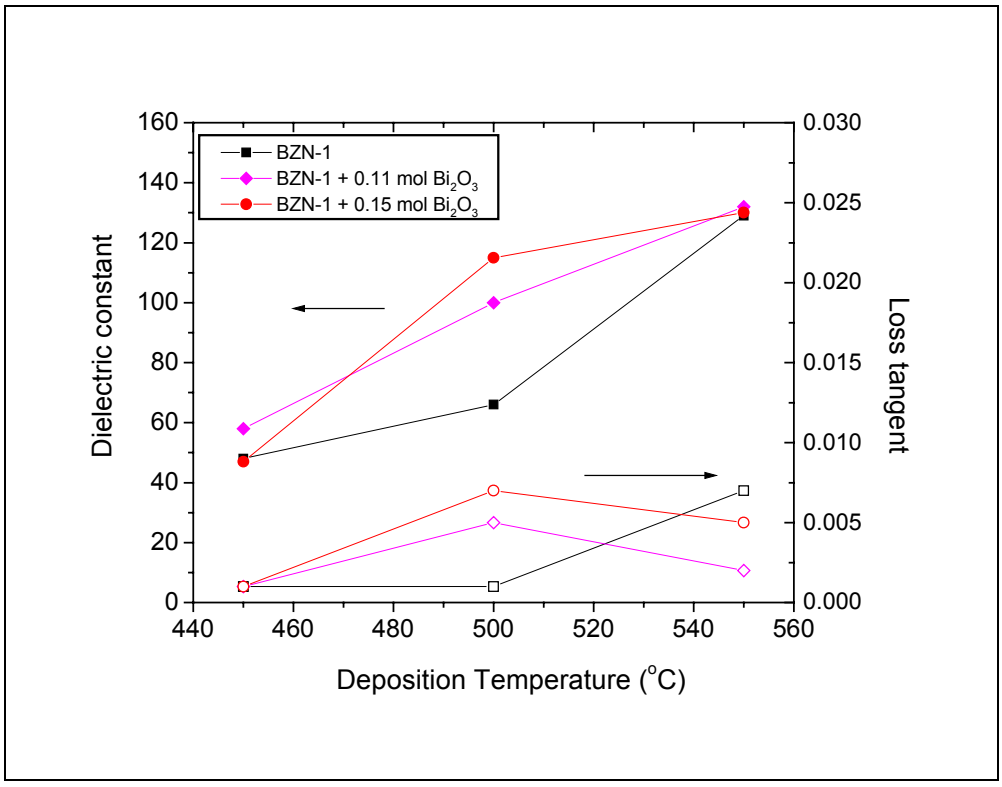

Figure 4.23 Permittivity as a function of deposition temperature for films deposited using the base composition of BZN-1.0, on Nova substrates, at a target to substrate distance of 7 cm, and a laser frequency of 3 Hz. The films deposited at 450 °C were deposited using a chamber pressure of 50 mTorr. The films deposited at 500 °C and 550 °C were deposited using a chamber pressure of 100 mTorr. The measurements were completed at room temperature using a frequency of 10 kHz and an oscillation voltage of 0.03 V.

It was shown previously in Table 4.7 that the composition did not change as a function of deposition temperature. The bismuth content in the film increases with the

addition of excess bismuth in the target from a bismuth content of 1.39 $\pm$ 0.07 moles in the BZN-1.0 target, 1.46 $\pm$ .07 moles in the BZN-1.0 + 0.11 mol Bi_2O_3 target, and 1.55 $\pm$ 0.08 moles in the BZN-1.0 + 0.15 mol Bi_2O_3 target. The permittivity remained relatively the same, ranging from 129 to 132 at a deposition temperature of 550 °C as the bismuth content was increased in the films.

The zinc content remains approximately unchanged in the films and ranges between 0.64 $\pm$ 0.03 moles for the film grown using the BZN-1.0 target, 0.60 $\pm$ 0.03 moles for the film grown using the BZN-1.0 + 0.11 mol Bi_2O_3 target, and 0.54 $\pm$ 0.03 moles for the film grown using the BZN-1.0 + 0.15 mol Bi_2O_3 target.

The maximum permittivity of 132 for the films grown using the targets with the excess bismuth is lower than the maximum permittivity, 150, measured in metal organic deposited films and bulk samples with the composition of $Bi_{1.5}Zn_{1.0}Nb_{1.5}O_7$.[6,36] The MOD films with the BZN-0.5 composition have permittivities of 180.[43] The maximum deposition temperature used in PLD is 200 °C lower than the firing temperature of 750 °C required for the MOD films to have a permittivity of 150.[6] The MOD films that were fired at temperatures between 700-550 °C have dielectric permittivities between 130 to 90, and the loss is ≤ 0.008 at 10 kHz.[6] There are several possibilities for the lower permittivity in the PLD films. First the films may not be completely crystallized into the correct phase at a deposition temperature of 550 °C. This corresponds well with the observations in MOD films that the permittivity increased with increasing firing temperatures. TEM studies would need to be completed to determine if there are regions of amorphous or second phase material in the films. A second possibility is that the PLD

films deposited at temperatures ≤ 550 °C are not completely dense. It is not uncommon for porosity to be entrapped in columnar films.

Figure 4.24 shows the permittivity as a function of deposition temperature for films deposited using the BZN-0.5 base composition. The maximum permittivity occurs at the maximum deposition temperature for all three of the targets used, as shown in Figure 4.24. The loss is less than 0.004 for all of the films. The films deposited at 450°C were amorphous and the films deposited at temperatures greater than 500 °C were crystalline. The x-ray diffraction patterns were shown previously in Figure 4.10 and Figure 4.12. The film grown at a substrate temperature of 500 °C using the BZN-0.5 + 0.15 mol Bi_2O_3 target shows a small amount of $BiNbO_4$ in the x-ray pattern in Figure 4.12. The other films are single phase cubic pyrochlore within the detection limits of the x-ray diffraction equipment that was used. The films grown using targets that have excess bismuth have maximum permittivities of 108 for the target with 0.15 moles Bi_2O_3 excess and 107 for the target with 0.03 moles Bi_2O_3 excess.

For all of the different compositions of BZN-1 and BZN-0.5, the loss tangent is less than 0.007. This is a strong indication that the films are ionically compensated and not electronically compensated for the bismuth and zinc deficiencies in the crystal structure. The losses in the films would be significantly higher if there were electronic species compensating the cation vacancies in the structure. This helps justify the choice of ionic compensation made in discussing the film compositions.

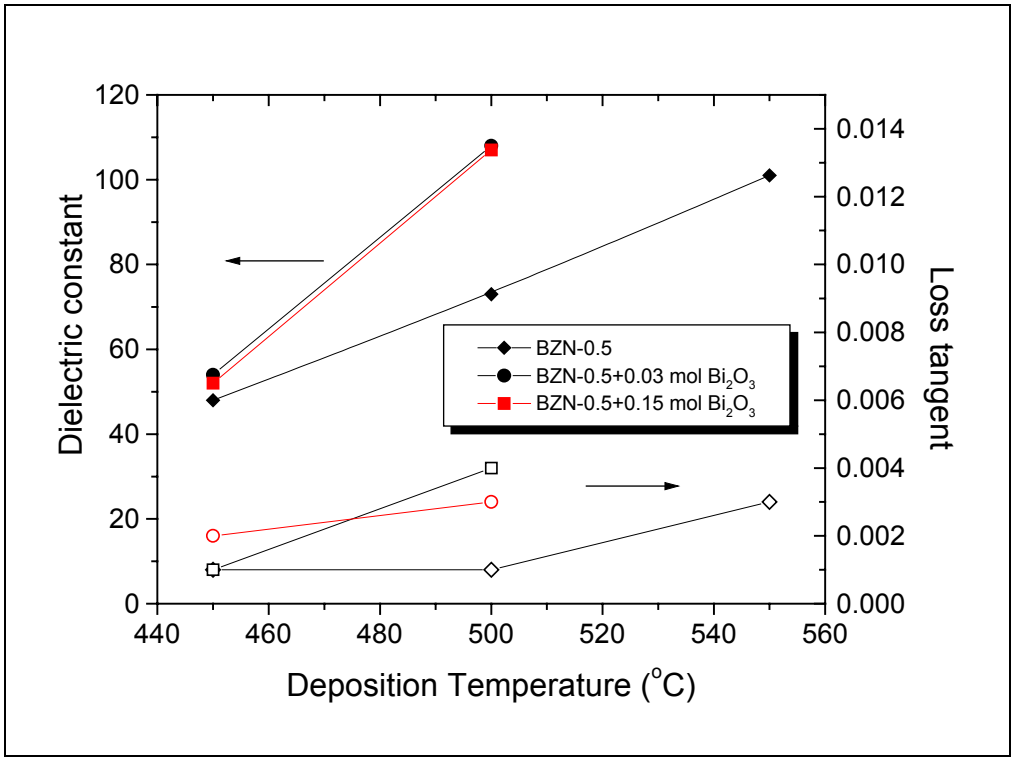

Figure 4.24 Permittivity as a function of deposition temperature for films deposited using targets with the base composition of BZN-0.5. The films were deposited at a target to substrate distance of 7 cm and a laser frequency of 3 Hz. The films deposited at 450 °C were deposited using a chamber pressure of 50 mTorr and the films deposited at 500 °C and 550 °C were deposited using a chamber pressure of 100 mTorr. The measurements were completed at room temperature using a frequency of 10 kHz and an oscillation voltage of 0.03 V.

4.4.2 Dielectric Properties as a Function of Chamber Pressure

Figure 4.25 shows the permittivity as a function of chamber pressure for films grown from the BZN-1 target, at a substrate temperature of 550 °C, a target to substrate distance of 7 cm, and a laser frequency of 3 Hz. The x-ray diffraction patterns for these films were given previously in Figure 4.7 and the film compositions were shown in Table 4.9. The films grown between 100 to 400 mTorr show the cubic pyrochlore structure. The bismuth and zinc contents dramatically increase as the chamber pressure increases from 100 to 400 mTorr. The bismuth and zinc contents were 1.39 moles and 0.64 moles,

respectively, at 100 mTorr and 1.69 moles and 0.90 moles, respectively, at 400 mTorr. The permittivity increased slightly as the chamber pressure increased and the loss tangent decreased with increasing chamber pressure. It is interesting that the changes in permittivity and loss are really rather small given the substantial range in composition. This suggests that there should be a wide processing window for vapor deposited BZN films.

The maximum permittivity of 138 occurs at a chamber pressure of 400 mTorr. This permittivity is approaching the bulk permittivity for BZN-1.0 of 150.[5] It would be interesting to explore higher temperature deposited films, as well as the film microstructure, to investigate the cause of the differences.

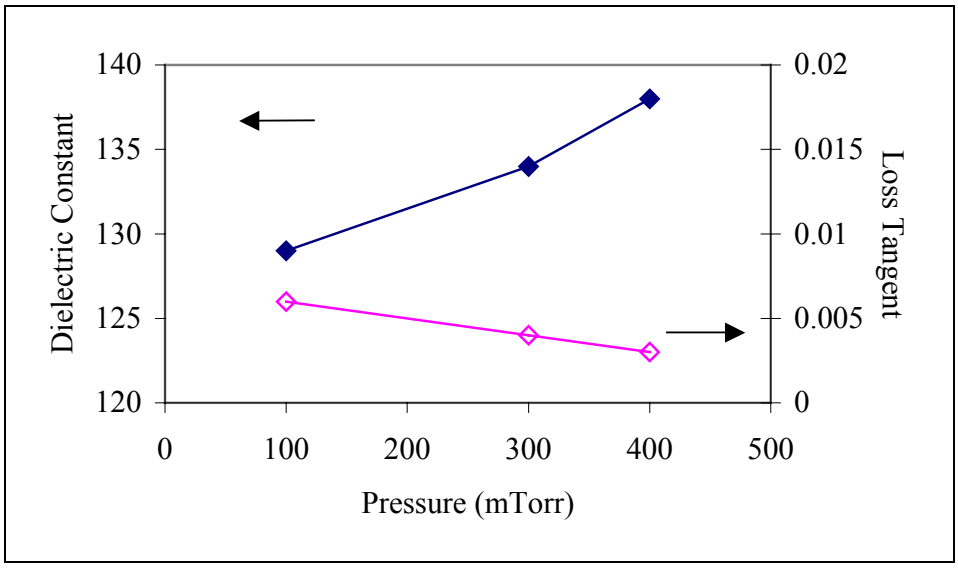

Figure 4.25 Permittivity as a function of chamber pressure for films grown from the BZN-1.0 target, at a substrate temperature of 550 °C, a target to substrate distance of 7 cm, and a laser frequency of 3 Hz. The measurements were completed at room temperature using a frequency of 10 kHz and an oscillation voltage of 0.03 V.

4.4.3 Permittivity as a Function of Target to Substrate Distance

Figure 4.26 shows the permittivity as a function of target to substrate distance for films grown using the BZN-1.0 + 0.15 mol Bi_2O_3 target, at a substrate temperature of 550 °C, a chamber pressure of 100 mTorr, and a laser frequency of 3 Hz. Table 4.4 showed the film compositions as a function of target to substrate distance for these films. The bismuth content changed from 1.30 moles to 1.55 moles at target to substrate distances of 5 cm and 7 cm, respectively. The zinc content remained approximately the same as a function of target to substrate distance. The permittivity changed from 125 to 132 at target to substrate distances of 5 cm and 7 cm, respectively. The increase in bismuth content in the films could be responsible for the increases in permittivity in the films.

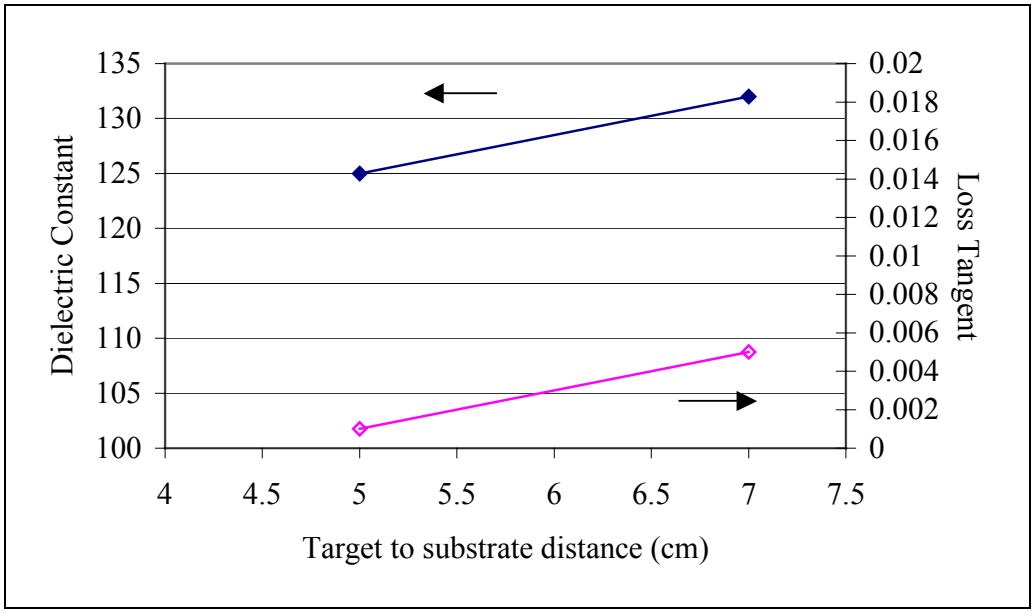

Figure 4.26 Permittivity as a function of target to substrate distance, for films grown using the BZN-1.0 + 0.15 mol Bi_2O_3 target, at a substrate temperature of 550 °C, a chamber pressure of 100 mTorr, and a laser frequency of 3 Hz. The measurements were completed at room temperature using a frequency of 10 kHz and an oscillation voltage of 0.03 V.

4.4.4 Temperature Coefficient of Capacitance

Because BZN films are interesting for NPO capacitors, it is also important to measure the temperature coefficient of capacitance, TCC. TCC was calculated using the following equation:

$$TCC = \frac{C' - C}{C\Delta T} \qquad (1)$$

where C' and C are the capacitance at 100 °C and –50 °C, respectively, and ΔT is the change in temperature. The TCC was measured at a frequency of 10 kHz and an oscillation voltage of 0.03V. The loss was less than 1 % over the temperature range of 100 °C to –50 °C. Figure 4.27 shows the dielectric constant as a function of deposition temperature over the temperature range used to calculate the TCC for films grown using the BZN-1.0 + 0.11 mol Bi_2O_3 target.

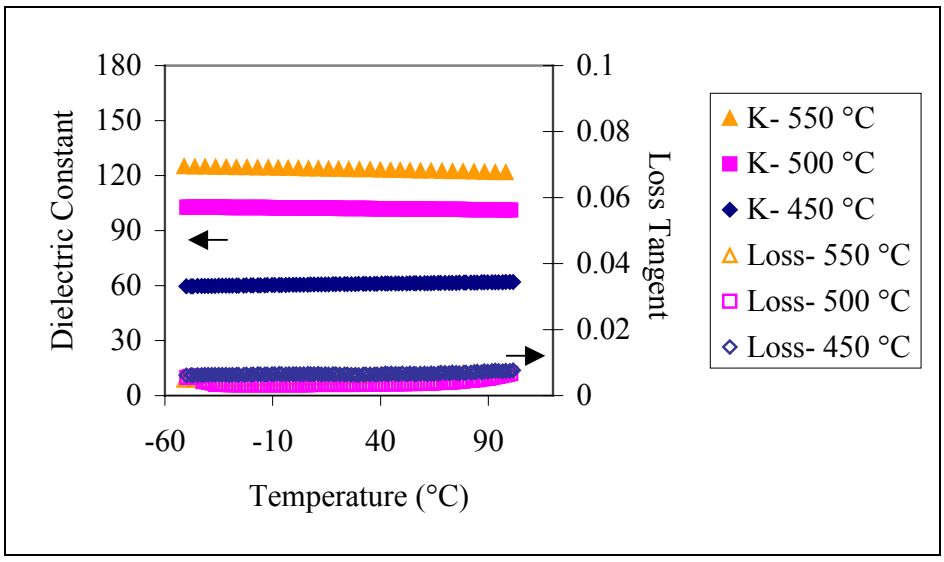

Figure 4.27 Temperature dependence of the dielectric constant for films grown using the BZN-1.0 + 0.11 mol Bi_2O_3 target, on Nova substrates, at different substrate temperatures, at a target to substrate distance of 7 cm, a laser frequency of 3 Hz, and a chamber pressure of 100 mTorr. The measurements were completed at a frequency of 10 kHz and an oscillation voltage of 0.03 V.

Figure 4.28 shows the summary of the TCC for films with the base composition of BZN-1.0 on Nova substrates. The films deposited at 450 °C are amorphous and the films deposited at temperatures above 500 °C are crystalline. The TCC ranges from positive 260 ppm/°C to 186 ppm/°C for the amorphous films to negative –94 ppm/°C to –200 ppm/°C for the crystalline films deposited at 550 °C. These results correspond to the TCC measurements of the MOD films (see Figure 2.14). The TCC of –400 ppm/°C is the value for BZN-1.0 bulk samples.[5] The TCC of only –200 ppm/°C could indicate that the films grown by PLD are not completely crystallized, or not single phase.

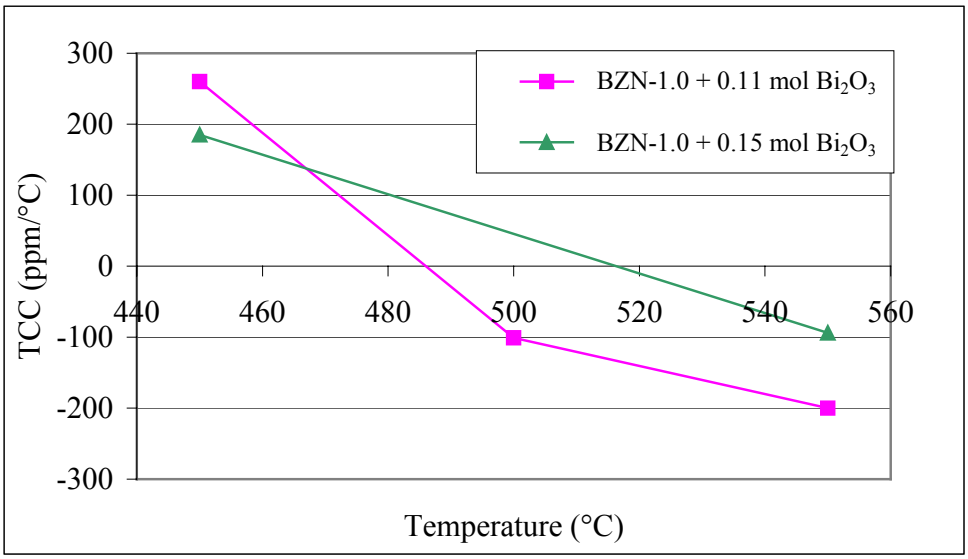

Figure 4.28 TCC as a function of deposition temperature for films deposited using the base target composition of BZN-1.0. The films were deposited on Nova substrates, at a target to substrate distance of 7 cm, and a laser frequency of 3 Hz. The film deposited at 450 °C using the BZN-1.0 + 0.15 mol target was deposited at a chamber pressure of 50 mTorr. The other films were deposited at a chamber pressure of 100 mTorr.

Figure 4.29 shows the summary of the TCC for films grown using the base target composition of BZN-0.5. The TCC ranges from positive 226 ppm/°C for the amorphous films deposited at 450 °C to –22 ppm/°C crystalline films deposited at 500 °C. The TCC

for the films deposited at 500°C are promising for NPO capacitors because of their low TCC values. The permittivities of these films are ~100.

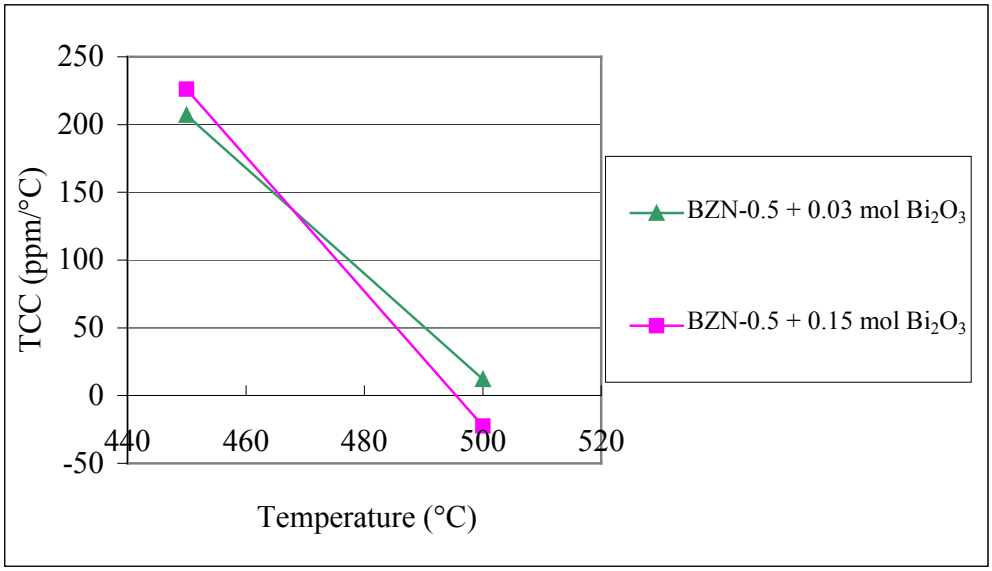

Figure 4.29 TCC as a function of deposition for films with a base composition of BZN-0.5. The films were deposited on Nova substrates, at a target to substrate distance of 7 cm, a laser frequency of 3 Hz, and a chamber pressure of 100 mTorr.

4.4.5 Low Temperature Dielectric Behavior for Amorphous Films

The dielectric behavior at low temperature for amorphous films of BZN was never measured in previous studies.[6,43] The ability to process amorphous films at temperature less than 450 °C makes it possible to use these films for on chip applications. Figure 4.30 shows the dielectric constant as a function of temperature for an amorphous film grown on the 1st Pt/ La, Pt alloy (5 vol % La in Pt)/ $La_2O_3/SiO_2/Si$ wafer, using the BZN-1 + 0.15 mol Bi_2O_3 target, at a deposition temperature of 450 °C, a target to substrate distance of 7 cm, a laser frequency of 3 Hz, and a chamber pressure of 100 mTorr. The amorphous film shows a knee in the permittivity and a peak in the loss tangent at ~50 K. The film might have small regions of crystalline material that cause

this behavior. Future studies using TEM need to be completed to determine this. The slope change is weakly frequency dependent, unlike the relaxation observed in BZN-1 films and in bulk samples.[6,36] The loss remains less than 0.01 over the entire temperature range. This is in contrast to the dramatic increase in the loss which is shown in Figure 2.9 and Figure 2.15 for bulk BZN-1 and MOD films, respectively. It is also intriguing that the TCC does not become negative above the knee.

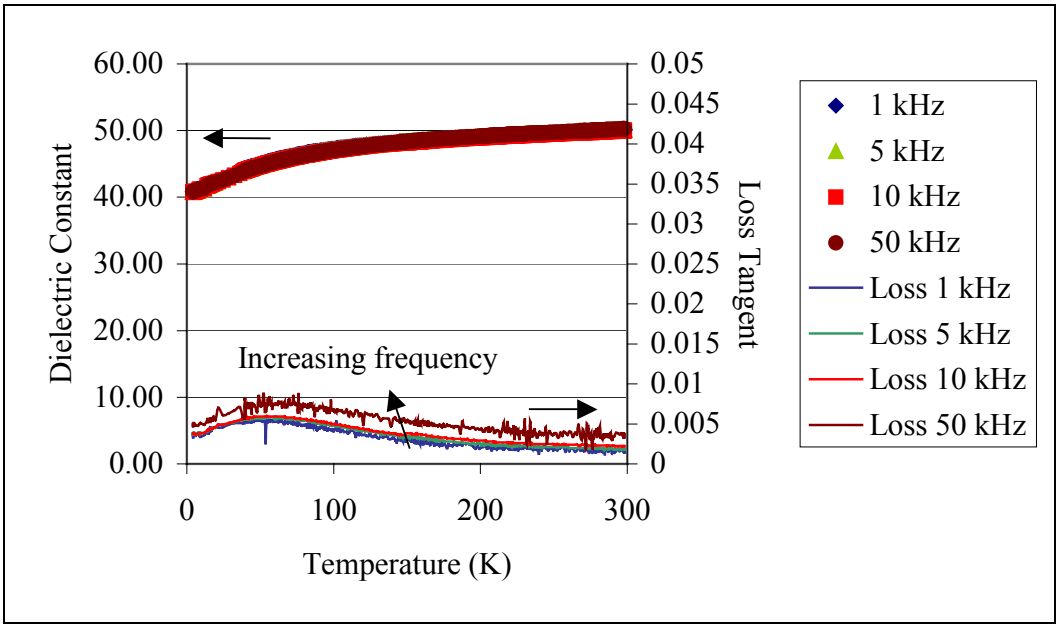

Figure 4.30 Dielectric constant as a function of temperature for a film deposited using the BZN-1 + 0.15 mol Bi_2O_3 target, on the 1st Pt/ La, Pt alloy (5 vol % La in Pt)/ $La_2O_3/SiO_2/Si$ wafer, at a deposition temperature of 450 °C, a target to substrate distance of 7 cm, a laser frequency of 3 Hz, and a chamber pressure of 100 mTorr.

4.4.6 Leakage Behavior for Amorphous Films

A preliminary study of the leakage current behavior of the PLD films was completed. Figure 4.31 shows the leakage current as a function of time that the voltage was applied for a positive and negative bias on a film grown using the BZN-1.0 + 0.15 mol Bi_2O_3 target, on the 1st Pt/ La, Pt alloy (5 vol % La in Pt)/ $La_2O_3/SiO_2/Si$ wafer, and a deposition temperature of 450 °C. The film is amorphous under these deposition

conditions. I-V curves are strongly time dependent, so it is very important to determine the leakage current as a function of time.[64] The leakage in the capacitor reached steady state behavior at times greater than ~90 seconds under these bias conditions. Higher voltages led to dielectric breakdown.

Figure 4.32 shows the leakage behavior as a function of electric field measured 90 seconds after increasing the electric field on the sample. The data shows that the leakage behavior is the same for positive and negative biases on the top electrode. This result is different from crystalline MOD films with Cr/Au top electrodes and the BZN-1.0 composition. The MOD films show an order of magnitude higher leakage current when the top electrode has a negative bias verses a positive bias on the top electrode.[43] The PLD film shows lower leakage currents than the MOD films with Cr/Au electrodes with values of 2×10^{-8} A/cm^2 and 1×10^{-6} A/cm^2, respectively at a 200 kV/cm.[43] The lower leakage values for the PLD films could be caused by several different factors. First, the PLD films measured are amorphous films, and the MOD films are crystalline. There maybe more structural defects associated with the crystalline MOD films that lead to higher leakage currents. Second, the composition of the MOD films is $Bi_{1.5}Zn_{1.0}Nb_{1.5}O_7$ versus the PLD film composition of $Bi_{1.42}Zn_{0.50}Nb_{1.5}O_{6.38}$. More extensive studies on the leakage behavior as a function of crystallinity and composition would be needed to determine cause of the lower leakage currents in PLD films verses MOD films.

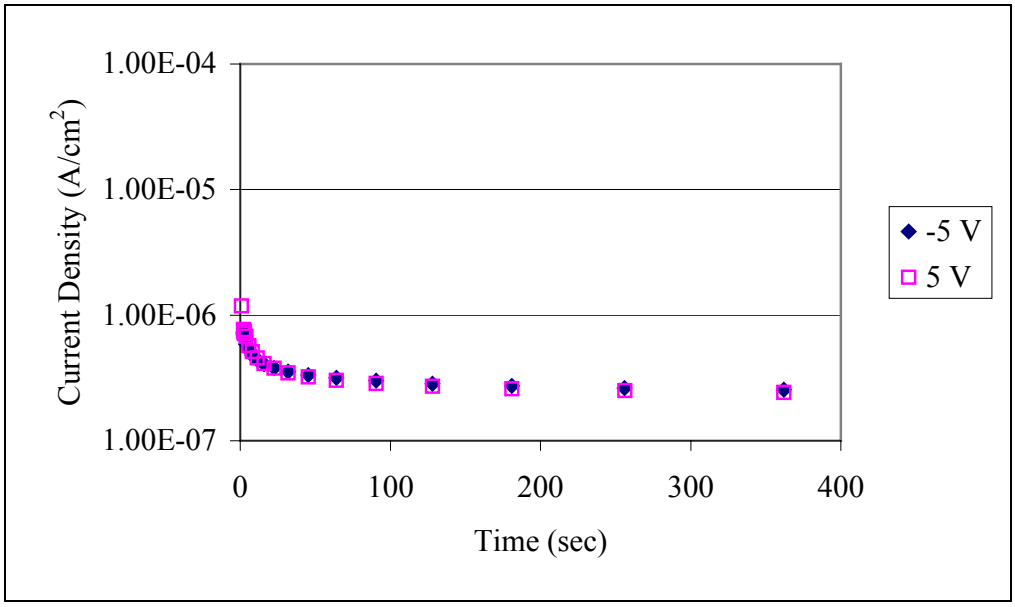

Figure 4.31 Leakage current as a function of time for positive and negative bias on a film grown using the BZN-1.0 + 0.15 mol Bi_2O_3 target, on the 1st Pt/ La, Pt alloy (5 vol % La in Pt)/ $La_2O_3/SiO_2/Si$ wafer, at a deposition temperature of 450 °C, at a target to substrate distance of 7 cm, a laser frequency of 3 Hz, and a chamber pressure of 100 mTorr.

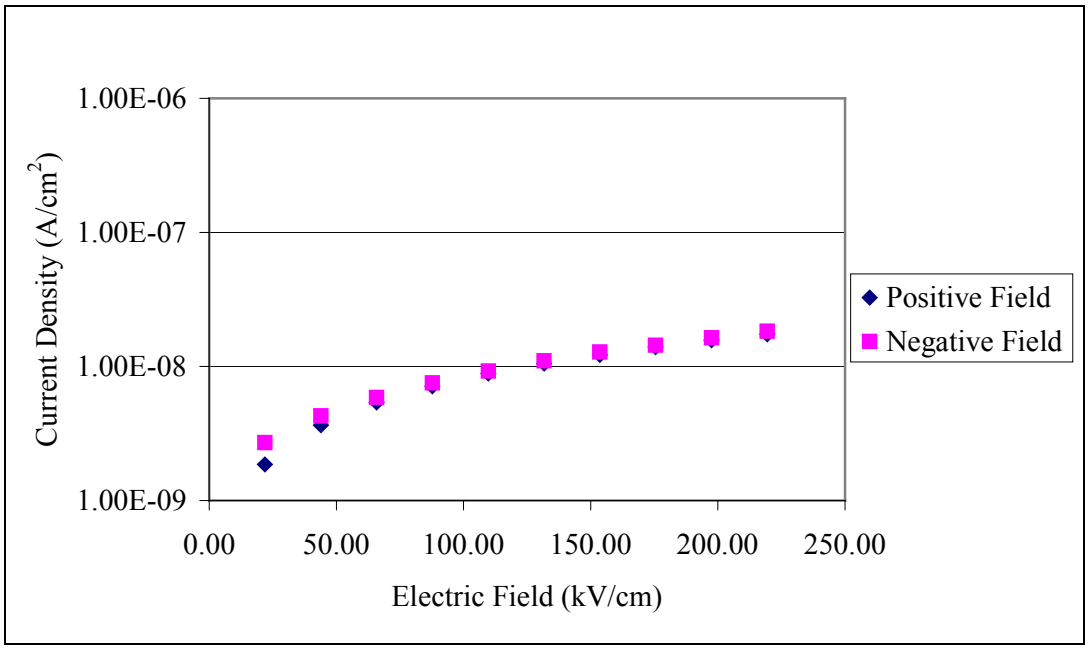

Figure 4.32 Leakage current as a function of electric field for positive and negative fields for a film grown using the BZN-1.0 + 0.15 mol Bi_2O_3 target, on the 1st Pt/ La, Pt alloy (5 vol % La in Pt)/ $La_2O_3/SiO_2/Si$ wafer, at a deposition temperature of 450 °C, at a target to substrate distance of 7 cm, a laser frequency of 3 Hz, and a chamber pressure of 100 mTorr. Leakage currents were measured 90 seconds after increasing the field.

4.4.7 Tunability

One area of interest for BZN thin films is for tunable applications. The tunability of BZN thin films was measured by applying a field from 0 V to a positive electric field and then going from the positive electric field back to 0 V and then applying a negative electric field and going back to 0 V. The sample was typically cycled twice under these conditions. Several electrodes were tested to determine the maximum bias field that could be applied to the sample before dielectric breakdown occurred. All six compositions of BZN-1.0 and BZN-0.5 showed similar tunability curves. Figure 4.33 shows the tunability as a function of deposition temperature for film deposited using the BZN-1.0 + 0.11 mol Bi_2O_3 target. The film deposited at 450 °C was amorphous and the films deposited at temperatures greater than 500 °C were crystalline. The films deposited at 450 °C and 500 °C show constant permittivities as a function of electric field over the field range tested. The loss tangent on both of these films increases with the bias field, indicating the beginning of conduction in the film, which would eventually lead to dielectric breakdown in the capacitors.

The lack of tunability in the films fired at 500 °C and 450 °C is similar to the results on the MOD BZN-1.0 films. In that case, as well, films fired at 550 °C showed very little tunability in the dielectric constant as a function of electric field.[6] The amount of tunability increased as the firing temperature increased in the MOD films.[6] The PLD film deposited at 550 °C showed a dielectric constant change of 5.4 % at an electric field of 400 kV/cm. MOD films fired at 750 °C showed much larger tunabilities of the dielectric constant ~30 % at 1.8 MV/cm.[43] The results on the MOD films clearly indicate that the crystallization of the films is a critical parameter to having large changes in the

dielectric constant as a function the electric field. One possibility is that the lower tunability of the PLD films deposited at lower temperatures could indicate the films are not completely crystallized or contain second phase not apparent in the x-ray diffraction patterns. This would be consistent with the lower dielectric constants, lower tunability, and positive TCC values. TEM studies are needed to confirm this hypothesis. Another possibility in the tunability differences are the variations in stoichiometry between the PLD films and the MOD films, which was previously discussed in section 4.2.

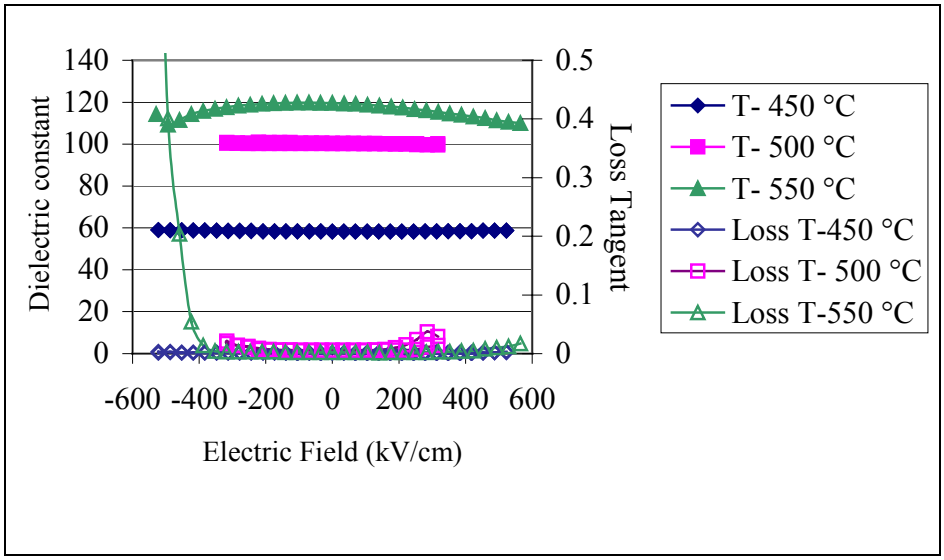

Figure 4.33 Dielectric constant as a function of electric field for films deposited using the BZN-1.0 + 0.11 mol Bi_2O_3 target, on Nova substrates, at a target to substrate distance of 7 cm, a laser frequency of 3 Hz, and a chamber pressure of 100 mTorr. Note, the film deposited at 550 °C was only cycled once as a function of electric field. The other films were cycled twice.

4.4.8 Effects of Forming Gas Annealing on Dielectric Properties

A preliminary study was completed to determine if BZN films would be stable in a forming gas environment. A capacitor that is integrated on silicon would have to undergo several different forming gas anneals during the device fabrication.[65] The effects on the BZN films during forming gas annealing were completed in an ambient of

5% hydrogen and 95% nitrogen at atmospheric pressure. The film was held at 400 °C for 30 minutes under this atmosphere. The forming gas annealing was completed on a film that had platinum top electrodes, because the Cr/Au electrodes were not stable at 400 °C. Figure 4.34 shows the x-ray diffraction patterns before and after the forming gas anneal. The film was well crystallized into the cubic pyrochlore structure before the forming gas anneal and after the forming gas anneal the film is poorly crystallized. Changes in the crystal structures were also observed in $SrBi_2Ta_2O_9$ (SBT) and $Bi_{3.25}La_{.75}Ti_3O_{12}$ (BLT) under forming gas annealing.[65,66] The SBT films observed the formation of a secondary phase of Bi_2O_3 and the BLT films observed the formation of Ti_6O_{11} and $(Bi,La)_2Ti_2O_7$.[65,66]

Table 4.10 shows the effects of the forming gas annealing on the dielectric properties. After under going the forming gas annealing, the dielectric constant decreased by 10 % and the tan δ increased. This type of degradation was also observed in ferroelectric capacitors.[65] This may indicate either that the hydrogen is incorporated into the film, or that the film is being reduced. Future studies would need to be completed to analyze the structural and compositional changes of the BZN films during forming gas annealing. These results do, however, suggest that BZN capacitors may need to be protected by a barrier layer during forming gas annealing for on-chip applications.

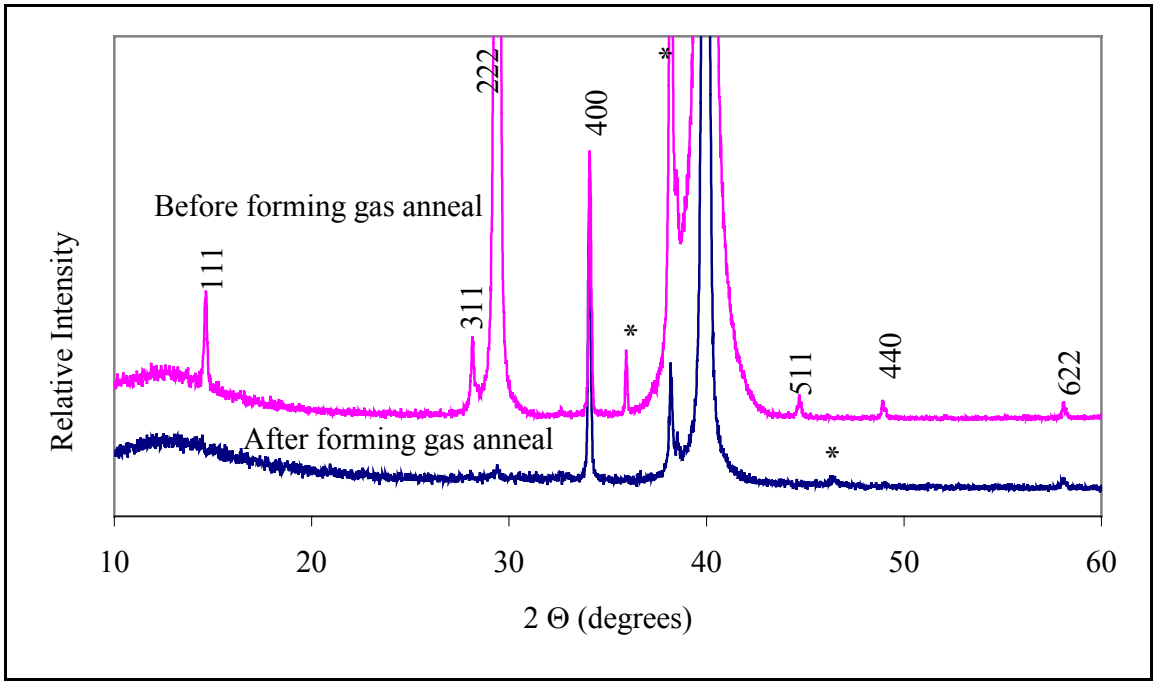

Figure 4.34 X-ray diffraction patterns before and after forming gas anneal on a film grown using the BZN-1.0 target, on Nova substrates, at a substrate temperature of 650 °C, a target to substrate distance of 7 cm, a laser frequency of 10 Hz, and a chamber pressure of 200 mTorr. * denotes substrate peaks. The amorphous hump around 12° 2θ is from the substrate holder. Indexed peaks from the cubic pyrochlore phase.

Table 4.10 Dielectric properties before and after forming gas annealing.

Before forming gas anneal		After forming gas anneal	
K	Tan δ	K	Tan δ
127	0.001	115	0.022

4.5 Degradation Behavior of BZN Thin Films

Highly accelerated lifetime testing, HALT, was completed on amorphous BZN thin films to determine both the degradation mechanisms for failure under constant dc field and the lifetime of BZN thin films. Experiments were completed on 23 capacitors under each set of conditions. The PLD samples were produced individually and it was

possible to get 1 or 2 HALT samples from each film. It would have been ideal to grow one sample by PLD and use the same film for all of the HALT tests, but the heater used in the PLD chamber is limited to samples that are ~2.5 cm x 2.5 cm. Moreover, PLD is limited in the areas of uniform thickness that can be produced. The likely result of this method adopted is that there may be some run-to-run variability in the films, and hence the HALT data.

The samples for the HALT analysis were grown from the BZN-1.0 + 0.15 mol Bi_2O_3 target, on the1st Pt/ La, Pt alloy (5 vol % La in Pt)/ $La_2O_3/SiO_2/Si$ wafers, at a deposition temperature of 450 °C, a target to substrate distance of 7 cm, a laser frequency of 3 Hz, and a chamber pressure of 100 mTorr. The films were amorphous under these growth conditions.

Initially, all of the samples were processed together for the patterning of the top electrodes to eliminate any deviation in the processing of the samples, but there were not enough samples to complete the tests processed in the first batch. There were five different batches of samples processed for the patterning of the top electrodes for the HALT samples. Again, this variation in processing may have led to variation in the degradation of the samples.

In this study, the time to failure was determined to be the time when the current reached 10^{-4} A. Figure 4.35 shows the time to failure for two capacitors.

The following empirical relationship was used to determine the time to failure at any voltage and temperature:

$$\frac{t_1}{t_2} = \left(\frac{V_2}{V_1}\right)^n \exp\left[\frac{E_a}{k}\left(\frac{1}{T_1} - \frac{1}{T_2}\right)\right] \qquad (4.2)$$

where t_1 is the mean time to failure at V_1 and T_1, t_2 is the mean time to failure at V_2 and T_2, V_1 and V_2 are the test voltages, n is the voltage acceleration factor, E_a is the activation energy, k is Boltzmann's constant, and T_1 and T_2 are the test temperatures in K.[67]

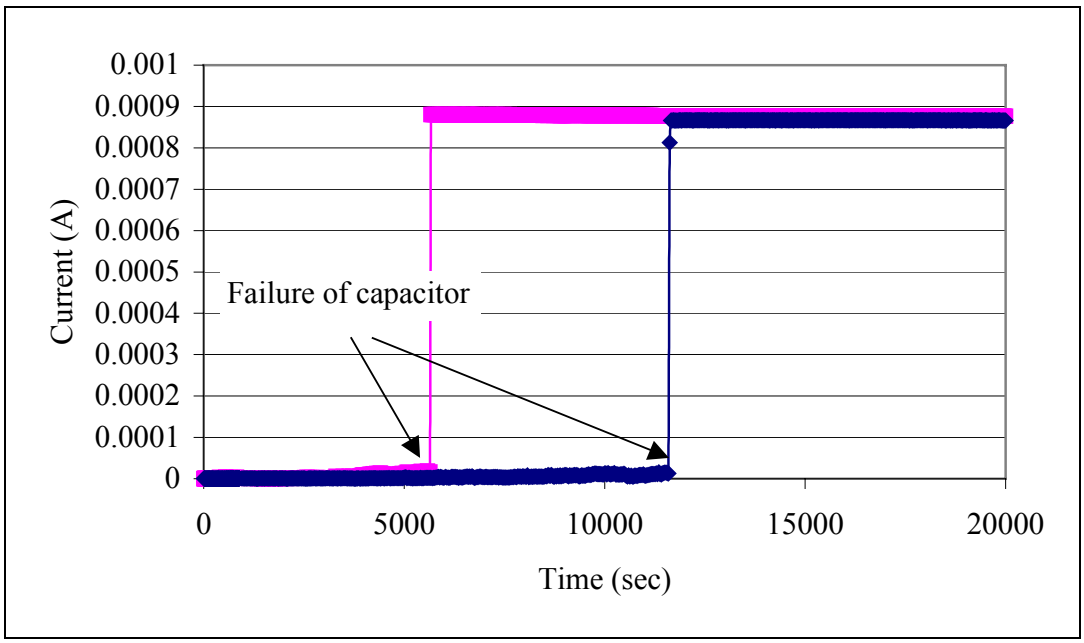

Figure 4.35 Current as a function of time, illustrating the failure of the capacitors.

The log of the failure time was plotted as a function of the cumulative percent failure, cpf, to determine the mean time to failure for a set of test conditions. The method for fitting the data is given in the Appendix. Figure 4.36 shows the time to failure as a function of the cumulative percent failure. The curve in Figure 4.36 shows an S-shaped curve, which indicates that there are two modes of failures for the breakdown of the samples.[68] The lower portion of the curve is associated with freak failures, which are typically a result of processing defects. The upper portion of the curve is used to determine the median time to failure, MTF, and the standard deviation of the data. One of the problems with the HALT was there were several modes of failure in the upper portion of the curve under some of the HALT conditions. Figure 4.37 shows the HALT

data combined from two tests, on 46 capacitors, at 85 °C and 10 V. The upper portion of the curve shows three different slopes to the curve. The middle region was used to calculate the MTF for this set of data. These variations in the data lead to the scatter in the σ_{ln} values. Some data from the tests could not be fit to curves to calculate the MTF. There was too much scatter in two tests at 7 V and 100 °C to fit the data. Because of the variability, further testing was not completed to determine the voltage acceleration factor.

Table 4.11 shows the summary of results for HALT for PLD films. The results show that there is variation in the standard deviation of the natural logarithm of the failure times, σ_{ln}. The σ_{ln} should be independent of all external stresses for proper lifetime assessment to be completed.[69] These HALT show that there are large variations in the degradation behavior between each sample that causes the variation in the standard deviation of the failures times.

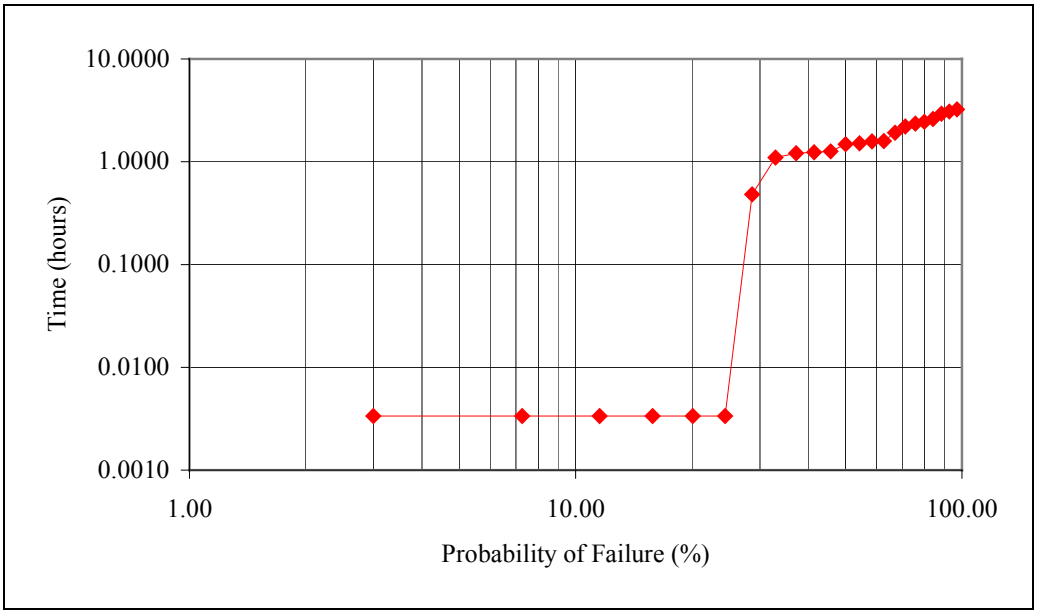

Figure 4.36 The time to failure as a function of the cumulative probability of failure for HALT conditions of 100 °C and a voltage of 10 V.

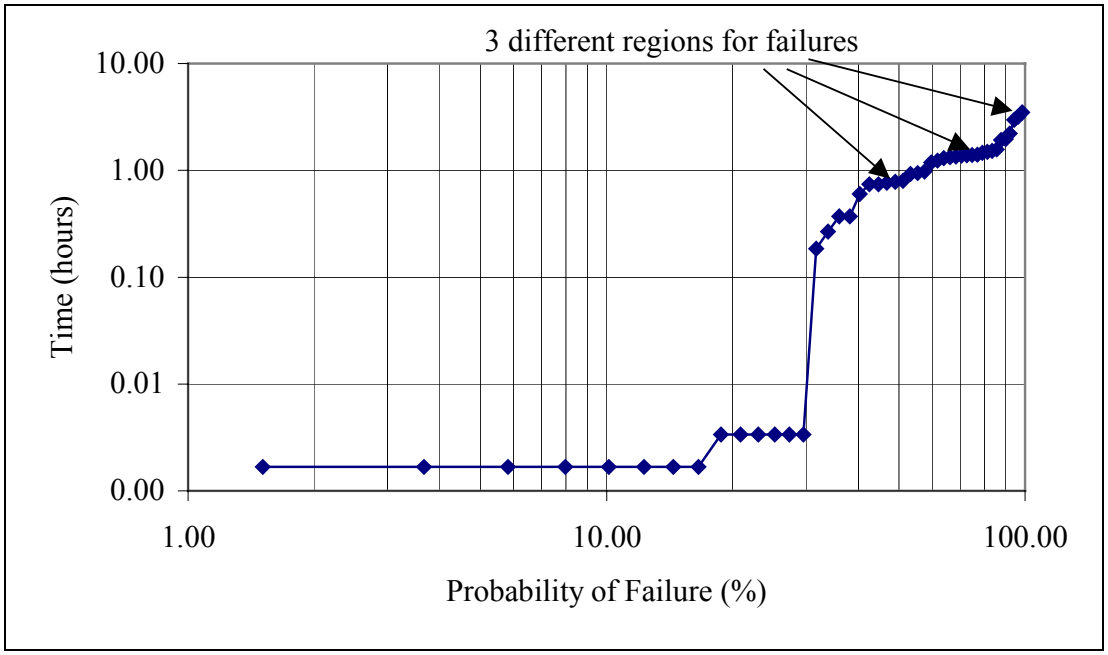

Figure 4.37 The time to failure as a function of the cumulative probability of failure for two samples tested at 85 °C and 10 V.

The summary of the results of the HALT for PLD films shows large variation in the MTF and inconsistencies in the results. The sample tested at 85 °C should have had a longer mean time to failure than the sample tested at 100 °C.

Table 4.11 Results of the HALT for PLD films.

Temperature (°C)	Voltage (V)	MTF (hours)	σ_{ln}
85	10	1.25	0.267
100	10	1.82	0.674
115	10	0.26	0.704
125	10	0.21	0.282

Note: The test completed at 85 °C is for two HALT runs.

The MTF was fitted to an Arrhenius plot to determine the activation energy. Figure 4.38 shows the MTF as a function of 1/Temperature. The slope of this line was

multiplied by Boltzmann's constant to calculate the activation energy. The activation energy was 0.66 ± 0.49 eV. The bounds were calculated by systematically removing one point from the data and recalculating the slope. This activation energy is lower than the $BaTiO_3$ multilayer ceramics, which typically have an activation energy of 1.1 eV.[48] There is some work on the activation energy for oxygen ion conduction in bulk pyrochlore materials. $Nd_2Zr_2O_7$ had experimentally measured activation energy of 0.76-0.84 eV and $Sm_2Zr_2O_7$ had experimentally measured activation energy of 0.69 eV.[70] Both of these materials have similar activation energies to the BZN thin films.

More HALT runs need to be completed before statistically significant results can be produced and recommendations will be made in the future work section.

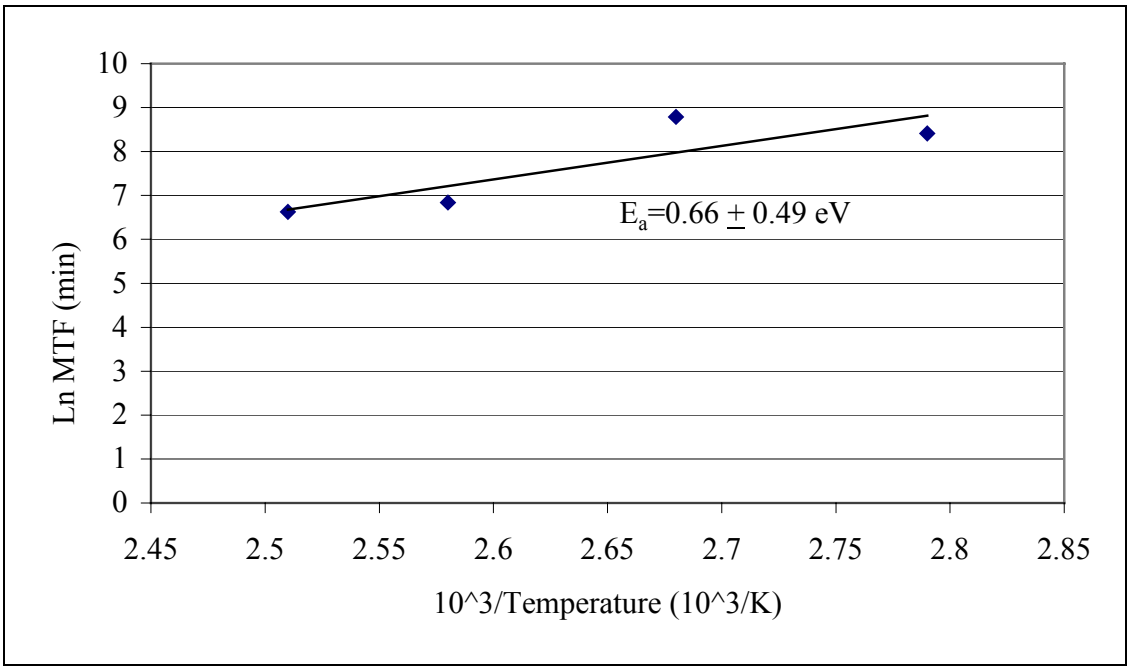

Figure 4.38 The MTF as a function of 1/Temperature.

Chapter 5 Conclusions and Future Work

5.1 Conclusions

Bismuth-zinc-niobate, BZN, thin films were deposited using pulsed laser deposition. The relationships between processing and properties were studied. This thesis specifically looked at the effects of target to substrate distance, laser frequency, target composition, chamber pressure, and deposition temperature and their effects on the film composition. It was found that composition control in the bismuth pyrochlores is very complicated in the PLD process, due to the complex interplay between deposition variables and the large apparent solubility limits in the pyrochlore structure. It can be concluded that laser frequencies between 3 to 10 Hz and deposition temperatures between 450 °C to 600 °C did not impact the BZN film composition. The lack of volatilization at these temperatures is a mixed blessing. On the positive side, it at least eliminates one processing variable. It did, however, preclude the use of self-accommodation of stoichiometry, as is often used in the growth of GaAs or the Pb-based perovskites.[51] In those systems, providing there is a considerable overpressure of the volatile species, the incorporation of that species into the growing film self-regulates to produce near stoichiometric films over a wide range of overpressures. It would be interesting to explore whether a similar approach could be used with higher deposition temperatures for the pyrochlores, where volatility would be expected to increase. However, it was clear that at the low substrate temperatures used in this study, this approach could not be used.

The target to substrate distance and the chamber pressure were the dominant parameters that controlled the stoichiometry of the BZN films. By decreasing the target to substrate distance from 7 cm to 4 cm, the bismuth content in the films was decreased,

while the zinc composition remained unchanged. The decrease in bismuth content was probably caused by resputtering of the bismuth from the growing film.

Changing the chamber pressure from 100 mTorr to 400 mTorr dramatically changed the film composition and increased both the bismuth and zinc content in the film to a composition that was close to the stoichiometry of the target. It was suggested that the angular distribution of species in the plume varied, with the lighter species being scattered preferentially to the outer region of the plume and the heavier elements having narrower distributions along the deposition axis. Ultimately, it is believed that the interplay of the distribution of elements within the plume, bombardment, and the narrowing of the plume with increasing pressure controls the film composition over the deposition space investigated in this study.

The crystallization of the cubic pyrochlore structure varied as a function of chamber pressure and substrate. The minimum crystallization temperature was 450 °C onto Pt/ La, Pt alloy (5 vol % La in Pt)/ $La_2O_3/SiO_2/Si$ wafers. This is lower than any of the previous studies on BZN thin films and makes BZN a candidate material for on chip decoupling capacitors. The crystallization temperature changed from 450 °C to 500 °C depending on the crystallinity of the Pt/ La, Pt alloy (5 vol % La in Pt)/ $La_2O_3/SiO_2/Si$ wafers. The origin of this change in crystallization temperature for the cubic BZN films is currently unknown and will be discussed more extensively in the future work section. The lattice parameter for the films grown in this study was smaller than bulk BZN and MOD BZN films.

The amorphous films show a small knee in the permittivity as a function of temperature measured from 300 K to 4 K and peak in the loss at ~50 K. The loss

remained less than 0.01 at 50 kHz over the entire temperature range. The amorphous PLD films showed low leakage currents of 2 x 10^{-8} A/cm^2 at 200 kV/cm with Cr/Au top electrodes.

The dielectric constant varied between 50 and 138 as a function of deposition temperature and film composition. The dielectric loss was ≤ 0.007 for all of the films measured at 10 kHz. Figure 5.1 shows a comparison of the dielectric properties of the films grown by PLD in this study with the previous work on BZN by MOD. The PLD films show properties comparable to those of MOD BZN-1 films crystallized ~150°C higher. This may due to a combination of lower crystallization temperatures and reduction in the film zinc content. This work showed that using PLD it was possible to crystallize cubic BZN at 450 °C, which was 100 °C lower than the crystallization temperature for MOD films.

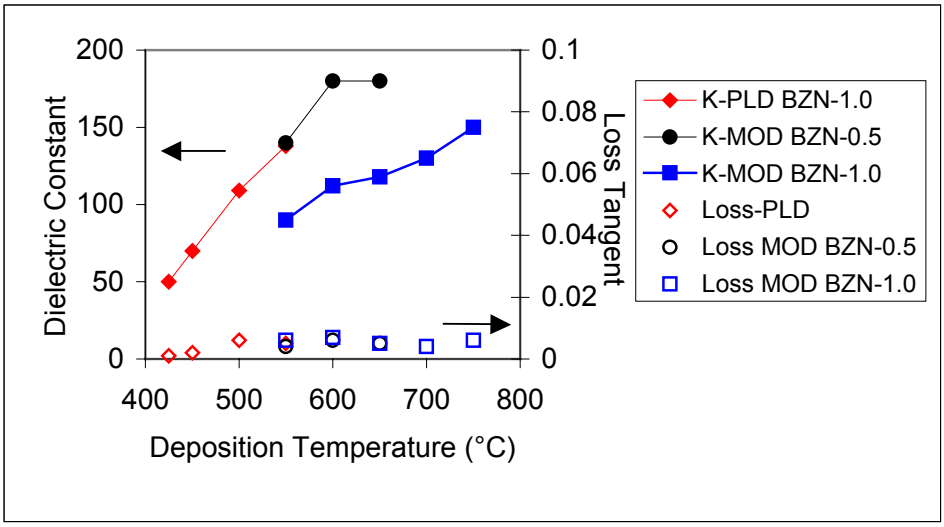

Figure 5.1 Summary of dielectric properties for PLD films and MOD films.[6,43]

Both the PLD and MOD films show low dielectric loss. This low dielectric loss is a strong indication that any cation vacancies in the structure of the PLD films are

ionically compensated and not electronically compensated. If the films were electronically compensated, the dielectric loss should be significantly higher. The dielectric loss was independent of the stoichiometry of the films.

The temperature coefficient of capacitance, TCC, was strongly dependent on the crystallinity of the films and ranged between 200 ppm/°C to –200 ppm/°C for amorphous films and well crystallized films, respectively, when measured between 100 °C to –50 °C. The loss was $\leq$ 1 % over the temperature range measured for TCC. Some of the films (ε_r~100) showed TCC between 12 ppm/°C to –22 ppm/°C, which make them promising for NPO, negative, positive, but almost zero temperature coefficient of capacitance, dielectrics. These materials should be useful for high capacitance density, temperature and frequency stable capacitors for on and off chip applications.

5.2 Future Work

There are several different areas for future work on BZN thin films. They can be broken into six main areas: determining the angular distribution of species in the plasma plume, understanding the crystal structure of BZN thin films, lowering the deposition temperature, decoupling the roles of bombardment and composition, completing dielectric property measurements, and investigating epitaxial growth of BZN thin films.

In order to substantiate the species distribution model developed in this work, it would be necessary to confirm the angular distribution of species inside the plasma plume. This could be completed using optical spectroscopy or laser fluorescence. Both of these techniques could determine the species present inside the plasma plume and the distribution of energies of the species. In addition, the film composition should be

measured as a function of different positions of the substrate relative to the deposition axis to further analyze the angular distribution for the BZN system. This information could be used to advance the understanding of the compositional changes observed as a function of chamber pressure and target to substrate distance and produce a quantitative model for the ablation of BZN.

Complete studies using transmission electron microscopy, TEM, as a function of film deposition temperature are needed to determine the local distribution of amorphous and crystalline material. XRD is an averaging technique that establishes when at least part of the film crystallizes. Thus, it would be important to do TEM studies on the x-ray amorphous films to determine if the films have microcrystalline regions. Similarly, it should be determined if the crystalline films have regions of amorphous phases or secondary phases that could not be detected by x-ray diffraction. It would also be very interesting to complete high resolution TEM and neutron diffraction studies on the films as a function of composition and determine the positions of each of the cations in the crystal structure. Such studies would help resolve the dependence of permittivity, tunability, dielectric relaxation, and TCC on the composition and deposition temperature in both MOD and PLD BZN films. TEM studies would also be very useful in studying the interface between the film and the different substrates used in these studies. This would help determine if there were reactions occurring at the interfaces or if different nucleation mechanisms are occurring for different bottom electrode-dielectric interfaces.

It would also be interesting to attempt to lower the deposition temperature further by using substrates with lattice parameters that match the cubic BZN lattice parameter or attempt to use a seed layer to help facilitate the nucleation of BZN. Another method to

lower the deposition temperature would be to try ion-assisted deposition. Ion-assisted deposition has been previously used in the deposition of other materials by PLD to reduce the deposition temperature needed to grow single crystal films.[9]

It was impossible in this study to decouple the effects of composition and bombardment on the growth of BZN. It would useful to try to grow films under constant bombardment conditions and change the composition by batching new targets. The bombardment of the film could also be changed by using different gases during deposition. These studies would be able to determine if the bombardment or the changes in composition control the lattice parameter of the films. It would also be used to complete studies to determine how large of a bias the substrate acquires during deposition. As this could be a strong function of whether or not the sample was in the plume, measurements should be made on the potential as a function of target to substrate distance. This would be useful to determine if it is the bombardment of charged species that controls the composition during growth.

It would be interesting to map out the effects of composition and crystallinity on the dielectric relaxation in BZN thin films. It is possible to prepare films of a wide variety of stoichiometries by PLD that have not been previously investigated in bulk samples or in thin films. This offers the opportunity to determine how strongly tied the relaxation is to the cation stoichiometry. The mapping would also lead to determining the compositions that have the highest permittivities.

More studies need to be done to completely determine the degradation and reliability of BZN thin film. Larger batches of samples need to be tested to get more statistically significant results using HALT and to determine if there are several different

mechanisms that are responsible for degradation of BZN thin films. Since it is possible to produce a wide variety of compositions by PLD, it would be interesting to determine if the degradation and reliability of BZN thin films are strongly dependent on the stoichiometry of the film.

The tunability in the BZN-2/3 composition may be controlled by the zinc atoms, which are along the a-axis in the structure, having two possible crystallographic positions. It would be fascinating to try to grow epitaxial BZN-2/3 with the a-axis perpendicular to the substrate and measure out-of-plane tunability of the film. If the tunability is controlled by the zinc atoms, the epitaxial films should show larger tunabilities then the polycrystalline films have shown.

Appendix

The reliability of a device is defined in statistical terms as the probability of survival of the device over a given period of time while operating in a known set of conditions.[69] The reliability function can be defined using the following equation:

$$R(t)=1-F(t) \qquad (A.1)$$

where F(t) is the cumulative failure distribution function.

The failure rates of capacitors are not constant in time and are typically fitted to a lognormal distribution, $f_{ln}(t)$ or a Weibull distribution $f_w(t)$ density function.[69] This study use the lognormal distribution function, which is given by:

$$f_{ln}(t) = \frac{1}{\sqrt{2\pi\sigma_{ln}^2 t}} \exp\left[-0.5\left(\frac{\ln t - \ln t_{50}}{\sigma_{ln}} \right)^2 \right] \qquad (A.2)$$

where σ_{ln} is the standard deviation of ln t and t_{50} is the median lifetime at which 50 % of the devices fail.

The method used to determine the σ_{ln} and the t_{50} was a graphical method. The data for the time of failure was ranked from 1 to n, where n is the samples size. The cumulative failure distribution function (CDF), was determined using the following equation:

$$F_i(t) = \frac{i - 0.3}{n + 0.4} \qquad (A.3)$$

where i is the rank order and n is the total number of samples tested.[71] The mean time to failure, MTF, could be determined directly from the graph at the 50th percentile.

The standard deviation is calculated using the following equation:

$$\sigma_{ln} = 0.5 \ln\left(\frac{t_{84}}{t_{16}}\right) \qquad (A.4)$$

where t_{84} and t_{16} are the time to failure for 84 % and 16 % of the samples, respectively. The values of 16 and 84 are chosen because they are one standard deviation away from t_{50}.[71]

Some of the data in this study showed an S-shape to the distribution of failures and a different approach was used to determine the MTF and the standard deviation. The curve is broken into two section where the first failures are designated freak failures, fr, and the second section is designated, long failures, lf. The following equation is used to calculate the cumulative distribution function:

$$F(t)_{meas} = p*F_{fr}(t) + (1-p)*F_{lf}(t) \qquad (A.5)$$

where p is the probability of failure, F_{fr} (t) and F_{lf}(t) are the actual failure probabilities for modes fr and lf, respectively. The value of p is taken as the inflection point between the failure modes. F_{lf} was calculated using the equation A.4, where the F_{fr}(t) equaled one. The calculated values of F_{lf} were used to determine the MTF and σ_{ln}. σ_{ln} was calculated using equation A.3. Figure A.1 shows an example of the graphical method used to determine the MTF and σ_{ln}.

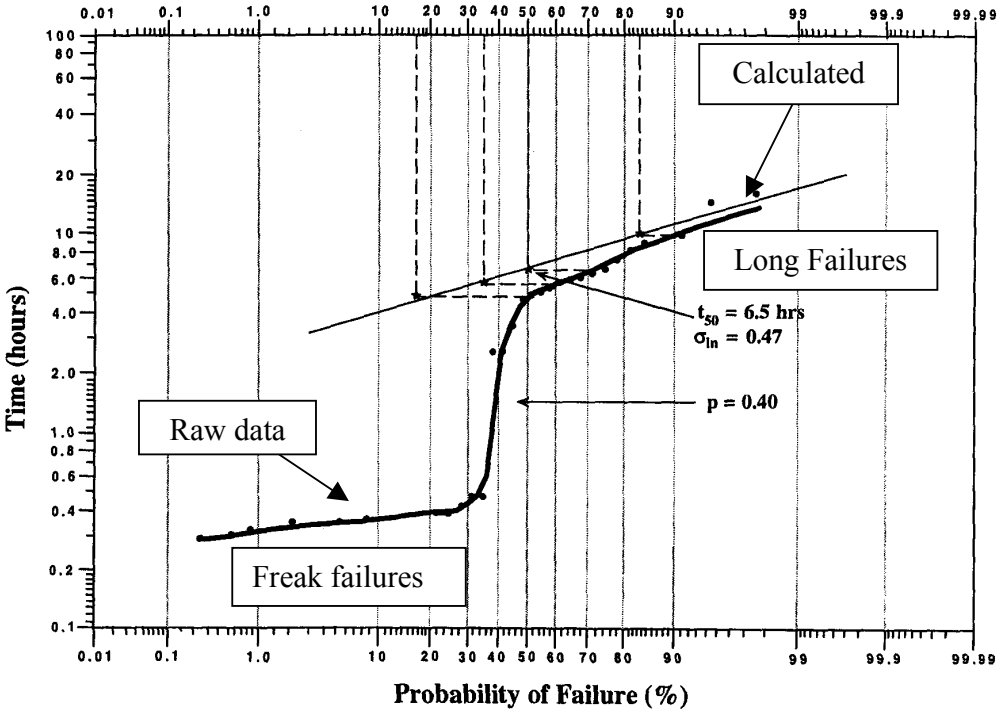

Figure A.1 Probability of failure as a function of time illustrating the raw data and the calculated data.[71]

References:

[1] K.Y. Chen, W. D. Brown, L.W. Schaper, S.S. Ang, and H. A. Naseem, "A study of the high frequency performance of thin film capacitors for electronic packaging," IEEE Transactions on Advanced Packaging, **23** (2), 293-301 (2000).

[2] B. Etienne and P. Sandborn, "Application-specific economic analysis of integral passives in printed circuit boards," in Proc. 2001 International Symposium on Advanced Packaging Materials, (IEEE, Piscataway, NJ) 399-404 (2001).

[3] S. Ramesh, B.A. Shutzberg, E. P. Giannelis, "Integral thin film capacitors: fabrication and integration issues," in Proc. 50th Electronic Components and Technology Conference, (IEEE, Piscataway, NJ) 1568-1571 (2000).

[4] M. Itsumi, S. Ohfuji, M. Tsukada, and H. Akiya, "On-chip decoupling capacitance with high dielectric constant and strength using $SrTiO_3$ thin films electron-cyclotron-resonance-sputtered at 400 °C," J. Electrochem. Soc., **144** (12), 4321-4325 (1997).

[5] J.C. Nino, M.T. Lanagan, and C.A. Randall, "Phase formation and reactions in the Bi_2O_3-ZnO-Nb_2O_5-Ag pyrochlore system," J. Mater. Res., **16** (5), 1460-1464 (2001).

[6] W. Ren, S. Trolier-McKinstry, C. A. Randall, and T.R. Shrout, "Bismuth zinc niobate pyrochlore dielectric thin films for capacitive applications," J. Appl. Phys., **89** (1), 767-774 (2001).

[7] H.F. Cheng, Y.C. Chen, and I.N. Lin, "Frequency response of microwave dielectric $Bi_2(Zn_{1/3}Nb_{2/3})_2O_7$ thin films laser deposited on indium-tin oxide coated glass," J. Appl. Phys., **48** (1), 479-483 (2000).

[8] H.M. Smith and A.F. Turner, "Vacuum Deposited Thin Films Using a Ruby Laser," Applied Optics **4(1)**, 147-148 (1965).

[9] D.B Chrisey and G. K. Hubler, *Pulsed Laser Deposition of Thin Films,* (John Wiley & Sons, Inc., New York, NY, 1994).

[10] J. Cheung and J. Horowitz, "Pulsed laser deposition history and laser-target interactions," Mat. Res. Bull., **17** (2), 30-36 (1992).

[11] J.T. Cheung and T. Magee, "Recent progress on LADA growth of HgCdTe and CdTe epitaxial layers," J. Vac. Sci. Tech. A (1), 1604-1607 (1983).

[12] J.J. Dubowski, D.B. Williams, P.B. Sewell, and P. Normon, "Epitaxial growth of (100) CdTe on (100) GaAs induced by pulsed laser evaporation," Appl. Phys. Lett., **46**(11), 1081-1083 (1985).

[13] M. Ohring, *Materials Science of Thin Films Deposition and Structure 2nd Ed.,* (Academic Press, New York, NY, 2002).

[14] R.K. Singh, O.W. Holland, and J. Narayan, "Theoretical model for deposition of superconducting thin films using pulsed laser evaporation technique," J. Appl. Phys. **68**(1), 233-247 (1990).

[15] F. Aburiet, N. Chaoui, R. Chety, B. Maunit, E. Millon, and J. Muller, "Laser ablation mass spectrometry: a tool to investigate matter transfer processes during pulsed-laser deposition experiments," Appl. Sur. Sci., **186**, 282-287 (2002).

[16] X. D. Wu, B. Dutta, M.S. Hegde, A. Inam, T. Venkatesan, E. W. Chase, C.C. Chang, and R. Howard, "Optical spectroscopy: An *in situ* diagnostic for pulsed laser deposition of high T_c superconducting thin films," Appl. Phys. Lett. **54** (2), 179-181 (1989).

[17] D. B. Geohegan and D. N. Mashburn, "Characterization of ground-state neutral and ion transport during laser ablation of $Y_1B_2Cu_3O_{7-x}$ using transient optical absorption spectroscopy," Appl. Phys. Lett., **55**(22), 2345-2347 (1989).

[18] K.L. Saenger, "On the origin of spatial nonuniformities in the composition of pulsed-laser-deposited films," J. Appl. Phys. **70** (10), 5629-5635 (1991).

[19] J.A. Greer and M.D. Tabat, "Large-area pulsed laser deposition: Techniques and applications," J. Vac. Sci. Tech. A **13**(3), 1175-1181 (1995).

[20] C.B. Arnold and M.J. Aziz, "Stoichiometry issues in pulsed-laser deposition of alloys grown from multicomponent targets," Appl. Phys. A-Materials Science and Processing, **69** S23-S27 (1999).

[21] B. Dam, J.H. Rector, J. Johansson, S. Kars, and R. Griessen, "Stoichiometric transfer of complex oxides by pulsed laser deposition," Appl. Surf. Sci., **96-98** 679-684 (1996).

[22] T. Venkatesan, X.D. Wu, A. Inam, and J.B Wachtman, "Observation of two distinct components during pulsed laser deposition of high T_c superconducting films," Appl. Phys. Lett., **52**(14), 1193-1195 (1988).

[23] R. K. Singh and D. Kumar, "Pulsed laser deposition and characterization of high-Tc $YBa_2Cu_3O_{7-x}$ superconducting thin films," Materials Science and Engineering, R22, **4** 113-185 (1998).

[24] E.V. Pechen, A.V. Varlashkin, S.I. Krasnosvobodtsev, B. Brunner, and K.F. Renk, "Pulsed-laser deposition of smooth high-Tc superconducting films using a synchronous velocity filter," Appl. Phys. Lett., **66**(17), 2292-2294 (1995).

[25] M. Ohring, *The Materials Science of Thin Films 1st Ed.,* (Academic Press, New York, NY, 1992).

[26] R. Messier, A. P. Giri, and R.A. Roy, "Revised structure zone model for thin film physical structure," J. Vac. Sci. Tech. A **2**(2), 500-503 (1984).

[27] R. Messier, "Toward quantification of thin film morphology," J. Vac. Sci. Tech. A **4**(3), 490-495 (1986).

[28] J.A. Thornton, "High rate thick film growth," Ann. Rev. Mater. Sci. **7** 239-260 (1977).

[29] H.C. Ling, M.F. Yan, and W.W. Rhodes, "High dielectric constant and small temperature coefficient bismuth-based dielectric compositions," J. Mater. Res., **5** (8), 1752-1762 (1990).

[30] D.P. Cann, C.A. Randall, and T.R. Shrout, "Investigation of the dielectric properties of bismuth pyrochlores," Solid State Comm., **100** (7), 529-534 (1996).

[31] X. Wang, H. Wang, and X. Yao, "Structures, phase transformation, and dielectric properties of pyrochlores containing bismuth," J. Am. Ceram. Soc., **80** (10), 2745-2748 (1997).

[32] J. Wei, L. Zhang, and X. Yao, "Melting properties of Bi_2O_3-ZnO-Nb_2O_5 based dielectric ceramics," J. Am. Ceram. Soc., **82**(9), 2551-2552 (1999).

[33] W. Hong, Y. Xi, Z. Liangying, and X. Feng, "Phase transition of pyrochlore structure in Bi_2O_3-ZnO-Nb_2O_5 system," Ferroelectrics, **229**, 95-101 (1999).

[34] M. Valant and P.K. Davies, "Crystal chemistry and dielectric properties of chemically substituted $(Bi_{1.5}Zn_{1.0}Nb_{1.5})O_7$ and $Bi_2(Zn_{2/3}Nb_{4/3})O_7$," J. Am. Ceram. Soc., **83** (1), 147-153 (2000).

[35] H. Wang and X. Yao, "Structure and dielectric properties of pyrochlore-fluorite biphase ceramics in the Bi_2O_3-ZnO-Nb_2O_5 system," J. Mater. Res. **16** (1), 83-87 (2001).

[36] J.C. Nino, M.T. Lanagan, and C.A. Randall, "Dielectric relaxation in Bi_2O_3-ZnO-Nb_2O_5 cubic pyrochlore," J. Appl. Phys., **89** (8), 4512-4516 (2001).

[37] I. Levin, T.G. Amos, J.C. Nino, T.A. Vanderah, I.M. Reaney, C.A. Randall, M.T. Lanagan, "Crystal structure of the compound $Bi_2Zn_{2/3}Nb_{4/3}O_7$," J. Mater. Res. submitted, (2001).

[38] I. Levin, T.G. Amos, J.C. Nino, T.A. Vanderah, C.A. Randall, and M.T. Lanagan, "Structural study of an unusual cubic pyrochlore $Bi_{1.5}Zn_{0.92}Nb_{1.5}O_{6.92}$," J. Chem. submitted, (2001).

[39] J. C. Nino, "Fundamental structure-property relationships towards engineering of an integrated NPO capacitor for bismuth pyrochlore systems," Ph.D. Thesis, The Pennsylvania State University, 2002.

[40] Y.C. Chen, H.F. Cheng, and I.N. Lan, " Electrical and optical properties of microwave dielectric thin films prepared by pulsed laser deposition," Integrated Ferroelectrics, **32**, 33-43 (2001).

[41] H.F. Cheng, Y.C. Chen, Y.M. Tsau, P. Kužel, J. Petzelt, Y.H. Zhu, and I.N. Lin, "Dielectric properties of $Bi_2(Zn_{1/3}Nb_{2/3})_2O_7$ electroceramics and thin films," J. Euro. Ceram. Soc., 21, 1605-1608 (2001).

[42] Y.C. Chen, H.L. Liu, K.F. Cheng, and I.N. Lin, "Dielectric properties of $Bi_2(Zn_{1/3}Nb_{2/3})_2O_7$ thin films measured by fourier transform infrared spectroscopy," J. Euro. Ceram. Soc., **21**, 1711-1714 (2001).

[43] R. Thayer, "Bismuth Zinc Niobate Films for Dielectric Applications," M.S. thesis, The Pennsylvania State University, (2002).

[44] R. Waser, T. Baiatu, and K. H. Härdtl, "Degradation of dielectric ceramics," Materials Science and Engineering, A109 171-182 (1989).

[45] R. Waser, T. Baiatu, and K. Härdtl, "DC electrical degradation of perovskite-type titanates: I, ceramics," J. Am. Ceram. Soc., **73**(6) 1645-1653 (1990).

[46] W.L. Warren, D. Dimos, and R.M. Waser, "Degradation mechanisms in ferroelectric and high-permittivity perovskites," MRS bulletin, 7, 40-45 (1996).

[47] R. Munikoti and P. Dhar, "Highly accelerated life testing (HALT) for multilayer ceramic capacitor qualification," IEEE Trans. on Components, Hybrids, and Manufacturing Tech. **11**(4), 342-345 (1988).

[48] G.H. Maher, "Highly accelerated life testing (HALT) of K-4500 low fired X7R dielectric," The 9th US-Japan Seminar on Dielectric and Piezoelectric Ceramics, 357-359 (1999).

[49] L.A. Mann, J. J. Beeson, M.S. Randall, J. L. Paulsen, and E. K. Reed, " Reliability of base metal electrode multilayer ceramic capacitors," The 10th US-Japan Seminar on Dielectrics and Piezoelectric Ceramics, 39-42 (2001).

[50] N. Maffei, "Excimer Laser Ablated Bismuth Titanate Thin Films for Nondestructive Readout Nonvolatile Memory Applications," Ph.D. Thesis, Penn State University, (1993).

[51] J.P Maria,. "Epitaxial $Pb(Mg_{1/3}Nb_{2/3})O_3$-$PbTiO_3$ Thin Films," Ph.D. Thesis, Penn State University, (1998).

[52] Drawn by Brian Edge.

[53] S.L. Swartz and T.R. Shrout, "Fabrication of perovskite lead magnesium niobate," Mater. Res. Bull., **18**, 663-667(1982).

[54] G. R. Fox, S. Trolier-McKinstry, and S. B. Krupanidhi, "Pt/Ti/SiO_2/Si substrates," J. Mater. Res., **10** (5), 1508-1515 (1995).

[55] D. J Lichtenwalner, O. Auciello, R. Dat, and A.I. Kingon, "Investigation of the ablated flux characteristics during pulsed laser ablation deposition of multicomponent oxides," J. Appl. Phys. **74** (12), 7497-7505 (1993).

[56] B.D. Cullity, *Elements of X-ray Diffraction,* (Addison-Wesley Publishing Co. Inc., Reading, MA, 1978).

[57] L.R. Gilbert, R. Messier, and S.V. Krishnaswamy, "Resputtering effects in Ba(Pb, Bi)O_3 perovskites," J. Vac. Sci. Tech., **17**(1) 389-391 (1980).

[58] S.K. Hau, K.H. Wong, P.W. Chan, and C.L. Choy, "Intrinsic resputtering in pulsed-laser deposition of lead-zirconate-titanate thin films," Appl. Phys. Lett., **66** (2), 245-247 (1995).

[59] T. Okada, Y. Nakayama, W. Kumuduni, and M. Maeda, "Observation of scattering of particles produced by laser ablation on a substrate by laser induced fluorescence," Appl. Phys. Lett., **61**(19), 2368-2370 (1992).

[60] D.R. Lide, *CRC Handbook of Chemistry and Physics 81st Ed.,* (CRC press, New York, NY 2000-2001).

[61] Materials safety data sheet for ZnO powder.

[62] L.N. Sidorov, I.I. Minayeva, E.Z. Zasorin, I.D. Sorokin, and A.Y. Borshchevskiy, "Mass spectrometric investigation of gas-phase equilibria over bismuth trioxide," High Temp. Sci., **12** 175-196 (1980).

[63] J.P. Maria, S. Trolier-McKinstry, D.G. Schlom, M.E. Hawley, and G.W. Brown, "The influence of energetic bombardment on the structure and properties of epitaxial $SrRuO_3$ thin films grown by pulsed laser deposition," J. Appl. Phys., **83**(8), 4373-4379 (1998).

[64] I. Stolichnov and A. Tagantsev, "Space-charge influenced-injection model for conduction in $Pb(Zr_xTi_{1-x})O_3$," J. Appl. Phys., **84**(6), 3216-3225 (1998).

[65] S. Zafer, V. Kaushik, P. Laberge, P. Chu, R. E. Jones, R. L. Hance, P. Zurcher, B. E. White, D. Taylor, B. Melnick, and S. Gillespie, "Investigation of hydrogen induced changes in $SrBi_2Ta_2O_9$ ferroelectric films," J. Appl. Phys. **82** (9), 4469-4474 (1997).

[66] U. Chon, K.B. Kim, and H. M. Jang, "Degradation mechanism of ferroelectric properties in $Pt/Bi_{4-x}La_xTi_3O_{12}/Pt$ capacitors during forming gas annealing," Appl. Phys. Lett., **79** (15), 2450-2452 (2001).

[67] R. Munikoti and P. Dhar, "Highly accelerated life testing (HALT) for multilayer ceramic capacitor qualification," IEEE Transactions on Components, Hybrids, and Manufacturing Technology, **11** (4), 342-345 (1988).

[68] E.B. Fowlkes, "Some methods for studying the mixture of two normal (lognormal) distributions," J. Am. Statistical Association, **74** (367), 561-575 (1979).

[69] S. K. Kurtz, S. Levinson, and D. Shi, "Infant mortality, freaks, and wear-out: application of modern semiconductor reliability methods to ceramic multilayer capacitors," J. Am Cer. Soc., **72**(12), 2223 (1989).

[70] M. Pirzada, R.W. Grimes, L. Minervini, J. F. Maguire, K.E. Sickafus, "Oxygen migration in $A_2B_2O_7$ pyrochlores," Solid State Ionics **140,** 201-208 (2001).

[71] R. G. Polawich, "Piezoelectric and Dielectric Reliability in Lead Zirconate Titanate Thin Film," M.S. Thesis, The Pennsylvania State University, (1999).

Automated Polarization Measurement System

developed by Paul Moses

POLARIZATION

This is an automated device intended primarily for measuring the polarization of materials induced by an electric field. It can additionally monitor an external input from, for example, a strain gauge amplifier, and can compensate for linear impedances in the sample. The frequency range is 1 mHz to 1 KHz[1] and the charge range is ~10pc to 100μc. It is based on a PC type computer running DOS 3.3 or better.

A conceptual block diagram consists of:

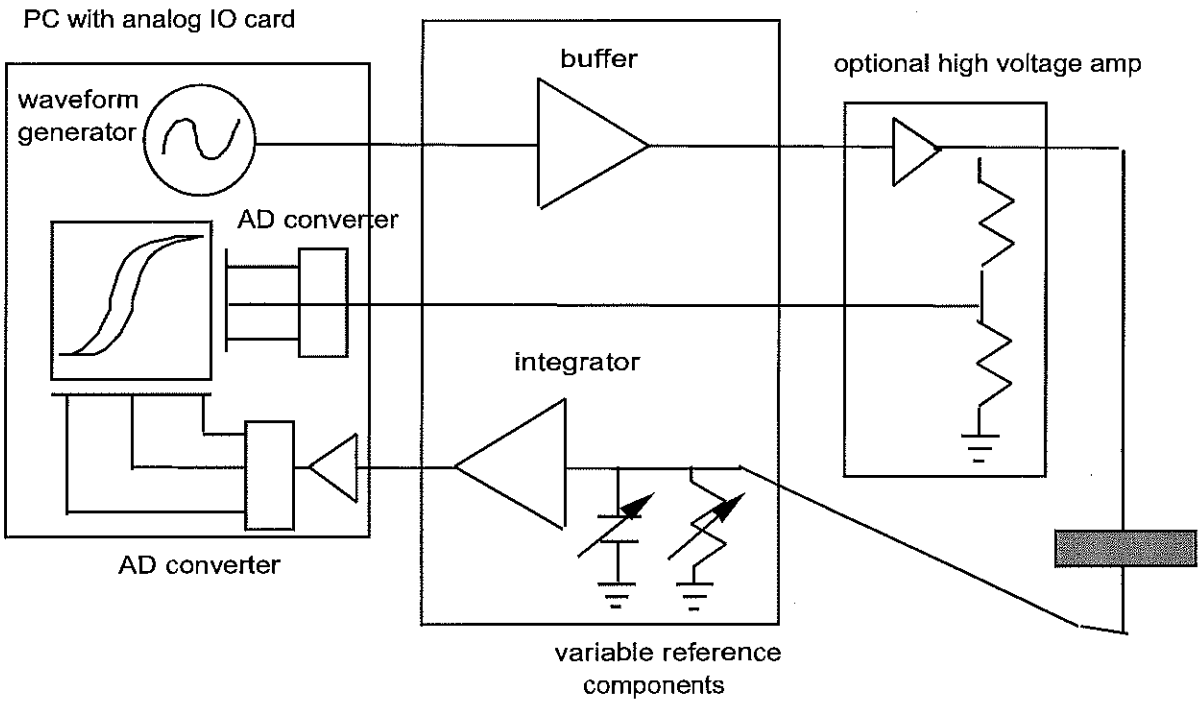

The principle of operation is very simple. Using a multipurpose analog IO card, the computer generates a measurement signal. This signal is amplified by a built-in amplifier with a peak voltage of 10 V and a peak current of 100mA. External amplifiers can be used to provide gains of 10, 100, or 1000 and peak voltages of up to 10kV. The external amplifiers must be provided with precision voltage dividers equal to the gain of the amplifiers.

The amplified signal is applied to the sample. The resultant current is absorbed by the integrator which converts the current to into an output voltage proportional to the input charge. The integrator is automatically zeroed before each new acquisition. This signal,

---

[1] depending on the computer and IO card used

the divided applied voltage, and an external input are fed to the IO card which digitizes the three signals. All further processing is done by the computer (in computer controlled mode).

The hardware and software are constructed so that the computer IO card, external circuitry and amplifier work together as a single virtual instrument controlled from the keyboard. As such, most of this manual will be without specific reference to exactly which of the four components is doing which task. Use of the system in manual mode has fewer options and is less complex so it is discussed in a seperate section.

Using the device is straightforward, unfortunately you must first run the program before connecting the voltage amplifier or sample, this is very important. Initializing the circuitry results in a number of voltage spikes which are typically more than sufficient to destroy your sample. The program is called from a bat file "charge". The program sets various starting values (for example it sets largest possible reference capacitor and resistor and the applied voltage to 0) then enters the menu state. At this point you make a number of choices from the menu using the ⇑ ⇓ ⇐ ⇒, ENTER, HOME, and 0-9 keys. Some menu items are 'multiple choice' and are scrolled through using the ⇐ ⇒ keys. Others require numeric parameters. To enter them use the ⇑ ⇓ keys to select the menu item, then one of ⇐, ⇒, HOME, or ENTER keys and the program will usually prompt you for the numeric value. On some menu items one or more of these keys executes a special function. Those items which have a HOME function are indicated by a small 'house' next to the menu title.

Pressing F1 starts a measurement. The measurement either finishes on its own or after you press ESC (this is explained in the sweep mode section) and the program re-enters the menu state. You press ESC or CTRL-C to exit the program. The menu options fall into two classes, those that affect only the display and those that affect the measurement, each type is explained below.

MEASUREMENT SECTION

Period: Use the ⇑ ⇓ to highlight period in red. Hit either ⇐ or ⇒ then type in the desired value of the period of the applied signal in seconds, then hit ENTER. The program will calculate the closest available period and display it. The range is 1 mHz to 1KHz.

Acq mode

There are 7 different acquisition modes available: one-shot, delayed, sequential, averaged, continuous, memory, and stepped.

One shot: Applies the measurement signal with the specified period for one cycle, acquiring data at the same time, stops, then redraws the screen, with an automatically calculated scale (if autoscale is on).

Delayed: Applies the measurement signal with the specified period n times without acquiring any data, 1 more time while acquiring data, then stops. The menu parameter "# cycles before acq" sets n. The range of n is 0 to 2^9. (A delayed sweep with n=0 is exactly the same thing as a one-shot). You might use this delay mechanism to do two things. First a hysteresis loop is often desired without the initial rise from zero. A delay of 1 will cause the measurement to be made on the second cycle rather than the first

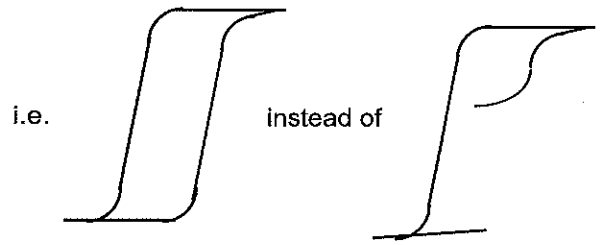

Second, it is possible to do a simple aging study by acquiring samples with delays of say, 0,8,89,899,8999, which would result in acquisitions of exactly the first, tenth, hundredth, thousandth, and ten-thousandth cycles.

Sequential: The program takes a one-shot, redraws the screen quickly, displaying the raw data from the AD converter, then repeats. The period of the signal applied to the sample is correct but the repetition rate is determined largely by the time it takes to redraw the screen, so if you have a period of, say, .1 s set each measurements done with that period but you won't see 10 new measurements each second.

Averaged: This is like sequential but each cycle is averaged with the previous ones to reduce any noise that might be present. The system is phase-locked so the averaging is effective.

Memory: Memory mode is just the sequential mode with one thing added. For 9 cycles the program automatically measures, draws the raw data on screen, then stores the

data in reference traces 1-9. This allows you to automatically catch the first few applied cycles in a fast, automatic way.

Stepped: This is also the sequential mode with one thing added. The peak applied voltage is increased ~5% every cycle. You can use this to gradually and automatically increase the voltage to watch for the onset of hysteresis. Unless you set the reference components and AD gain low enough before you begin this acquisition then you will probably have to interrupt this process (hit any key) from time to time because the correct settings for the first cycles will not be correct for later cycles.

Range: Three ranges are available, internal (+/- 10V), 10X external (+/- 100 V), 100X external (+/- 1000V), and 1000X external (+/- 10kV). This is limited by the peak voltage selected.

Pk voltage: The peak value of the applied signal. This value is limited by the range selected. It is entered numerically or using the arrow keys. You have to select a range / peak voltage combination which is self-consistent. For example you can't select a peak voltage of 100V on the 15V range, and you can't reduce the range to 15V if you have already set a 100V peak signal. In general when raising the applied voltage to a new range, change the range first then the peak voltage. When reducing the peak voltage, change the peak value first, then the range. With this item selected you can enter the value numerically by first pressing ENTER or HOME then entering the value at the prompt. Alternately, if you would like to gradually raise the voltage applied to your sample and monitor the pattern you should set the sweep mode to single shot, then select this menu item and press the right arrow. This will increase the applied voltage about 10% and take one measurement which you can see on the screen. You can then press the arrow again and repeat the process increasing the applied voltage ~10% each time, 8 repetitions will precisely double the applied voltage. You can also use the left arrow to decrease the applied voltage. You might also have a look at the *stepped* acquisition mode, which is an automatic version of this.

C_{ref}: This selects one of seven reference capacitors. The HOME button will start an autoranging sequence that will do its best to optimize the choice of Cref and AD gain to do a charge measurement with the selected signal parameters (period and pk voltage). Cref interacts with AD gain, bias comp and period and this should be considered when selecting Cref.

AD gain: This controls the amplification of the AD card. Remember that first the signal from the sample is accumulated by the converter, then the output from the converter is digitized. This controls the amplification of the IO card's digitizing step. There is a different gain for each of the three input signals: applied field, charge, and the external input. The AD gain for the applied field is always automatically set. For the other channes it can is set by the autorange sequence (Cref, HOME). You can also set it manually. Basically you should start with it as low as possible (1), set the other elements (Cref, applied field, and/or external signal), then raise the AD gain until the program warns you that it is saturated, finally back it off one setting. You could also only raise it until your pattern on the screen has adequate resolution and signal-to-noise ratio but that is not necessarily as good as it could get.

Bias Comp: Used to control leakage from samples. There are 4 settings available, 10^7, 10^8, 10^9 ohms, and none. Depending on the frequency being used (Cref * Bias Comp resistor should be much less than the period) this can be used to control drift on the screen. The reistance chosen is placed in parallel with the reference capacitor so that charge which fails to average to zero (asymmetric leakage current) won't cause the loop to continuously drift.

Waveform: You have the choice of four waveforms: sine, triangle, unipolar, and user-defined. The first two are self-explanatory. The unipolar waveform is the first half-wave of a sine wave. The intended use is with strain measurements when only one polarity is to be applied to the sample. It is possible to apply either a positive or negative cycle to the sample by setting the peak voltage to a positive or negative value. To use the fourth choice you have to edit the function userwave (x) in the file userwave.bas . This subroutine should take a real value between 0 and 2π and return a real value between ± 1 to ensure that the program scales the applied signal correctly. Regardless of the value of your function at 2π, the program will set the last output point to 0V as a safety measure to prevent high voltage from remaining across the sample after the sweep is done. After writing your function you compile it with BC.EXE resulting in an object file userwave.obj. Then run the bat file qlink.bat which will relink the rest of the program with your function. When using Quick Basic qlink expects to find the following files: st.obj, brun60er.lib, pclabdrv.lib, support.lib. After using qlink you should have a new executable file q.exe which is called by the bat file charge.bat. If it should become necessary to change the main program there is a bat file called qcomp.bat which will recompile the source file (q.bas) with the necessary options.

DISPLAY SECTION

Cursor: This is used to read exact values from the screen. When the cursor line is selected the ⇐ and ⇒ buttons will move a yellow box on the screen from point to point. There is another larger white box which jumps to the same point as the yellow box when the HOME button is pressed. The difference between the x and Y values at the points selected by the two cursors is displayed beneath the menu items (in the same units as the full scale values shown another line to two down). Unfortunately, moving the yellow cursor tends to erase points under the box. The display can be refreshed by hitting ENTER

X and Y axes: You can normally display any of the following 4 quantities on either axis: time, applied field, charge/current, or the voltage on the external input. In some acquisition modes time is not available.

Math

There are 3 math functions available: loop area, Pr&Ec, and re-zero.

Loop area: The program will calculate the area of a trace for you if you press either ⇐ or ⇒ while loop area is selected. The algorithm used expects your trace to define a simple closed curve. A normal hysteresis loop is a simple closed curve so the answer given by the program will be correct but it is possible to measure loops which don't close or cross themselves and in those cases an answer will appear on screen normally but it will be wrong. It is up to you to ensure that your measurement defines a simple closed curve. The answer is given in the same units as the scale and as the cursor, so if you make a charge (polarization) measurement the answer will be in units of energy density.

Pr&Ec: Given a reasonable loop the program can find the remanent polarization and the coercive field by interpolating the zero-crossings. If you have a bad loop the answers will be nonsense. The program marks the locations of the zero-crossings with short blue lines then prints the values on the screen.

Re-zero: This option will center a loop for you about the horizontal axis. An arbitrary hysteresis loop should not be expected to lie centered. The program starts all measurements at 0 so the amount the loop is off center is determined by the amount of remnant polarization in the sample when the measurement began.

Ref: There are 10 reference memories, numbered 0 through 9, which can be used to store a trace. To store select the reference menu item, press ⇒ , then a number 0-9. Recalling a trace is done the same way but with ⇐ . The recalled trace is always displayed on the same scale as the last measurement (which always remains on screen) so it may be clipped or squeezed into a small area depending on the scale of the active trace.

Info: Pertinent information about the sample is entered here. You can enter the sample's area or, if the sample is round, enter the diameter and the program will calculate the area. You can enter its thickness and give it a name which will appear on

printouts and in the saved settings file. You can also define units to be used with the external input so that if, for example, you are connection a strain measurement which has an output of 1 μm per volt you can define a "μm" unit and enter the ratio of 1 per volt. The screen will then display the external input in those units rather than in millivolts, the default unit.

Plot: This prints the screen on a Hewlett-Packard inkjet or laserjet printer. After selecting plot you may enter a one-line comment which will appear on the printout. Other information, the sample name, dimensions, and the date also appear on the printout. If you enter "no" as the comment the plotting operation will be canceled.

Disk: A sweep can be stored on disk. A stored sweep can be read from disk to the screen. Just select the disk menu item and press ⇐ or ⇒ and answer the questions. When storing data two files are created: name.pol and name.set where name is the name you enter. The file are written to the volume given in the program's include file and contains 4 columns of about 250 points each (depending on how many points were in the reference trace). The columns consist of: the applied field (V/m), charge, the voltage on the external input (V), and elapsed time separated by a tab. If the resultant signal has been compensated or integrated the rccorded data reflects this. The settings file contains the values of the settings of the device so that a record exists of important information like the period and peak voltage. The setting file also contains some other information such as the name of the sample (see "info - name" below).

Compensation

There are three virtual compensation components available: compensation for linear capacitance, linear conductance, and input bias current. They exist only in software. The idea is to subtract contributions to the resultant signal from each of the three effects. This section works only with a charge measurement. You select a compensation component in the same way you enter other numeric parameters (like the period). By pressing HOME you also have defaults which the program calculates for you. The compensating charge is calculated according to:

$$Qcomp = CcompVapp^{t} + \frac{1}{Rcomp}\int_{0}^{t_s} Vapp(t)\,dt$$

where ts is the time value of each measured point starting from t=0 at the beginning of the sweep. The default compensation components are calculated according to the property that a linear resistor will produce a resultant charge signal which is exactly out of phase with the applied voltage and a linear capacitor will produce a charge exactly in phase with the applied voltage. So finding the compensating capacitor consists of integrating the resultant signal (charge) against the applied voltage and the compensating resistor is calculated by integrating against the applied voltage phase shifted 90°, i.e.:

$$Ccomp=\frac{2}{V_{pk}^2 T}\int_0^T Qin(t)Vapp(t+\delta)dt$$

$$Rcomp=\frac{-T^2V_{pk}^2}{4\pi}\int_?^? Qin(t)Vapp(t+\delta)dt \qquad \delta= T/4$$

Tests indicate that the method is accurate to about 5% under most circumstances in determining the size of actual (linear) components intentionally placed in parallel. But it is unlikely that these components sizes are the optimum choices for the question as stated (by ceramists) as compensating for linear, parallel impedances. Experience suggests it is really nothing of the sort and consequently the algorithm used may answer the question as stated without doing what is desired. Significantly more sophisticated programming combined with much better knowledge of the problem would be required to resolve it. Until then this must remain a matter for your judgment. The bias current compensations corrects for the current drawn by the converter. On a charge measurement that current would tend to add a linear contribution to the measured charge.

Auto Scl: This turns the auto scaling feature on and off. When on, with each new screen the program will pick a reasonable scale for both the x and y axes. When off the same scale is used until it is changed by turning the auto scale on again. When the auto scale is turned on the screen is cleared and a new scale calculated, when it is first turned off you are prompted for the x and y extremes you want to use.

Connect: The data taken always consists of a sequence of points. For the sake of display clarity those points can be connected or shown as distinct points using this option.

Auto Save: With this option on every time the program makes a measurement and returns to the menu state the measured data will be saved on disk. The directory is specified in the program's include file. The files are pol.NNN and settings.NNN when NNN is a number 001 through 999. Each time the program is started the count is set to 001 and automatically incrememented with each measurement cycle. Old files are automatically written over. With hysteresis measurments samples are often tested to the point of breakdown, sometimes even on purpose. This option allows you to make measurements without tediously saving files at each change in voltage or frequency and without risk of losing the last and usually best cycle. Pressing the home button erases the previously saved files and starts the counter over again.

EXTERNAL CONNECTIONS

There are four external connections.

1. Sample Low: Self-explanatory

2. Vout: This is a 10V peak output which can drive a low voltage sample directly or can be used as the input to a high voltage amplifier. The amplifier can have a gain of 10, 100 or 1000.

3. Voltage Monitor: When an external amplifier is used it must have a voltage monitor/divider with a division factor equal to its gain. The output of that divider is plugged in here so the system can measure the actual applied voltage.

4. External Input: The system can also monitor an independent external signal, for example, from a strain gauge preamp.

5. External Ref: This connection allows you to insert your own reference component. For instance if you have a very large charge source you can connect a very large capacitor or if you want to measure current instead of charge you could insert a resisitor of the appropriate value.

Strain Accessory

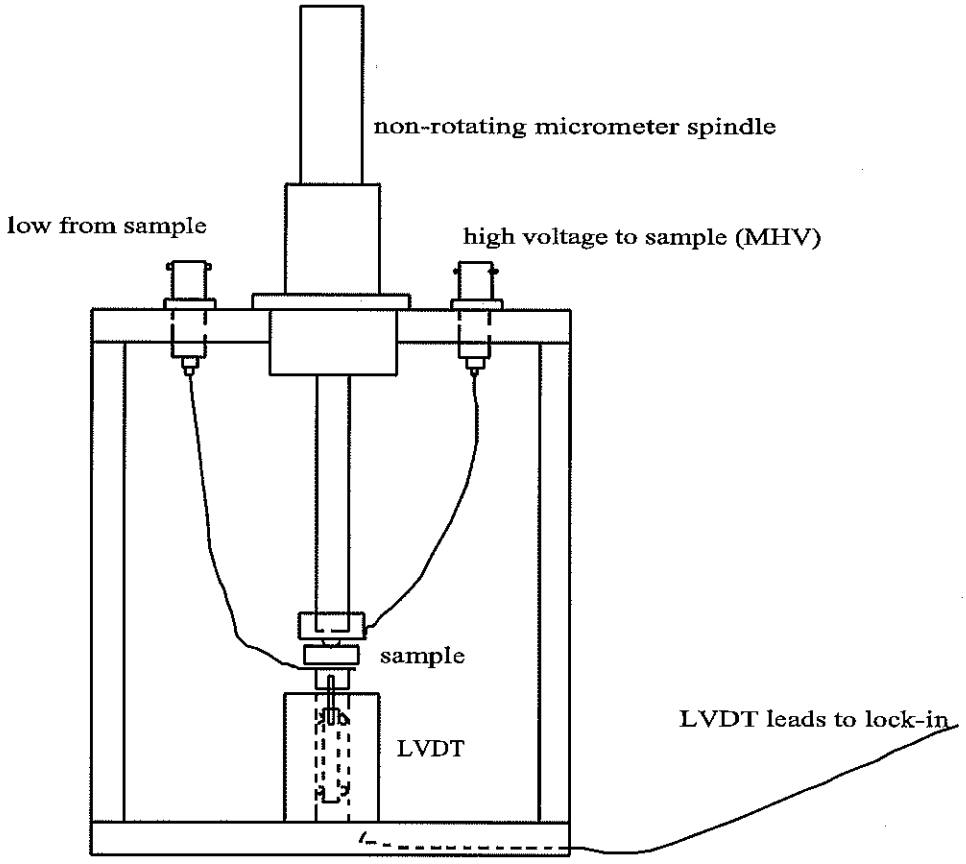

The following describes an easy-to-use instantaneous-type[2] strain measurement intended for use with actuators and relatively high strain materials which works in conjunction with the polarization measurement system and a lock-in amplifier, preferably the Stanford Research 850 or 830. The resolution is better than 3 nm, depending on the measurement time, and the frequency "range" is .001 Hz to 10 Hz. It uses the polarization measurement system to apply the voltage to the sample and to acquire the strain data, the maximum voltage with the existing supplies is 10 kV, so you don't need a very thin sample. The fattest sample you can use is 15 mm. The system can measure the charge from the sample at the same time as the strain and can display it or plot it against the applied field, the charge, or time. You can also use this as an easy holder for polarization measurements at room temperature without measuring the strain, just don't connect the lock-in.

The sample (which normally should be electroded) is held in place between two probes, a little like the d33 meter. The whole gadget, consisting of a small frame, an LVDT, the hold-down micrometer, and the wiring can be immersed in Flourinert when necessary to prevent air breakdown. **Whenever it is used with voltage exceeding 250V it must be immersed in Flourinert to prevent breakdown to the LVDT and destruction of the lock-in**. I have made a container to hold the fourinert into which the strain fixture fits which you should use and cover when you're done to keep the flourinert from evaporating. There is a metal mesh which fits on the flourinert container to allow the fixture to drain for a few minutes after you have finished. Both the strain gadget and the flourinert container should be kept in the cabinet in the poling room. Right now the electrical contact to the sample is made by the mechanical probes that hold it in place, which is very convenient for a "33" measurement, but in the future I want to add connections to allow a "31" measurement. The strain is converted to an AC voltage by the LVDT and the AC voltage is converted to a DC voltage by the lock-in[3]. The DC voltage from the lock-in is measured by the auxiliary input to the polarization system. In the next few months I want to build a demodulator to replace the lock-in but until then the lock-in has to be shared with people using it for other things. If you can't find it when you need it look in the Research Unit.

Using it is intended to be as simple as possible. In principle you only need to plug things in and adjust the range taking care not to blow anything up. Following is a step-by-step sequence:

1. Insert the sample **gently** tightening the micrometer onto it and connect the sample high and low cables **but not the cables from the LVDT to the lock-in.** Connect the baseplate to a ground on the voltage supply or equipment rack using the baseplate ground wire. The bottom probe is the electrical high and has an MHV connector. If you are making a charge measurement set it up and run at least one cycle. If not, ground the low

---

[2] An instantaneous strain measurement can give you a picture of the strain in your sample as a function of time. This is in contrast to an averaged strain measurement which gives you one number, a d or Q coefficient for example.

[3] If you are unfamiliar with what lock-ins do please read the document about lock-ins in the reference computer.

side of the sample using a shorting BNC plug, set the voltage, period, and AD gain[4] and apply the full voltage at least once. In either case I suggest working with a period of 1 second. This step of applying the voltage is to make sure there are no shorts which could kill an $8000 lock-in. It will also simplify the lock-in ranging later if the computer screen is already set up. Then set the computer display to show you the aux input on the y-axis, which at this point will just be garbage.

2. Connect the lock-in to the LVDT (2 BNC's) and plug the channel 1 output from the lock-in into the aux input of the polarization unit.

3. Insert the disk containing the lock-in set up file. There should be a disk near the lock-in labeled *Lock-in Setups*. If not, copy the file \LOCKIN\STRAIN.85S from the polarization computer to any DOS formatted double density disk and use it. Recall the settings by hitting[5] DISK then Settings Recall, Catalog, and use the knob to select STRAIN.85S then hit Recall. The screen should show you a polar plot on top and a number with a bar graph on the bottom. The polar graph shows the total signal from the LVDT at 10 mV full scale and the bottom gives the X component of the signal. The X component is proportional to the displacement, the Y component is quadrature error and should be less than 3 mV once the LVDT is nulled (next step). Look at the bottom left corner of the screen. There are several boxes, one of which should say STOP, which is normal. Two of the others are warnings for overloads on the output and dynamic reserve. After the micrometer is adjusted, they should never be on during this measurement. If they go on, unless some noticeable external vibration is present, then something is screwed up. The settings recalled in this step are general purpose for 1 Hz. To work at 10 Hz or for the minimum system phase shift you should reduce the lock-in time constant and you may raise the time constant at .1 Hz.

4. Slowly adjust the micrometer so that the X component is between +/- 1 mV. This adjustment is backlash sensitive and you should always stop while *tightening* the micrometer. If you overshoot, loosen the micrometer a little and start again. Depending on thermal expansion and residual strain in your sample you may have to periodically re-adjust this, although probably just changing the offset described in the next step will be OK. If you have to adjust the micrometer, make sure the offset is set to 0%.

5. Press OUTPUT OFFSET and Auto: to subtract the rest of the offset. When taking measurements, if the strain picture drifts up or down you should reset this.

6. Press F1 to make a measurement. Three things can happen:

a. If the AD converter is saturated then press GAIN TC, Sensitivity and spin the knob clockwise to decrease the lock-in sensitivity. Go back to step 5.

b. If the measurement resolution is not good enough, in which case you will see widely scattered dotsthen you have two options. First, you can increase the

---

[4] To set the AD gain you can just hit the HOME button on the AD gain menu line.

[5] Front panel buttons on the lock-in are shown in boxes, softkeys are underlined in dots.

sensitivity of the lock-in as in a. above but with a counter-clockwise spin. The sensitivity can easily be increased to as much as 2 mV full scale, higher if you know what you are doing[6] . Or you can press OUTPUT OFFSET, Expand and use the knob to pick an output amplification. Go back to step 5.

c. Good measurement. Plot it or do whatever you want then turn off the high voltage and go back to step 4 with your next sample or tell your advisor you worked all day at this then go home.

For now the polarization system will only show you the voltage from the aux input, it won't calculate strain for you, here is the formula. Using the default lock-in settings the net scale factor is one Volt per μm.

$V_{on\ screen} = \Delta l * (\text{LVDT sensitivity}) * (V_{app} \text{ to LVDT}) * (\text{lock-in conversion ratio}) * (\text{lock-in scale expansion})$

LVDT sensitivity = 250 $mV_{AC}/mm/V_{app}$
V_{app} to LVDT = 4 V_{AC}[7]
lock-in conversion = 10 V/full scale sensitivity (10 mV by default)
lock-in expansion = your setting (1 by default)

To recall the instrument state for strain measurements you press **SETUP RECALL**, dial **9**, then press **SETUP RECALL** again.

The correct settings are:
Input:
Time constant: 1 ms, 24dB/oct rolloff
Sensitivity: 10mV
Input A, AC coupled, Ground
Reserve: Low Noise
Filters: Line and LineX2

Channel One:
Display: X
Output: X

Channel Two:
Display:Y

---

[6] The best resolution is achieved at the highest sensitivity but you may have to adjust the dynamic reserve and that is tricky because the output warning box will light up from the quadrature error and you have to know when it is safe to ignore it. The signal-to-noise ratio can also be improved by using the averaged acquisition mode of the polarization system.

[7] The drive is actually set higher to compensate for the LVDT primary coil impedance and the softness of the nylon screws. You can think of 4V as the effective drive voltage.

Reference:

Phase: 0.00 deg
Freq: 2.000 kHz
Amplitude: 4.5 V
Harmonic: 1
Source: Internal

You will set the offset as with the 850. If the strain graph floats above or below the screen centerline, press **auto offset** to zero the lock-in output. If necessary turn the offset off and adjust the micrometer. Remember to finish all micrometer adjustments by tightening.

Strain Measurement Conversion Table

Room Temperature Fixture with 4.5 Vac used

Lock-in Sensitivity	μm/V
100 mV	10.
50 mV	5.
20 mV	2.
10 mV	1.
5 mV	.5
2 mV	.2
1 mV	.1

As a rule the time constant of the lock-in should be 1/1000 of the period of the measurement. If the strain curve has sharp features and you need the minimum distortion you may need to use 1/3000 of the period. For better noise rejection you may be able to use 1/300 of the period.

MANUAL POLARIZATION MEASUREMENT

The polarization measurement unit can be used with a signal generator and oscilloscope and without the computer interface for manual polarization measurements. A small control unit is plugged into the polarization measurement box to substitute for the computer control. Used in this way the polarization unit is simply an electronic integrator which is typically applied to the oscilloscope's "Y" input. A signal proportional to the applied voltage (for instance from a high voltage amplifier's monitor output) would be applied to the oscilloscope's "X" input and a the XY trace would show polarization vs. field, i.e. a hysterisis loop. In manual mode the user sets up the signal generator to produce the desired waveform and sets up the oscilloscope for the desired display.

There are only three controls on the manual control unit: Reference Capacitor, Bias, and Short. The Reference Capacitor and Bias are as on the computer controlled system. The purpose of the Short control is to prevent the accumulated charge from drifting off scale. When under computer control the system automatically re-zeroes before each measurement and the user may not even be aware it is happening. Under manual control the accumulated charge must also occasionally be zeroed for two reasons. One, ferroelectric samples often produce slightly more leakage current in one direction than in the other. Two, the charge integrator has a small input leakage current. Either of these current sources can gradually cause the hysterisis loop to drift away from center. This can be done in two ways.

First, simply press the Short button. This will zero the charge. Second, if the signal generator has a TTL sync pulse that can be used to zero the charge at the beginning of each cycle. Simply connect the sync output to the short in BNC. A TTL transition will generate an approximate 5 ms pulse to short the charge. This can only be used with relatively low frequency measurements (.1 second period or slower) because the integrator is shorted for 5 ms during the cycle and charge released during that period is lost.

ELECTRONIC DETAIL
(for LabPC IO card)

In the most sweeping generality possible the circuit consists of an output amp and input integrator with an auxiliary output and input for an external amp.

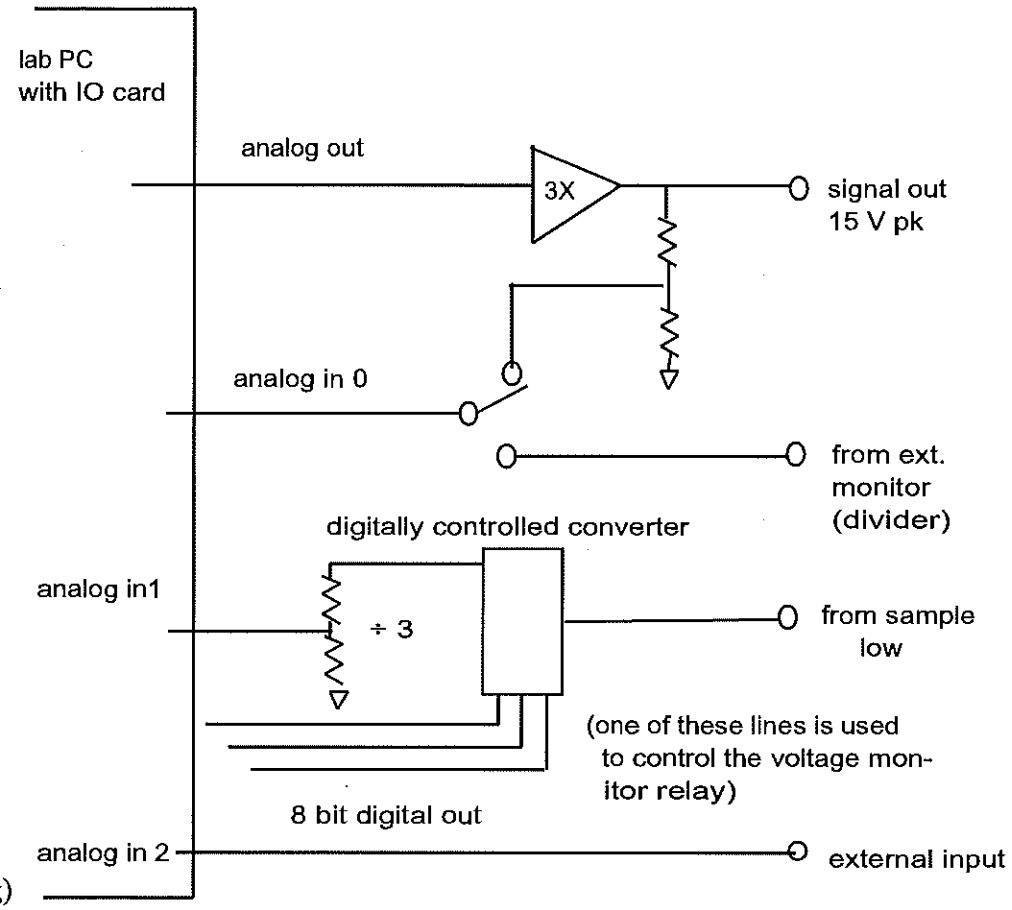

(fig)

The whole thing is powered by 5V from the computer which is converted to ±15V by DC-DC converter. The output section consists of an RC filter to smooth the digital output steps and a X3 amp with 40 mA output current, made from an LF353 and LH0002. This is capable of supplying a normal sized sample at normal rise times but could conceivably current limit with a large sample especially if a user function is written with a fast rise time.

This output signal is fed to a x2.5 divider which feeds one of the terminals on the voltage input relay, which selects input from either an external divider or the internal divider. This relay is controlled by bit A4 from the labPC card (boosted by one of the high current open collector buffers in 74072).

The converter is another LF353/LH0002 combination with feedback components selected by the user. There are 5 resistors (10^8, 10^7, 10^6,10^5,10^3 Ω) and 6 capacitors ($2*10^{-5}$,10^{-6},10^{-7},10^{-8},10^{-9},10^{-10} F) each in series with a reed relay. The relay is controlled by a 7407 (7407_1 for the capacitors and 7407_2 for the resistors) each section is controlled by a separate 74LS154 so that the resistors and capacitors can be selected independently. The 74LS154 is controlled by bits A0-A3 from the lab PC card. In order to simplify the layout C1 corresponds to channel 8 on the LS154. Bits A5-A7 control $74LS154_2$ (bit A4 is fed directly to 7407_2 to control the voltage input relay). The highest order bit of 75154_2 is held high and again R1 corresponds to channel 8>

The integrator is perfectly standard. A 10pF capacitor is always in place to ensure stability. The input is protected from sample breakdown by high speed surge absorbers. The exact values of the feedback components are stored in an include file. You are free to change the feedback components as necessary. In particular you can eliminate the most sensitive capacitance range and add a new 100μF range if you are careful to use temperature stable low leakage capacitors (polycarbonate or polystyrene) as long as you change the values in the include file. Furthermore the exact values of the various voltage dividers are stored in the same place. These should be changed if the divider components are replaced. You must then re-compile and re-link according to the directions in the userwave section.

SPECIFICATIONS

Integrator Section

Ranges	Reference
100μC	20μF capacitor
10μC	1μF capacitor
1μC	100nF capacitor
100nC	10nF capacitor
10nC	1nF capacitor
1nC	100pF capacitor

Freq range:	1mHz to 1 kHz max depending on computer
Basic accuracy:	3% +.5% of range (5% on 1nC range)
Resolution:	range/2048
Offset:	10mV when reference resistor ≤ 10MΩ
	15mV when reference resistor ≤100MΩ
Drift:	50pA * Cref(in volts/sec) when Rref=1 terraΩ

Offset and drift errors will appear as error*Cref/(sample area) or error/(Rref*sample area) depending on whether a charge or current measurement is being performed.

Output

Ranges: ±10 V (±100V, ±1.kV, ±10kV using external amp)

FILES

q.bas-	basic program
uwave.bas-	basic subroutine defining the user wave function
q.inc	an include file containing calibration values and system defaults
uwave.obj-	object (compiled but not linked) file for user wave.
q.obj-	object file for main program
qcomp.bat-	batch file which will compile q.bas using the correct options
qlink.bat-	batch file which will link q.obj + uwave.obj necessary libraries to create executable file
q.exe-	executable file which should work
charge.bat	bat file to run program
labpcdrv.lib-	library of drivers necessary for IO card
support.lib-	miscellaneous stuff necessary for lab driver
bcom60er.lib-	library necessary to make executable files
conf.exe-	executable file to configure the IO card. It creates a file lpc_brds.cfg which contains configuration information necessary for the IO card. We are including a copy of this file so that re-configuring should be unnecessary.
lpc_brds.cfg-	configuration file for IO card.
labpcdrv.inc-	definition for basic programs using lab pc's
no.txt-	a nearly empty file which supplies returns for qcomp.bat and qink.bat

INSTALLATION (for LabPC IO card)

1. Refer to manual for the lab PC IO card. Verify that the base address is 2804 insert the lab IO card connect the polarization unit. Note: The address is not the factory default. The default address is not used because it conflicts with the address of the HP Basic processor card used in HP Vectra's.

2. Copy all files from 3 1/2 diskette to an empty directory on the hard disk.

3. From that directory type charge IF this fails: Type qcomp and wait for compilation to finish. This assumes the existence of the basic compiler bc.exe in the search path. Then type qlink and wait for it to finish. This assumes the existence of the quick basic linker in the search path. You may also have the DOS linker which will not work. If there is a link error generated (bad record...) re-order the search path to put the quick basic linker in front or rename the DOS linker. Try charge. again.

4. In the event. A configuration error involving IO card run the executable file lpc_brds.cfg. Ensure that the configuration is set to:

Board ID = 1

Type = lab-pc

Base address = 2804

Int lvl = 5

DMA chan = 3

DAQ mode = DMA using selected channel in the event of further problems contact somebody smart.

TEST PROCEDURE

The first and simplest test is to switch the unit to **test**, disconnect all inputs and outputs, run the program, then autorange by hitting HOME on Cref. You should see a nearly closed ellipse at an angle on the screen. The program should have autoscaled to +/- 2MV/m and +/- .01 mC/m^2.If this is not satisfactory you can perform the following which is not a calibration, only a further test to determine if the device is functioning correctly. The idea is to measure a number of capacitors and resistors of known value to exercise each of the reference components.

Collect the following components: 1μF, 1nF capacitors; 10MΩ and 10KΩ resistors. Measure them on an LCR meter at 100 Hz.

Run the program. Enter the diameter as 17.8 mm. This way the program will calculate an area of .001 square meters so that the scale factor on the polarization display (which is in mC per square meter) will be exactly one million. Enter the thickness as one micron so that the field display (which is in MV/m will read the applied voltage in volts directly.)

Set the period to .01s and Vapp to 1 V.

Set Cref to 10μF and Rref to 10^{12} Ω. Insert the 1μF cap and take a one-shot. You should obtain a straight line or narrow loop like the following:

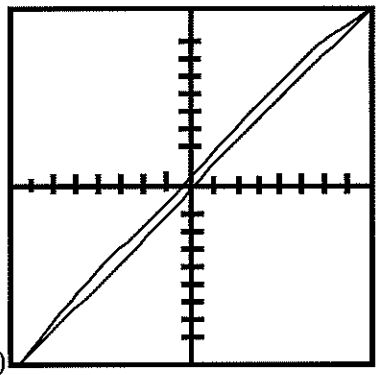

(fig)

Use the cursors to measure the peak to peak field and polarization. You should obtain a pk-pk field of approximately 2V (2 MV/m). The actual polarization is (external capacitance)*(applied voltage). The measured capacitance should be about 1μF and the applied voltage should be about 2V. The program will display the polarization in mC/m2 which should be exactly one million times the bulk polarization (since the area should have been entered as .001 m2). If these don't check you have a problem.

Repeat this test with the same external cap (1μF) but with Cref = 1μF then 100nF. The measured values should not change more than the specified error.

Replace the external capacitor with the 1 nF capacitor and repeat for Cref = 10nF, 1nF and 100pF. Of course you will have to recalculate the polarization because the external cap is different.

Set the period to 1 s, Cref to 100 pF and Rref to 100 MΩ. Insert the 10MΩ resistor and take a one-shot. You should obtain a similar picture. The calculation is exactly like the above except that the current is (applied voltage)/(external resistance. Repeat with the 10 MΩ external resistor for Rref = 10 MΩ and 1MΩ.

Replace the 10 Mohm external resistor with the 10 KΩ resistor for the last 2 Rref ranges.

Blind Repair of Hysteresis Circuit

1. Check all fuses. There are two in the external box and one on the Lab PC IO card.

2. Check the input diodes in both directions with a diode checker. These are Shottky diodes so they should be about .2 to .3 V. in the forward-biased mode. Replace either open or short circuits.

3. Replace the LF353 in the sample low circuit. When you install this chip, be sure to hook up the inputs exactly as they were. That is, the inverting input (pin 7) is not installed into the socket but soldered directly to the lead wire.

3. Replace the LH002 in the sample low circuit.

4. If these two things don't work, call the technician.

Chapter 1 Introduction and Statement of Goals

1.1 Introduction

As clock rates and integrated circuit gate density increase, discrete chip capacitors do not satisfy the decoupling requirements for high current switching at high frequencies.[1] In addition, some engineers believe that discrete surface mounted passive components are also reaching their limits in performance, cost, reliability, and size. Certainly, the use of integral passives reduces assembly costs and shrinks the required board size.[1,2] Because low value ceramic chip capacitors (<1000 pF) constitute about 40% of all capacitors used in handheld applications, and because they may eliminate some of the above complications, they are being considered for replacement by integral capacitors.[3] These factors are driving researchers to find new materials that can be used in these applications.

To integrate a decoupling capacitor in an integrated circuit, the processing temperature should be below 450 °C. This is mandated because the dielectric would most likely be deposited after the interconnect processing in a standard complementary metal oxide silicon, CMOS, fabrication.[4] Thus, it would be imperative that the dielectric deposition does not perturb any of the underlying layers.

New dielectric materials with high and stable permittivities, low leakage, low dissipation factors, and low processing temperatures are required for such integrated capacitors. The Bi_2O_3-ZnO-Nb_2O_5 (BZN) pyrochlore ceramic system has been shown to exhibit these properties in bulk samples and thin films made by metal organic deposition,

MOD, and pulsed laser deposition, PLD.[5,6,7] BZN thin films also show a field tunability of the dielectric constant.[6] The processing of films by PLD and MOD has been able to produce crystalline films at temperatures of 475 °C and 550 °C, respectively.[6,7] However, many unanswered questions about processing-composition-microstructure-property relations in vapor deposited BZN films remain.

1.2 Statement of Goals

The goals of this work can be divided into the following categories:

1. Development of the deposition parameters to produce single-phase compositions of bismuth-zinc-niobate (BZN) using pulsed laser deposition. This study focused on the following two compositions: $Bi_{1.5}Zn_{1.0}Nb_{1.5}O_7$ (BZN-1) and $Bi_{1.5}Zn_{0.5}Nb_{1.5}O_{6.5}$ (BZN-0.5). This is the first study to make the BZN-1 and BZN-0.5 compositions hy pulsed laser deposition. This study focused on the interactions between the growth temperature, the chamber pressure, and laser frequency to determine the parameters required to produce single-phase compositions. These results should be transferable to other physical vapor phase deposition techniques.

2. Determination of the film composition as a function of target composition, target to substrate distance, chamber pressure, substrate temperature, and laser frequency. This should elucidate the relative roles of bombardment, resputtering, evaporation, and the distribution of species within the plume in controlling composition. The composition was measured using Rutherford Backscattering analysis.